UNIVERSITY OF CALIFORNIA

Santa Barbara

Study of Seismic Noise Excited by the Anthropogenic and Natural Causes Using Seismometers and Distributed Acoustic Sensing

A dissertation submitted in partial satisfaction of the

requirements for the degree Doctor of Philosophy

in Earth Science

by

Han Xiao

Committee in charge:

Professor Toshiro Tanimoto, Chair

Professor Chen Ji

Professor Robin Matoza

December 2022

The dissertation of Han Xiao is approved.

_____

Chen Ji

_____

Robin Matoza

_____

Toshiro Tanimoto, Committee Chair

September 2022

Study of Seismic Noise Excited by the Anthropogenic and Natural Causes Using Seismometers and Distributed Acoustic Sensing

by

Han Xiao

ACKNOWLEDGEMENTS

First of all, I would like to thank my advisor, Professor Toshiro Tanimoto, for his support and guidance during the four years of my Ph.D. I am very grateful for the research opportunities and great research environment he provided me, he has helped me a lot in my research and life and taught me to think critically and independently. He provided exciting cutting-edge research and professional theoretical guidance for my dissertation. His attitude and curiosity about scientific research, as well as his philosophy of lifelong learning, have benefited me throughout my life. No matter what career I pursue in the future, his guidance and advice will be very important to me. At the same time, I would like to thank my committee members, Professor Chen Ji and Professor Robin Matoza, for their suggestions, help, and insightful comments on my thesis. In the process of discussing with them, I will recognize the inadequacies of my research, which will allow me to improve my research ability. I would also like to thank Professor Zach Eilon and Professor Zack Spica from the University of Michigan, Ann Arbor for their help and guidance on my research.

I also thank my friends and lab mates from the geophysical group, Rodrigo De Negri Leiva, Jiong Wang, Scott Condon, Hugo Ortiz, Kayleen Rose, Brennan Brunsvik, Aaron Anderson, Richard Sanderson, Jon Petruska, Sean Maher, and Cristhian Salas Pazmiño. They have brought so much fun to me for these years.

Finally, I would like to thank my parents, grandparents and aunts. Especially I would like to thank my wife Mohan Pan and my daughter Juniper Xiao who have brought great joy and happiness to my life.

VITA OF HAN XIAO
September 2022

EDUCATION

Doctor of Philosophy in Geological Sciences (expected) September 2022
University of California, Santa Barbara, USA

Master of Geophysics June 2018
Tongji University, Shanghai, China

Bachelor of Science June 2015
Ocean University of China, Qingdao, China

PROFESSIONAL EMPLOYMENT

09/2018-09/2022 Graduate Student Researcher, Department of Earth Science, University of California, Santa Barbara
09/2018-09/2022 Teaching Assistant, Department of Earth Science, University of California, Santa Barbara
09/2015-03/2018 Graduate Student Researcher, School of Ocean and Earth Science, Tongji University

PUBLICATIONS

Spica, Z. J., Ajo-Franklin, J., Beroza, G., Biondi, B., Cheng, F., Gaite, B., ... **Xiao, H.** & Zhu, T. (2022). PubDAS: a PUBlic Distributed Acoustic Sensing datasets repository for geosciences. *Seismological Research Letter, in review*.

Xiao, H., Tanimoto, T., Spica, Z. J., Gaite, B., Ruiz-Barajas, S., Pan, M., & Viens, L. (2022). Locating the Precise Sources of High-Frequency Microseisms Using Distributed Acoustic Sensing. *Geophysical research letters, 49*(17), e2022GL099292.

Xiao, H., Tanimoto, T., & Xue, M. (2021). Study of S-wave Microseisms Generated by Storms in the Southeast Australia and North Atlantic. *Geophysical Research Letters*, 48, e2021GL093728.

Lecocq, Thomas, … and **Xiao, H.** (2020) Global quieting of high-frequency seismic noise due to COVID-19 pandemic lockdown measures. *Science* 369.6509: 1338-1343.

Xiao, H., Elion, Z., Ji, C., & Tanimoto, T. (2020). COVID-19 societal response captured by seismic noise in China and Italy, *Seismological Research Letter*, 91(5):2757-2768.

Xiao, H., Xue, M., Pan, M., & Gao, J. (2018). Characteristics of microseisms in South China. *Bulletin of the Seismological Society of America*, 108(5A), 2713-2723.

Xiao, H., Xue, M., Yang, T., Liu, C., Hua, Q., Xia, S., ... & Pan, M. (2018). The characteristics of microseisms in South China Sea: Results from a combined data set

of OBSs, broadband land seismic stations, and a global wave height model. *Journal of Geophysical Research: Solid Earth*, 123(5), 3923-3942.

AWARDS

- Archuleta Family Award, UC Santa Barbara, Dept. of Earth Science, 2022
- Geophysics Award, UC Santa Barbara, Dept. of Earth Science, 2021
- Archuleta Family Award, UC Santa Barbara, Dept. of Earth Science, 2020
- Guang Hua Scholarship, Tongji University, 2016
- Outstanding Graduate Award, Ocean University of China, 2015
- Outstanding Student Award, Ocean University of China, 2013, 2014
- Outstanding Student Academic Scholarship, Ocean University of China, 2012, 2013, 2014

FIELDS OF STUDY

Major Field: Seismology

Environmental Seismology, Anthropogenic Noise, Microseisms, and Ocean Solid Earth Interactions

ABSTRACT

Study of Seismic Noise Excited by the Anthropogenic and Natural Causes Using Seismometers and Distributed Acoustic Sensing

by

Han Xiao

Seismic noise is the continuous vibration of the ground due to various non-earthquake causes and is generally regarded as an unwanted component of the signal recorded by a seismograph. Its primary sources include human activity, ocean waves, wind, and atmospheric phenomena. It has long been discarded in seismic analysis but it contains valuable information about its excitation sources and Earth structure. This thesis aims at exploring two main components of seismic noise: anthropogenic noise (human activity) and microseisms (ocean waves). It attempts to clarify noise source characteristics, excitation mechanism, and propagation processes. By using seismic records from seismometers and Distributed Acoustic Sensing (DAS), and applying several processing techniques, we show discoveries on patterns of human behavior, SH-wave microseisms excitation mechanisms, and precise microseism source locations.

First, in Chapter 2, in regards to the anthropogenic noise, we find seismic noise is positively correlated with human activity and economic development over 20 years. We choose an iconic event: the COVID-19 pandemic to study human response recorded in seismic

noise records, on the ground that cities in mainland China and Italy imposed restrictions on travel and daily activities in response to COVID-19. It gives us an unprecedented opportunity to study the relationship between human behavior and seismic noise. In this study, we are primarily concerned with seismic noise with frequencies above 1 Hz, known as "cultural noise", mainly generated by local transportation systems. We demonstrate that seismic noise can provide an absolute real-time, anonymous characterization of human activity.

In Chapter 3, with respect to the microseisms in the frequency band 0.05-0.5 Hz, we present body-wave microseisms caused by two remote low-pressure systems off the coast of southeastern Australia and southeastern Greenland, detected by a large, dense array (~350 stations) in China. We then use two years of data to study the noise sources of body wave microseisms around the globe. The study points out that SH-wave microseisms, which theoretically should not be excited by the wave-to-wave interaction of ocean waves, can be clearly observed. We also demonstrate that SH waves can only be observed when the source region is close to an area of thick ocean-bottom sediments.

Finally, in Chapter 4, we locate the precise sources of high-frequency microseisms in the frequency band 0.5-2 Hz using the new seismic measurement technique DAS. Although microseisms have been observed for more than 100 years, precise locations of their excitation sources in the oceans are still elusive. DAS data offer opportunities for deciphering the locations of excitation sources near the coast that were not possible at all by regular seismographs, including ocean-bottom seismographs. Using DAS data off the coast of Valencia, Spain, and applying a cross-correlation approach, we show that the sources of high-frequency microseisms (0.5-2 Hz) are confined between 7 and 27 km offshore, where the water depth varies from 25 to 100 m. Over time, we observe that these sources move quickly

along narrow areas, often confined within an area of a few kilometers. Our method with DAS data allows us to characterize microseisms with high spatiotemporal resolutions, opening a new chapter in understanding the global and complex seismic phenomena that occur in the oceans.

TABLE OF CONTENTS

1. Introduction

When there are no earthquakes and the earth is in a relatively quiet period, the spectrum of the seismic record typically shows five peaks over different frequencies, which originate from different noise sources (Peterson, 1993). Research on seismic noise sources has shown that the first peak in the ultra-low frequency portion of the spectrum, i.e. noise below 2 mHz, is mainly produced by changes in atmospheric density (Tanimoto et al., 2015). The second peak in the ultra-low frequency portion is the hum in the frequency band 5-10 mHz, which may be principally caused by the interaction of oceanic infragravity waves with seafloor topography (Rhie & Romanowicz, 2004; Suda et al., 1998; Tanimoto, 2005; Tanimoto et al., 1998). The most pronounced peaks that stand out in the whole seismic spectrum are microseisms in the frequency band 0.05-0.5 Hz. And ocean waves are ultimately the main sources of microseisms (Hasselmann, 1963; Longuet-Higgins, 1950). There are two different types of microseisms. The first is called primary microseisms and the other one is secondary microseisms. The peak of the primary microseism appears in the spectrum between 0.05 Hz and 0.1 Hz and is generated by the direct coupling between the ocean waves and sea bottom topography (Ardhuin et al., 2015; Hasselmann, 1963). The secondary microseisms, which are generated through the wave-wave interactions of the ocean wave, occur at a prominent peak between 0.1 Hz and 0.5 Hz (Ardhuin et al., 2011; Kedar et al., 2008; Longuet-Higgins, 1950; Tanimoto, 2007a, 2007b; Webb, 1998). Finally, for the peak above 1 Hz, seismic noise is clearly associated with human activities such as road traffic and industrial work, so it is called “anthropogenic seismic” or “cultural noise” (McNamara & Buland, 2004). But there are also natural causes, including wind, rivers, volcanic tremors, etc., that can also stimulate the high-frequency vibrations on the ground (Dybing et al., 2019; Julian, 1994; Konstantinou &

Schlindwein, 2003; Naderyan et al., 2016; Schmandt et al., 2013; Wilcock et al., 1999; Withers et al., 1996).

Seismic noise has long been considered an unwanted component and was not analyzed in the regular seismic record process flow. Gradually, researchers found its irreplaceable value in various aspects. For example, in order to understand subsurface structure using seismic noise, various processing methods were developed, including analysis of surface wave dispersion (Shapiro & Campillo, 2004; Shapiro et al., 2005), body waves from cross-correlation functions (Poli et al., 2012), autocorrelation functions (Claerbout, 1968), H/V peak analysis (Bonnefoy-Claudet et al., 2006; Nakamura, 1989; Nogoshi, 1971), and derivation of shallow elasticity structure from colocated seismic and pressure data (Tanimoto & Wang, 2019). At the same time, through the cross-correlation of seismograms, the velocity changes in and near the faults (Brenguier, Campillo, et al., 2008) and volcanoes (Brenguier, Shapiro, et al., 2008) were shown to be monitored in real-time. In addition, it was shown that the power spectral density variations of microseisms from global and regional stations can be used for proxy estimates of ocean wave height (Cannata et al., 2020; Ferretti et al., 2013), ocean wave energy (Aster et al., 2010), polar sea ice distribution (Anthony et al., 2017; Cannata et al., 2019) and climate changes (Aster et al., 2008; Stutzmann et al., 2009). These methods expand the regions of obtaining subsurface structures beyond what was possible with earthquakes, which mainly occur at plate junctions and therefore place strong geographic limitations for recovering subsurface structures. However, despite those breakthroughs, our knowledge of seismic noise is still very limited. With respect to anthropogenic noise, for instance, how human activities affect seismic records on large scales is not well understood. Regarding microseisms, the excitation mechanisms and exact source locations still remain unclear. For

example, seismologists have been unable to adequately characterize the complexity of nearshore microseisms (Bromirski et al., 2013; Juretzek & Hadziioannou, 2016) and the origin of SH-wave or Love wave microseisms (Tanimoto et al., 2015, 2016) due to a lack of high-density marine seismic observations.

This thesis consists of five chapters. Chapter 1 is this introduction. The main parts of this thesis are based on three papers, two of which were published (Chapters 2 and 3) and one still under review (Chapter 4). Chapter 2 is about using anthropogenic noise to monitor human activity during the COVID-19 pandemic. Chapter 3 focuses on the origin of SH-wave microseisms. Chapter 4 uses data from the underwater Distributed Acoustic Sensing (DAS) to obtain precise localization of microseisms. Chapter 5 presents the outlook for future work.

In Chapter 2, we examined how human activities are reflected on seismic records at different temporal and spatial scales. In fact, focusing on anthropogenic seismic noise or "cultural noise" is somewhat new to all seismologists who generally agree that anthropogenic seismic noise inevitably interferes with or masks natural signals such as earthquakes, landslides, and volcanoes. Therefore, people often try to deploy seismometers away from anthropogenic sources of seismic noise, or in boreholes, in a way that minimizes the impact of this seismic noise on the data (Trnkoczy et al., 2012). But some seismic stations are installed in cities (Chen et al., 2022; Díaz et al., 2017; Diaz et al., 2020), and these have proven useful for our research on anthropogenic noise (Xiao et al., 2020). Previous studies have confirmed that various kinds of human activities clearly contribute to seismic noise that is >1 Hz (McNamara & Buland, 2004). However, how human activity affects seismic noise specifically remains obscure. To this end, we analyzed 20 years of anthropogenic noise data from seismometers in different cities. We found that anthropogenic noise levels correlate well with

local economic growth and the number of civil motor vehicles. And we can differentiate noise sources in different frequency bands: foot traffic and local factories/businesses are about 1-8 Hz, traffic on motorways is typically ~10-30 Hz, and trains generate noise about ~20-30 Hz. However, these may depend on local conditions and can vary from place to place. Our research demonstrates the sensitivity and richness of anthropogenic noise datasets: from seismic data we can tell work hours, lunchtimes, nightlife, and vacations through variations in noise levels.

In Chapter 3, we studied the origin of SH-wave seismic noise. We first studied body wave microseisms generated by two storms in Southeast Australia and North Atlantic using beamforming and back-projection. We then used two years of data to study the noise sources of body wave microseisms around the globe. Body waves have the advantage of being able to locate sources since we can get both back azimuth and an incident angle from array processing techniques, which make it possible to track deep ocean storms in real-time (Liu et al., 2016; Neale et al., 2017; Zhang, Gerstoft, & Bromirski, 2010). We analyzed each one-hour-long time series in continuous seismograms from a large aperture three-component seismic array in Southwestern China using two-year data. We show that P- and SV-wave microseisms can be generated in both sedimentary and non-sedimentary layers, and the P-wave source regions are consistent with earlier studies (Euler et al., 2014; Gal et al., 2015; Gerstoft et al., 2008; Pyle et al., 2015; Reading et al., 2014; Wang et al., 2018; Zhang, Gerstoft, & Shearer, 2010). However, the SH-wave microseisms are generated almost exclusively in the thick sedimentary layers, indicating amplitude enhancement by a sedimentary layer is an important process for SH-wave observations in seismic noise.

In Chapter 4, we proposed a method to locate the precise sources of microseisms generated near the coast using DAS with unprecedented spatiotemporal resolution. DAS is a new

technology that uses the optical phase changes in Rayleigh backscattered light in a long optical fiber as thousands of seismic sensors (Hartog et al., 2013; Masoudi & Newson, 2016). At the end of the fiber, an instrument called the interrogator unit (IU) sends laser pulses down the cable that reflected off the fiber flaws and bounced back to the IU. When the fiber is disturbed by changes in strain, vibrations, and temperature, there are changes in size, frequency, and phase of light scattered backed to the IU. So the researcher can use these changes to record the seismic waves that might shake the fiber with a very high spatial resolution (~10 m), giving us a new chance to locate the microseisms.

In the past decade, the sensitivity of DAS has improved significantly (Lindsey et al., 2019; Lindsey & Martin, 2021; Mestayer et al., 2011; Zhan, 2019). The performance of DAS makes them suitable for various environments, especially in places where would be too expensive to set up the seismometers (Lindsey et al., 2017; Mateeva et al., 2014). DAS can use some unused dark fibers laid by telecom companies before, which saves a lot of manpower and material resources. Although the self-noise level of DAS is much higher than broadband seismometer and closer to the geophones. The DAS data quality is reasonably well compared to the data collocated from seismometers or geophones (Correa et al., 2017; Lindsey et al., 2017; Lindsey et al., 2020), even for recording teleseismic (Ajo-Franklin et al., 2019; Yu et al., 2019).

We found that with 10-minute of under-sea DAS data, a stable cross-correlation function can be obtained from different channels that are several kilometers apart. This allows us to determine the direction of propagation of seismic waves and thus determine the precise locations of the noise source. More importantly, this method improves the temporal resolution of locating microseisms from one hour to ten minutes and the spatial resolution from hundreds of kilometers to several kilometers.

1.1 References

Ajo-Franklin, J. B., Dou, S., Lindsey, N. J., Monga, I., Tracy, C., Robertson, M., et al. (2019). Distributed acoustic sensing using dark fiber for near-surface characterization and broadband seismic event detection. *Scientific reports, 9*(1), 1-14. https://doi.org/10.1038/s41598-018-36675-8

Anthony, R. E., Aster, R. C., & McGrath, D. (2017). Links between atmosphere, ocean, and cryosphere from two decades of microseism observations on the Antarctic Peninsula. *Journal of Geophysical Research: Earth Surface, 122*(1), 153-166. https://agupubs.onlinelibrary.wiley.com/doi/abs/10.1002/2016JF004098

Ardhuin, F., Gualtieri, L., & Stutzmann, E. (2015). How ocean waves rock the Earth: Two mechanisms explain microseisms with periods 3 to 300 s. *Geophysical research letters, 42*(3), 765-772. https://doi.org/10.1002/2014GL062782

Ardhuin, F., Stutzmann, E., Schimmel, M., & Mangeney, A. (2011). Ocean wave sources of seismic noise. *Journal of Geophysical Research, 116*(C09004). https://doi.org/10.1029/2011JC006952

Aster, R. C., McNamara, D. E., & Bromirski, P. D. (2008). Multidecadal Climate-induced Variability in Microseisms. *Seismological Research Letters, 79*(2), 194-202. https://doi.org/10.1785/gssrl.79.2.194

Aster, R. C., McNamara, D. E., & Bromirski, P. D. (2010). Global trends in extremal microseism intensity. *Geophysical research letters, 37*(14). https://agupubs.onlinelibrary.wiley.com/doi/abs/10.1029/2010GL043472

Bonnefoy-Claudet, S., Cornou, C., Bard, P.-Y., Cotton, F., Moczo, P., Kristek, J., & Fäh, D. (2006). H/V ratio: a tool for site effects evaluation. Results from 1-D noise

simulations. *Geophysical Journal International, 167*(2), 827-837. https://onlinelibrary.wiley.com/doi/abs/10.1111/j.1365-246X.2006.03154.x

Brenguier, F., Campillo, M., Hadziioannou, C., Shapiro, N. M., Nadeau, R. M., & Larose, E. (2008). Postseismic Relaxation Along the San Andreas Fault at Parkfield from Continuous Seismological Observations. *Science, 321*(5895), 1478-1481. https://www.science.org/doi/abs/10.1126/science.1160943

Brenguier, F., Shapiro, N. M., Campillo, M., Ferrazzini, V., Duputel, Z., Coutant, O., & Nercessian, A. (2008). Towards forecasting volcanic eruptions using seismic noise. *Nature Geoscience, 1*(2), 126-130. https://doi.org/10.1038/ngeo104

Bromirski, P. D., Stephen, R. A., & Gerstoft, P. (2013). Are deep-ocean-generated surface-wave microseisms observed on land? *Journal of Geophysical Research: Solid Earth, 118*(7), 3610-3629. https://agupubs.onlinelibrary.wiley.com/doi/abs/10.1002/jgrb.50268

Cannata, A., Cannavò, F., Moschella, S., Di Grazia, G., Nardone, G., Orasi, A., et al. (2020). Unravelling the Relationship Between Microseisms and Spatial Distribution of Sea Wave Height by Statistical and Machine Learning Approaches. *Remote Sensing, 12*(5), 761. https://www.mdpi.com/2072-4292/12/5/761

Cannata, A., Cannavò, F., Moschella, S., Gresta, S., & Spina, L. (2019). Exploring the link between microseism and sea ice in Antarctica by using machine learning. *Scientific reports, 9*(1), 13050. https://doi.org/10.1038/s41598-019-49586-z

Chen, K. H., Yeh, T.-C., Chen, Y., Johnson, C. W., Lin, C.-H., Lai, Y.-C., et al. (2022). Characteristics and impact of environmental shaking in the Taipei metropolitan area. *Scientific Reports, 12*(1), 743. https://doi.org/10.1038/s41598-021-04528-6

Claerbout, J. F. (1968). Synthesis of a layered medium from its acoustic transmission response. *GEOPHYSICS*, *33*(2), 264-269. https://library.seg.org/doi/abs/10.1190/1.1439927

Correa, J., Egorov, A., Tertyshnikov, K., Bona, A., Pevzner, R., Dean, T., et al. (2017). Analysis of signal to noise and directivity characteristics of DAS VSP at near and far offsets — A CO2CRC Otway Project data example. *The Leading Edge, 36*(12), 994a991-994a997. https://library.seg.org/doi/abs/10.1190/tle36120994a1.1

Díaz, J., Ruiz, M., Sánchez-Pastor, P. S., & Romero, P. (2017). Urban Seismology: on the origin of earth vibrations within a city. *Scientific Reports*, *7*(1), 15296. https://doi.org/10.1038/s41598-017-15499-y

Diaz, J., Schimmel, M., Ruiz, M., & Carbonell, R. (2020). Seismometers Within Cities: A Tool to Connect Earth Sciences and Society. *Frontiers in Earth Science, 8*. Perspective. https://www.frontiersin.org/article/10.3389/feart.2020.00009

Dybing, S. N., Ringler, A. T., Wilson, D. C., & Anthony, R. E. (2019). Characteristics and Spatial Variability of Wind Noise on Near-Surface Broadband Seismometers. *Bulletin of the seismological society of America, 109*(3), 1082-1098. https://doi.org/10.1785/0120180227

Euler, G. G., Wiens, D. A., & Nyblade, A. A. J. G. J. I. (2014). Evidence for bathymetric control on the distribution of body wave microseism sources from temporary seismic arrays in Africa. *197*(3), 1869-1883. https://doi.org/10.1093/gji/ggu105

Ferretti, G., Zunino, A., Scafidi, D., Barani, S., & Spallarossa, D. (2013). On microseisms recorded near the Ligurian coast (Italy) and their relationship with sea wave height.

Geophysical Journal International, 194(1), 524-533. https://doi.org/10.1093/gji/ggt114

Gal, M., Reading, A. M., Ellingsen, S., Gualtieri, L., Koper, K., Burlacu, R., et al. (2015). The frequency dependence and locations of short-period microseisms generated in the Southern Ocean and West Pacific. *Journal of Geophysical Research: Solid Earth, 120*(8), 5764-5781. https://doi.org/10.1002/2015JB012210

Gerstoft, P., Shearer, P. M., Harmon, N., & Zhang, J. (2008). Global P, PP, and PKP wave microseisms observed from distant storms. *Geophysical research letters, 35*(23). https://doi.org/10.1029/2008GL036111

H. Hartog, A., Kotov, O. I., & Liokumovich, L. B. (2013). The Optics of Distributed Vibration Sensing. https://www.earthdoc.org/content/papers/10.3997/2214-4609.20131301

Hasselmann, K. (1963). A statistical analysis of the generation of microseisms. *Reviews of Geophysics, 1*(2), 177-210. https://doi.org/10.1029/RG001i002p00177

Julian, B. R. (1994). Volcanic tremor: Nonlinear excitation by fluid flow. *Journal of Geophysical Research: Solid Earth, 99*(B6), 11859-11877. https://agupubs.onlinelibrary.wiley.com/doi/abs/10.1029/93JB03129

Juretzek, C., & Hadziioannou, C. (2016). Where do ocean microseisms come from? A study of Love-to-Rayleigh wave ratios. *Journal of Geophysical Research: Solid Earth, 121*(9), 6741-6756. https://doi.org/10.1002/2016JB013017

Kedar, S., Longuet-Higgins, M., Webb, F., Graham, N., Clayton, R., & Jones, C. (2008). The origin of deep ocean microseisms in the North Atlantic Ocean. *Proceedings of the Royal Society A: Mathematical, Physical and Engineering Sciences, 464*(2091), 777-793. https://doi.org/10.1098/rspa.2007.0277

Konstantinou, K. I., & Schlindwein, V. (2003). Nature, wavefield properties and source mechanism of volcanic tremor: a review. *Journal of Volcanology and Geothermal Research, 119*(1), 161-187. https://www.sciencedirect.com/science/article/pii/S0377027302003116

Lecocq, T., Hicks, S. P., Van Noten, K., van Wijk, K., Koelemeijer, P., De Plaen, R. S. M., et al. (2020). Global quieting of high-frequency seismic noise due to COVID-19 pandemic lockdown measures. *Science, 369*(6509), 1338-1343. https://science.sciencemag.org/content/sci/369/6509/1338.full.pdf

Lindsey, N. J., Dawe, T. C., & Ajo-Franklin, J. B. (2019). Illuminating seafloor faults and ocean dynamics with dark fiber distributed acoustic sensing. *Science, 366*(6469), 1103-1107. https://science.sciencemag.org/content/sci/366/6469/1103.full.pdf

Lindsey, N. J., & Martin, E. R. (2021). Fiber-Optic Seismology. *Annual Review of Earth and Planetary Sciences, 49*(1), null. https://www.annualreviews.org/doi/abs/10.1146/annurev-earth-072420-065213

Lindsey, N. J., Martin, E. R., Dreger, D. S., Freifeld, B., Cole, S., James, S. R., et al. (2017). Fiber-Optic Network Observations of Earthquake Wavefields. *Geophysical research letters, 44*(23), 11,792-711,799. https://agupubs.onlinelibrary.wiley.com/doi/abs/10.1002/2017GL075722

Lindsey, N. J., Rademacher, H., & Ajo-Franklin, J. B. (2020). On the Broadband Instrument Response of Fiber-Optic DAS Arrays. *Journal of Geophysical Research: Solid Earth, 125*(2), e2019JB018145. https://agupubs.onlinelibrary.wiley.com/doi/abs/10.1029/2019JB018145

Liu, Q., Koper, K. D., Burlacu, R., Ni, S., Wang, F., Zou, C., et al. (2016). Source locations of teleseismic P, SV, and SH waves observed in microseisms recorded by a large aperture seismic array in China. *Earth and Planetary Science Letters, 449*, 39-47. https://doi.org/10.1016/j.epsl.2016.05.035

Longuet-Higgins, M. S. (1950). A Theory of the Origin of Microseisms. *Philosophical Transactions of the Royal Society of London A-Mathematical and Physical Sciences, 243*(857), 1-35. https://doi.org/10.1098/rsta.1950.0012

Masoudi, A., & Newson, T. P. (2016). Contributed Review: Distributed optical fibre dynamic strain sensing. *Review of scientific instruments, 87*(1), 011501. https://aip.scitation.org/doi/abs/10.1063/1.4939482

Mateeva, A., Lopez, J., Potters, H., Mestayer, J., Cox, B., Kiyashchenko, D., et al. (2014). Distributed acoustic sensing for reservoir monitoring with vertical seismic profiling. *Geophysical Prospecting, 62*(4), 679-692. https://onlinelibrary.wiley.com/doi/abs/10.1111/1365-2478.12116

McNamara, D. E., & Buland, R. P. (2004). Ambient noise levels in the continental United States. *Bulletin of the Seismological Society of America, 94*(4), 1517-1527. https://doi.org/10.1785/012003001

Mestayer, J., Cox, B., Wills, P., Kiyashchenko, D., Lopez, J., Costello, M., et al. (2011). Field trials of distributed acoustic sensing for geophysical monitoring. In *SEG Technical Program Expanded Abstracts 2011* (pp. 4253-4257).

Naderyan, V., Hickey, C. J., & Raspet, R. (2016). Wind-induced ground motion. *Journal of Geophysical Research: Solid Earth, 121*(2), 917-930. https://agupubs.onlinelibrary.wiley.com/doi/abs/10.1002/2015JB012478

Nakamura, Y. (1989). A method for dynamic characteristics estimation of subsurface using microtremor on the ground surface. *Railway Technical Research Institute, Quarterly Reports, 30*(1).

Neale, J., Harmon, N., & Srokosz, M. (2017). Monitoring remote ocean waves using P-wave microseisms. *Journal of Geophysical Research: Oceans, 122*(1), 470-483. https://doi.org/10.1002/2016JC012183

Nogoshi, M. (1971). On the amplitude characteristics of microtremor, Part II. *Journal of the seismological society of Japan, 24*, 26-40.

Peterson, J. (1993). Observations and Modeling of Seismic Background Noise. *94*.

Poli, P., Campillo, M., & Pedersen, H. (2012). Body-Wave Imaging of Earth's Mantle Discontinuities from Ambient Seismic Noise. *Science, 338*(6110), 1063. http://science.sciencemag.org/content/338/6110/1063.abstract

Pyle, M. L., Koper, K. D., Euler, G. G., & Burlacu, R. J. G. R. L. (2015). Location of high-frequency P wave microseismic noise in the Pacific Ocean using multiple small aperture arrays. *42*(8), 2700-2708. https://doi.org/10.1002/2015GL063530

Reading, A. M., Koper, K. D., Gal, M., Graham, L. S., Tkalčić, H., & Hemer, M. A. (2014). Dominant seismic noise sources in the Southern Ocean and West Pacific, 2000–2012, recorded at the Warramunga Seismic Array, Australia. *Geophysical research letters, 41*(10), 3455-3463. https://doi.org/10.1002/2014GL060073

Rhie, J., & Romanowicz, B. (2004). Excitation of Earth's continuous free oscillations by atmosphere–ocean–seafloor coupling. *Nature, 431*(7008), 552-556. https://doi.org/10.1038/nature02942

Schmandt, B., Aster, R. C., Scherler, D., Tsai, V. C., & Karlstrom, K. (2013). Multiple fluvial processes detected by riverside seismic and infrasound monitoring of a controlled flood in the Grand Canyon. *Geophysical Research Letters*, *40*(18), 4858-4863. https://agupubs.onlinelibrary.wiley.com/doi/abs/10.1002/grl.50953

Shapiro, N. M., & Campillo, M. (2004). Emergence of broadband Rayleigh waves from correlations of the ambient seismic noise. *Geophysical Research Letters*, *31*(7). https://agupubs.onlinelibrary.wiley.com/doi/abs/10.1029/2004GL019491

Shapiro, N. M., Campillo, M., Stehly, L., & Ritzwoller, M. H. (2005). High-resolution surface-wave tomography from ambient seismic noise. *Science*, *307*(5715), 1615-1618. http://doi.org/10.1126/science.1108339

Stutzmann, E., Schimmel, M., Patau, G., & Maggi, A. (2009). Global climate imprint on seismic noise. *Geochemistry, Geophysics, Geosystems*, *10*(11). https://agupubs.onlinelibrary.wiley.com/doi/abs/10.1029/2009GC002619

Suda, N., Nawa, K., & Fukao, Y. (1998). Earth's Background Free Oscillations. *Science*, *279*(5359), 2089-2091. https://www.science.org/doi/abs/10.1126/science.279.5359.2089

Tanimoto, T. (2005). The oceanic excitation hypothesis for the continuous oscillations of the Earth. *Geophysical Journal International*, *160*(1), 276-288. https://doi.org/10.1111/j.1365-246X.2004.02484.x

Tanimoto, T. (2007a). Excitation of microseisms. *Geophysical research letters*, *34*(5). https://agupubs.onlinelibrary.wiley.com/doi/abs/10.1029/2006GL029046

Tanimoto, T. (2007b). Excitation of normal modes by non-linear interaction of ocean waves. *Geophysical Journal International*, *168*(2), 571-582. https://doi.org/10.1111/j.1365-246X.2006.03240.x

Tanimoto, T., Hadziioannou, C., Igel, H., Wasserman, J., Schreiber, U., & Gebauer, A. (2015). Estimate of Rayleigh-to-Love wave ratio in the secondary microseism by colocated ring laser and seismograph. *Geophysical research letters*, *42*(8), 2650-2655. https://doi.org/10.1002/2015GL063637

Tanimoto, T., Heki, K., & Artru-Lambin, J. (2015). Interaction of Solid Earth, Atmosphere, and Ionosphere. In G. Schubert (Ed.), *Treatise on Geophysics* (2nd ed., Vol. 4, pp. 421-443). Amsterdam: Elsevier. https://doi.org/10.1016/B978-044452748-6.00075-4

Tanimoto, T., Lin, C.-J., Hadziioannou, C., Igel, H., & Vernon, F. (2016). Estimate of Rayleigh-to-Love wave ratio in the secondary microseism by a small array at Piñon Flat observatory, California. *Geophysical research letters*, *43*(21), 11,173-111,181. https://doi.org/10.1002/2016GL071133

Tanimoto, T., Um, J., Nishida, K., & Kobayashi, N. (1998). Earth's continuous oscillations observed on seismically quiet days. *Geophysical research letters*, *25*(10), 1553-1556. https://agupubs.onlinelibrary.wiley.com/doi/abs/10.1029/98GL01223

Tanimoto, T., & Wang, J. (2019). Theory for Deriving Shallow Elasticity Structure From Colocated Seismic and Pressure Data. *Journal of Geophysical Research: Solid Earth*, *124*(6), 5811-5835. https://agupubs.onlinelibrary.wiley.com/doi/abs/10.1029/2018JB017132

Trnkoczy, A., Bormann, P., Hanka, W., Holcomb, L. G., Nigbor, R. L., Shinohara, M., et al. (2012). Site selection, preparation and installation of seismic stations. In *New Manual*

of Seismological Observatory Practice 2 (NMSOP-2) (pp. 1-139): Deutsches GeoForschungsZentrum GFZ. https://doi.org/10.2312/GFZ.NMSOP-2_ch7

Wang, W., Gerstoft, P., & Wang, B. J. G. J. I. (2018). Seasonality of P wave microseisms from NCF-based beamforming using ChinArray. *213*(3), 1832-1848.

Webb, S. C. (1998). Broadband seismology and noise under the ocean. *J Reviews of Geophysics*, *36*(1), 105-142. https://doi.org/10.1029/97RG02287

Wilcock, W. S. D., Webb, S. C., & Bjarnason, I. T. (1999). The effect of local wind on seismic noise near 1 Hz at the MELT site and in iceland. *Bulletin of the seismological society of America*, *89*(6), 1543-1557. https://doi.org/10.1785/BSSA0890061543

Withers, M. M., Aster, R. C., Young, C. J., & Chael, E. P. (1996). High-frequency analysis of seismic background noise as a function of wind speed and shallow depth. *Bulletin of the seismological society of America*, *86*(5), 1507-1515. https://doi.org/10.1785/BSSA0860051507

Xiao, H., Eilon, Z. C., Ji, C., & Tanimoto, T. (2020). COVID-19 Societal Response Captured by Seismic Noise in China and Italy. *Seismological Research Letters*, *91*(5), 2757-2768. https://doi.org/10.1785/0220200147

Yu, C., Zhan, Z., Lindsey, N. J., Ajo-Franklin, J. B., & Robertson, M. (2019). The Potential of DAS in Teleseismic Studies: Insights From the Goldstone Experiment. *Geophysical research letters*, *46*(3), 1320-1328. https://agupubs.onlinelibrary.wiley.com/doi/abs/10.1029/2018GL081195

Zhan, Z. (2019). Distributed Acoustic Sensing Turns Fiber-Optic Cables into Sensitive Seismic Antennas. *Seismological Research Letters*, *91*(1), 1-15. https://doi.org/10.1785/0220190112

Zhang, J., Gerstoft, P., & Bromirski, P. D. (2010). Pelagic and coastal sources of P-wave microseisms: Generation under tropical cyclones. *Geophysical research letters, 37*(15), L15301. http://dx.doi.org/10.1029/2010GL044288

Zhang, J., Gerstoft, P., & Shearer, P. M. (2010). Resolving P-wave travel-time anomalies using seismic array observations of oceanic storms. *Earth and Planetary Science Letters, 292*(3-4), 419-427. https://doi.org/10.1016/j.epsl.2010.02.014

2. COVID-19 Societal Response Captured by Seismic Noise in China and Italy

This chapter appeared essentially in this form in:

Han Xiao, Zachary Cohen Eilon, Chen Ji, Toshiro Tanimoto; COVID-19 Societal Response Captured by Seismic Noise in China and Italy. Seismological Research Letters 2020, 91 (5): 2757–2768. doi:10.1785/0220200147

2.1 Introduction

Cultural noise, which is almost always above 1 Hz on the seismic background, is generated by human activities (Green et al., 2017; Groos & Ritter, 2009; McNamara & Buland, 2004; Stutzmann et al., 2000) such as trains (Chen et al., 2004; Ribes-Llario et al., 2017; Sheen et al., 2009), road traffic (Coward et al., 2003; Hao & Ang, 1998) and airports (Meng & Ben-Zion, 2018). These noise sources are now known to be useful for studying the subsurface structures (Ajo-Franklin et al., 2019; Nakata et al., 2011; Quiros et al., 2016; Riahi & Gerstoft, 2015).

The outbreak of the novel coronavirus SARS-CoV-2 disease (hereafter: COVID-19) was first reported in Wuhan, Hubei, China, in December 2019 (Andersen et al., 2020). In early to mid-January 2020, the virus spread to other Chinese provinces, facilitated by increased travel during the Chinese Lunar New Year. With Wuhan being a major rail transport hub in China, the virus quickly spread throughout the country. On 23 January 2020, Wuhan and other cities in Hubei province imposed a lockdown in an effort to quarantine the epicenter of the COVID-19 outbreak (Lu, 2020). In most of the areas where this came into effect, villages, communities, and units could only keep one entrance and exit point open, and a limited number of people from each household were allowed to enter and exit. In some places, night-time access to villages or communities were prohibited, effectively a curfew, and in extreme cases, the movement was prohibited throughout the day (Graham-Harrison and Kuo, 2020; WHO, 2020). All public transportation except for emergency and supply vehicles were suspended. A total of 12 other counties to prefecture-level cities in Hubei, including Enshi, the location of one of the seismic stations used in this study, were placed on travel restrictions by the end of 24 January 2020 (Table 2.1). The World Health Organization (WHO) declared

the outbreak to be a Public Health Emergency of International Concern on 30 January 2020(Groos & Ritter, 2009)(Groos & Ritter, 2009)(Groos & Ritter, 2009). By chance, this outbreak closely coincided with the Chinese Lunar New year of 2020, and the Chinese government utilized this coincidence to facilitate lockdown logistics, essentially extending the traditional week-long national holiday for several months.

In Italy, following the rapid expansion of an outbreak of COVID-19 cases in the north of the country in late February 2020, the Italian government imposed a lockdown on many of its Northern provinces on 8 March 2020. The lockdown restricted all movement except for work, health circumstances and essential activities. On the evening of 9 March, quarantine measures were extended to the entire nation, becoming effective the next day. This quarantine included some important differences from the restrictions in China. For example, the lockdown did not apply to the public transportation system, including buses, railways, flights, and ferry services. People with self-declared travel exemptions were permitted to travel. On 11 March 2020, the WHO declared the outbreak a pandemic(Hao & Ang, 1998)(Hao & Ang, 1998)(Hao & Ang, 1998). This pandemic provides an unusual dataset allowing comparison of changes in seismic noise to the known timings of social orders.

In this study, we analyze continuous seismic time series from seismic stations in China and Italy (Figure 2.1). We particularly focus on understanding the characteristics of cultural noise before and after the lockdowns.

2.2 Data and methods

We utilized data from the New China Digital Seismograph Network (NCDSN), in operation since 1992, with the network code IC. Data from IC were obtained from 1 January

2000 to 15 April 2020. Those stations are: station IC.ENH, located in Enshi, Hubei province; station IC.MDJ, located in Mudanjiang, Heilongjiang province in the northeast region of China; station IC.BJT which is located in the northwest of Beijing, the capital of China; and station IC.QIZ which is located on Hainan island in Qiongzhou (Figure 2.1). We also analyzed data from the Italian National Seismic Network (INSN), with the network code IV. These data, including seismic stations IV.MILN in Milan, IV.MONC close to Torino, and IV.RMP ~20 km southeast of Rome, were obtained from 15 December 2019 to 15 April 2020 (Figure 2.1).

We analyzed broadband high-gain vertical seismograms (BHZ) and high-sample-rate high-gain broadband three-component seismograms (HHN, HHE, and HHZ), with sample rates of 20 Hz and 100 Hz, respectively. Ground acceleration records were retrieved by deconvolving the instrumental response from the original seismograms. All seismic data were divided into one-hour segments with overlapping time intervals of 50% (30 minutes). Each one-hour segment was detrended, tapered with a Hanning window, and the power spectral densities (PSDs) were calculated after amplitude correction with a factor 2. The binning we used in the frequency domain is 1/8th octave, with the highest frequency resolution 0.004525 Hz at 0.05 Hz and the lowest resolution 4.5254 Hz at 50 Hz, which may reduce the ability to identify the narrow-band peaks at high frequency (Anthony *et al.*, 2020). However, in this study we can still distinguish the general characteristics of cultural noise before and after the lockdowns. We did not remove earthquake signals from the time series, because the effects of earthquakes are limited to short time intervals and predominantly contain their most characteristic signals at lower frequencies. Thus they have extremely small overall effects on the estimation of cultural noise. We show noise power levels in units of decibels (dB) with

respect to $10\log_{10}(\mathrm{m^2 s^{-4} Hz^{-1}})$. We also performed a frequency-dependent polarization analysis for the high broadband three-component seismic data to determine the source directions of the cultural noise (Koper & Hawley, 2010; Park et al., 1987; Samson, 1983).

2.3 Results

2.3.1 Baseline seismic noise patterns at ENH

We use a twenty-year-long seismic record from station IC.ENH, located in Enshi, Hubei province, China, to establish important baselines and patterns in the cultural noise, illustrating the detailed ways in which this signal is related to societal behavior. The vertical PSD for this station is shown in Figure 2.2. Enshi is a county-level city, about 460 km west of Wuhan, with a metro area population of 0.587 Million. Typical secondary microseism peaks are distinct in this figure with an approximate frequency band of 0.15-0.5 Hz. Another distinct peak can be identified at high frequencies, approximately in the 1.5-8 Hz frequency band. As we will show, this peak is caused by cultural noise.

There is a clear increasing trend in seismic noise in Enshi between 2000 and 2020 which shows a good correlation with the local economic growth and the number of civil motor vehicles (Figures 2.2b and 2.2c). Black arrows in Figure 2.2a show the timings of the Chinese Lunar New Year since 2000, correlating well with an annual lull in cultural noise due to decreased traffic flow and closure of factories. The red arrow in Figure 2.2a indicates the time that Enshi came under lockdown, resulting in a sudden decrease of cultural noise. We explore the effects of this lockdown by examining vertical component PSDs for the first three months of the year, comparing vertical PSDs between 2018 (Figure 2.3a) and 2020 (Figure 2.4a).

The 2018 data at this site provide information on various aspects of social life in a regular year, including diurnal variations, a holiday effect, and seasonal variations (Figures 2.3a, 2.5a and 2.5b). We find that two distinct cultural noise spectral peaks are evident, with approximate frequency bands of 1.5–8 Hz and 10-20 Hz. Diurnal variations are strong; there is higher seismic noise during the daytime than at night. The largest change in noise patterns is correlated well with the national holiday of the Chinese Lunar New Year, which typically starts one day before the New Year day and ends five days after. The noise lull is the result of cessation in typical travel and industrial activity. During this period there is, on average, a 10 dB noise drop in the frequency band 1.5-8 Hz, compared to the background level. In detail, we show that the noise level started to drop 5-6 days before the holiday and did not fully recover until another two weeks after (Figure 2.6c). This frequency band also exhibits seasonal variations (Figure 2.5a) which is longer strong noise signal in the summer than the winter corresponding to variation in daylight hours. We infer that 1.5-8 Hz noise is probably generated by the local factories, pedestrians (Alyamkin & Eremenko, 2011), and low-speed urban road traffic (Green et al., 2017).

By contrast, the noise in the frequency band 10-20 Hz is relatively stable during the Chinese Lunar New Year. This persistence allows the noise source to be identified. Long (1971) found that moving vehicles on the freeway generate noise with peak frequency at about 10-20 Hz, and that this signal can be detected within 5-8 km. The station IC.ENH is located ~3 km from the freeway G50 to its southeast (Figure 2.1). The G50 is a 1900 km long and east-west bound expressway connecting Shanghai, China to the east and Chongqing, China to the west. While we are not yet able to retrieve the record of daily traffic-flow volume on the

G50 near city Enshi, traffic data for a segment of this freeway named as Huanghuang east of Wuhan can be accessed and we use it as the representative of the general traffic flow on this road within Hubei province. The average daily traffic-flow volume on the freeway during the 2018 Chinese Lunar New Year was only 31% less than the daily volume on the regular days (Table 2.2). This suggests that the cultural noise peak in the frequency band 10-20 Hz can be explained by the high-speed cars on the freeway. This is further supported by the back azimuths of the polarization ellipsoids in Figure 2.3b. The source direction of cultural noise in the 10-20 Hz frequency band is from the southeast (back azimuths are ~ 120° – 150°) during the daytime, indicating the noise arrives from the direction of the freeway. The northwest noise source during the night (Figure 2.3c) is probably from the downtown area, which lies in that direction. This dataset also shows a period of freeway traffic control between 13 September 2018 and 26 October 2018, when freeway access was limited or cut off due to road repairs. Station IC.ENH exhibits clear 10-20 Hz noise power reduction during this period (Figure 2.5b).

Our findings agree with previous analyses of frequency bands typical for road traffic (Groos and Ritter, 2009; Boese et al., 2015; Chang et al., 2016; Green et al., 2017) and consistent with a correlation between the cars' noise frequency content and their speed: the peak frequency band for the low-speed urban road traffic is 1.5-8 Hz, and for the high-speed cars traveling on the freeway it is 10-20 Hz (Long, 1971). Overground rail transportation could generate the seismic noise above 30 Hz in the seismograms (Boese et al., 2015; Chen et al., 2004; Green et al., 2017; Riahi & Gerstoft, 2015), and the Chinese Lunar New Year is the peak travel season for the railway stations. However, according to our observations, there is a 5 dB reduction in the frequency band 30-40 Hz during this period, suggesting that the noise

generated by the rail does not dominate our seismic record, perhaps due to the high attenuation and relatively far distance (8 km).

2.3.2 Comparison of living habits between China and Italy.

These data also reveal the various living habits of people in different cities (Figure 2.5). For station IC.ENH located in Enshi (Figures 2.5a and 2.5b), China, as we mentioned before, we can see the lull caused by the Chinese Lunar New Year in January or February (Figure 2.2). In general, people in Enshi show most activity from 8 a.m. to 5 p.m. during the winter. In the summer, people tend to be active for longer, from 7:00 a.m. to 6:00 p.m. There is a lunch-time lull year-round at noon. However, for the frequency band 10-20 Hz generated by the traveling cars on the freeway (Figure 2.5b), the lunch-time lull is longer and continues for about two hours during the summer. This may reflect hot noon-time weather in the summer discouraging people from going outside. Interestingly, the Chinese data do not show clear weekly cycles; work and activity continue week-round. In Milan, Italy (Figures 2.5c and 2.5d), people work longer during weekdays (from 5 a.m. to 11 p.m.) and show clear differences in behavior on weekdays compared to the weekend. We can also see the cultural noise lull caused by local holidays, such as Easter Monday (April 22), Liberation Day (April 25), Ferragosto (August 15) and Christmas (December 25). The cultural noise in the frequency band 10-40 Hz lull caused by the 2019 Christmas holiday for station IV.MILN is ~2 dB (Figure 2.8b). This may be related to the fact that this station is located in the National Research Institute, which is closed at Christmas. Interestingly, there are four distinct noise sources in frequency bands 1-2 Hz, 3-8 Hz, 10-20 Hz, and 20-40 Hz for station IV.RMP which is located in the Rome Observatory and a popular destination for astrophiles (Figures 2.8e and 2.10). We

estimate the first peak in 1-2 Hz (Figure 2.9a), with a ~5 dB reduction during the 2019 Christmas period, is generated by these visitors (Alyamkin and Eremenko, 2011), since the Observatory is closed during the holiday of Christmas. By comparison to the Chinese data, we believe the second peak at 3-8 Hz (Figure 2.9b) is generated by the local factories and low-speed cars on the street; this band a ~3dB deduction at Christmas. Finally, the high-speed cars on the freeway and the trains are responsible for the frequency bands at 10-20 Hz and 20-40 Hz respectively, which exhibit a ~2 dB reduction during Christmas (Figure 2.8f). However, there is no obvious diminishing in seismic noise power during the Christmas holiday for station IV.MONC (Figure 2.8d), in which the noise is mainly from the road nearby (Figure 2.1). We note that there is a remarkable difference in the level of cultural noise (1-40 Hz) between IV.MILN, IV.RMP and IV.MONC, as stations IV.MILN and IV.RMP exhibit much higher noise. We believe the reason is that stations IV.MILN and IV.RMP are in an urban area, whereas IV.MONC is in a mountainous area (Figure 2.1). It is worth noting that all three stations clearly recorded ocean-generated microseisms signal in the frequency band 0.05-0.5 Hz, whereas only station (IV.RMP) recorded strong noise in the 0.5-1 Hz band; this was probably generated by wind (Groos & Ritter, 2009; Withers et al., 1996) (Figure 2.8). Usually, the microseisms are stronger in the local winter and weaker in the local summer, which does not affect our analysis in cultural noise because of the differences in the frequency bands (Figure 2.A2). Italy follows the European Summer Time annual Daylight Saving Time procedure setting the clocks forward one hour from standard time during the summer months. In 2019, summer time was from March 31 to October 27. Figures 2.5c and 2.5d show a clear time shift of cultural noise power due to these clock changes. The abrupt time shift in the frequency band 10-40 Hz (Figure 2.5d) at the time of clock changes is reflective of the fact

that this seismic noise is generated by public transportation, such as trains, and buses, which have a fixed schedule. We highlight how cultural noise data reflects nuances in societal behavior in order to illustrate how these data can provide a detailed proxy account of the societal COVID-19 response.

2.3.3 Cultural noise changes in China

In 2020 we observe a sharp decrease in cultural noise in (Figures 2.4a and 2.4d) which coincides with the time when the city of Enshi went under lockdown due to COVID-19 (Table 1), and the extended new year holiday. By comparison to historical data (Figure 2.2), in the 1-8 Hz band the ~12 dB decrease was equivalent to the abrupt cessation of roughly 20 years' worth of urbanization and development activity. In Figure 2.4a, a weak peak still appears during the lockdown time in the frequency band around 10-20 Hz. This could be caused by the official vehicles and the supply vehicles on the road (Boese et al., 2015; Chang et al., 2016; Green et al., 2017; Groos & Ritter, 2009). The seismic noise power of this peak increases steadily as more vehicles appear on the road from approximately relative day 45 onwards. Directional analysis of this noise reveals that it mainly comes from the southeast even at night (Figure 2.4b and 2.4c) where the national freeway is located (Figure 2.1). The systematic increase in traffic as the lockdown eased serves as a natural experiment that we can leverage to better understand the relationship between traffic and seismic noise. Seismic noise generated by pedestrians and local industry is usually in the frequency band 1-5 Hz (Alyamkin & Eremenko, 2011). On the one hand, the marked decrease of seismic noise power in this frequency band during the lockdown period (Figure 2.4a) reflects the many fewer pedestrians and cars on the street. On the other hand, the observation that 1-5 Hz social noise increased

~5 dB in a two week period from relative days 46 to 60 suggests that Enshi started to gradually reopen much earlier than the official lift of the lockdown. Note that the increase in social noise at Enshi is correlated well with the traffic flow volume at the highway segment 600 km away (Figure 2.4d). It suggests that this gradual reopening is a province-wide activity.

The lockdown of Hubei province came one day before the 2020 Chinese Lunar New Year (January 25), the most important festival in the country. To quantify the reduction in cultural noise power caused by the coronavirus alone, we compared the daily cultural noise power variation between 2018 and 2020 using the day of Chinese Lunar New Year as the reference time in Figure 2.6. It is worth noting that they show a similar pattern before the lockdown of the cities in the Hubei province. However, after the lockdown, the cultural noise power in 2020 is much lower than in 2018. The average reduction was ~10 dB in the frequency band 1.5-8 Hz (Figure 2.6c), and ~12 dB in 10-20 Hz for the station IC.ENH.

We conducted a similar analysis at several other stations located within urban centers in China (Figures 2.6 and 2.7). None of these regions came under direct lockdown. We again compared the vertical component power spectral densities between the years 2018 (Figure 2.7, left) and 2020 (Figure 2.7, right). We found that the peak frequencies of cultural noise appear to be different for different cities. This is probably due to the relative distances to the noise sources and the installation (environmental) conditions at different station sites (Trnkoczy et al., 2012).

For station IC.MDJ (Figures 2.7a and 2.7b), located in the northeast region of China, the cultural noise is seen in mainly two peaks, similarly to at IC.ENH. One spans the frequency band 5-10 Hz and the other the frequency band 10-30 Hz. The first peak seems to be consistent with the local road traffic, and the second peak is consistent with the noise by the nearby

railway that is at a distance of about 3 km. A substantial change in noise is observed coincident with the lockdown of Hubei and Lunar New Year. The duration and magnitude of this noise change, when compared to the 2018 record, demonstrates that this change substantially exceeded the 'normal' variation due to the new year holiday, indicating that industry and civilians altered behavior in Mudanjiang in response to COVID-19 despite the lack of formal local lockdown. There was a ~3 dB reduction in the frequency band 5-10 Hz (Figure 2.6a), and ~4 dB in the frequency band 10-30 Hz. The lowest noise conditions persisted for ~20 days, followed by a slow return to normal noise levels over a further ~60 day period.

Station IC.BJT, located in Beijing, shows only the lower frequency cultural noise, in this station mostly at 2-5 Hz (Figures 2.7c and 2.7d). This may be related to site installation: this seismograph was installed in a deep tunnel, which might suppress high-frequency noise (McNamara & Buland, 2004). This 2-5 Hz cultural noise is likely to be generated by both the road traffic and by pedestrians (Alyamkin & Eremenko, 2011; Boese et al., 2015; Green et al., 2017). As with other stations, the COVID-19 effects produced a protracted lull in the cultural noise, with a reduction ~4 dB in 2-5 Hz (Figure 2.6b). At this station the duration of the noise reduction was longer, more than 81 days. The return to 'normal' cultural noise levels was substantially more gradual than at other stations, with a slow increase in amplitudes from Julian day 30 and recovery to early-January noise levels at approximately Julian day 100 (76 days after the Hubei lockdown started). The noise levels at IC.BJT is still lower than the 'normal' background noise levels of 2018 until April 22 (Julian day 113), implying a persistent alteration in traffic and social patterns from 'business as usual'.

Station IC.QIZ, located on Hainan island, which is famous for its tourism industry during the winter, shows a similar pattern to IC.ENH (Figures 2.7e and 2.7f), with a dominant cultural

noise peak in the range 2-20 Hz that seems to include distinct sources in bands 2-8 Hz and 8-20 Hz. This is probably because both stations are closer to the freeways (unlike station IC.MDJ) (Figure 2.1). IC.QIZ manifests a similar noise variation to IC.MDJ, with a ~30 day lull, followed by a gradual return to 'normal' but still less than the background levels in 2018 over a further ~51 day period (Figure 2.6d). The average reduction is ~10 dB in the frequency band 2-8 Hz and ~8 dB in the frequency band 10-20 Hz. Interestingly, the higher frequency (10-20 Hz) noise at this station seems to recover faster than the lower frequency (2-8 Hz) noise. If the former reflects high-speed vehicular traffic and the latter reflects pedestrian traffic, this staggered recovery may result from civilians feeling safe travelling in their own cars earlier than they feel comfortable walking around.

2.3.4 Cultural noise changes in Italy during lockdown

Italy was put under a dramatic lockdown (Table 2.1) as the coronavirus continued to spread in the country. Although it was one of the toughest responses implemented outside of China, their lockdown policy was less strict than China. As a result, we might expect traffic noise not to have decreased as sharply as we found in mainland China. We find only ~1 dB of decrease of cultural noise power in the frequency band 10-40 Hz in IV.MILN and ~5 dB of decrease in IV.MONC after Italy declared its lockdown (Figure 2.8). For station IV.RMP, the seismic noise power reduction was ~6 dB in 1-2 Hz (Figure 2.9a), indicating many fewer visitors in the Rome Observatory. There is a ~4 dB reduction in the frequency band 3-8 Hz (Figure 2.9b) and ~5 dB reduction in the frequency band 10-40 Hz (Figure 2.8f), which implies the decrease in traffic-volume was less than the reduction in foot-traffic. We calculated the PSDs for other IV stations in Italy, and the results are similar to the three

stations shown in this paper. Figure 2.A3 shows two examples including IV.FIR from Florence and IV.CMSN from Naples. Our observations are consistent with the local lockdown policies. The Italian authorities required that their schools, universities, theaters, cinemas, bars, and nightclubs must be closed. Religious gatherings, including funerals and weddings, and sporting events were suspended or postponed. Restaurants and bars were allowed to be open from 6 a.m. to 6 p.m., and shopping malls and markets could open on weekdays with a decreased density of patrons. Under such conditions, the cultural noise should be primarily generated by transportation systems. Lack of any decreasing seismic noise across the lockdown timing seems to corroborate the inference that the primary noise source was public transportation, which was not impacted by the lockdown (Pepe *et al.*, 2020). It appears that the continuous operation of the public transportation system maintained the persistently high level of cultural noise.

Despite this, a modest but significant decrease in noise level is observed at all Italian stations, from a period beginning at the official lockdown until Julian day 125. At stations with higher overall cultural noise (IV. MILN and IV.RMP), the pattern of noisy weekdays and less noisy weekends continues after the lockdown, although both shift to lower-noise than their pre-lockdown counterparts. In fact, for IV.RMP, near Rome, the post-lockdown week days are less noisy than even the quiet pre-lockdown weekends.

For station IV.MILN, the lowest noise power appears in the first weekend after lockdown of the country, with the lowest noise conditions persisting just for one day. We also note that even the quietest post-lockdown day is not as quiet as the 2019 Christmas day. Since Julian day 74 we observe a slow increase in noise over a further 40 day period, perhaps indicating that civilians are increasingly willing to go outside in Milan. However, the noise levels have

not yet reached pre-lockdown levels. For station IV. MONC, seismic noise reduced ~5 dB following the lockdown over a period of 5 days. There is no clear trend of noise increase at this station, perhaps indicating a more strict maintenance of social distancing and stay-at-home behavior. Station IV.RMP, by contrast, recorded a near-immediate reduction in seismic noise over the few days following the lockdown, and actually manifests a gradually decreasing trend for the entire cultural noise frequency band 1-40 Hz. The decrease is particularly evident in the 1-2 Hz and 3-8 Hz period bands associated with pedestrians and local urban traffic (Figure 2.9). This trend may imply that people in Rome are increasingly concerned by the COVID-19 pandemic and are adjusting their behavior to be more conservative.

2.4 Conclusions

Seismic records provide unique signals that can elucidate human activities on a large scale. In this paper, we examined variations in seismic noise between 1 Hz and 40 Hz, which provide proxy information on cultural behavior. In particular, we focused on the effects of governmental lockdowns and self-imposed behavioral alterations due to the outbreak of COVID-19 in mainland China and Italy. Using seismic records from stations in China and Italy, we show that the cultural noise in the range of about 2-40 Hz was primarily generated by the local transportation and population sources and study the living habits of local people by using seismic data. The lockdown of the cities and imposition of travel restrictions led to a ~4-12 dB decrease in cultural noise power on the background of the seismic noise in mainland China. According to our observations, different Chinese cities experienced distinct patterns of diminished cultural noise, related to the differing local responses to the epidemic. A marked noise change was found even in cities that did not come under government-

mandated quarantine. In contrast, there was only ~1-6 dB decrease of cultural noise power after Italy was put under a total lockdown, due to continuous public transport. Italian cities seem to be responding differently in terms of social behavior as the lockdown continues.

2.5 Data and resources

The data used in this study were collected from the Incorporated Research Institutions for Seismology (IRIS) Data Management Center (DMC; www.iris.edu/dms) and the Italian National Institute of Geophysics and Volcanology (INGV; http://webservices.ingv.it) in Italy using ObsPy Python package (Beyreuther et al., 2010). The population data for Enshi are from https://www.macrotrends.net/cities/23612/enshi/population. The GDP data are from the China National Bureau of Statistics (http://www.stats.gov.cn/). The traffic volume data are from http://www.hhgs.org.cn. We used GMT (Wessel & Smith, 1991) to make many of the figures in this paper. Our data for seismic PSD, polarization results and traffic-flow volume on the freeway can be obtained from https://zenodo.org/record/3740214#.XojbDC2ZNE6. The supplemental material includes three figures that provide additional information on our paper. Figure 2.A1 shows the location detail of seismic station IV.RMP using a large scale map and photo. The photo on the right is from Google Maps. Figure 2.A2 shows the one-year power spectral density of vertical component (HHZ) for the station IV.MILN in 2019. Figure 2.A3 provides two more results for station IV.FIR in Florence and IV.CMSN in Naples, Italy. All websites were last accessed on May 2020.

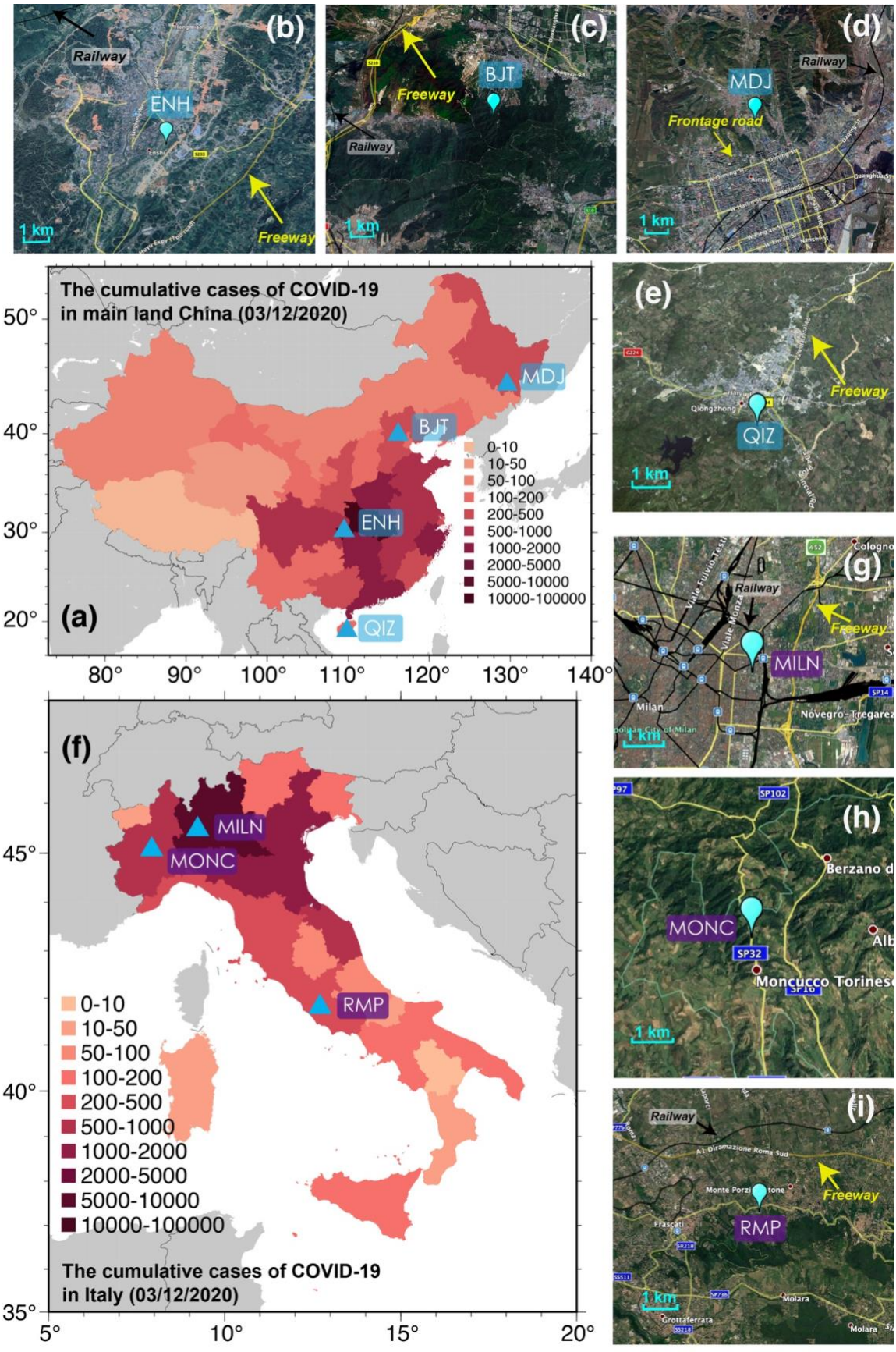
(b)
Railway
ENH
Freeway
1 km
(c)
BJT
Freeway
Railway
1 km
(d)
Railway
MDJ
Frontage road
1 km
The cumulative cases of COVID-19
in main land China (03/12/2020)
MDJ
BJT
ENH
QIZ
0-10
10-50
50-100
100-200
200-500
500-1000
1000-2000
2000-5000
5000-10000
10000-100000
(a)
50°
40°
30°
20°
80°
90°
100°
110°
120°
130°
140°
(e)
Freeway
QIZ
1 km
(g)
Railway
Freeway
MILN
Milan
Novegro - Tregarez
1 km
(f)
MILN
MONC
RMP
0-10
10-50
50-100
100-200
200-500
500-1000
1000-2000
2000-5000
5000-10000
10000-100000
The cumulative cases of COVID-19
in Italy (03/12/2020)
45°
40°
35°
5°
10°
15°
20°
(h)
SP102
MONC
SP32
SP10
1 km
(i)
Railway
Freeway
RMP
1 km
Molara

Figure 2.1. Map of stations in China and Italy. (a) The base image show the cumulative cases of COVID-19 for different provinces in mainland China as of 12 March 2020, based on data from the World Health Organization. The blue triangles indicate seismometer locations. (b) to (e) show the seismometer locations in each urban environment in China. IC.MDJ is located close to a railway line and a major road. IC.BJT is also close to the freeway and railway line but the seismometer is deployed in the deep tunnel. IC.ENH is located north west of a major freeway and south east of the local urban center. IC.QIZ is on the Hainan island and is also close to the freeway to its north. (f) Same as (a) but for Italy, highlighting seismic stations IV.MILN in Milan, IV.MONC in the area of Torino, and IV.RMC near Rome. (g) to (i) show local maps: station IV.MILN was deployed in the urban area along the railway line and freeway. Station IV.MONC is in the mountainous area. Station IV.RMP is in the suburbs 20 km southeast of Rome, Italy's capital city.

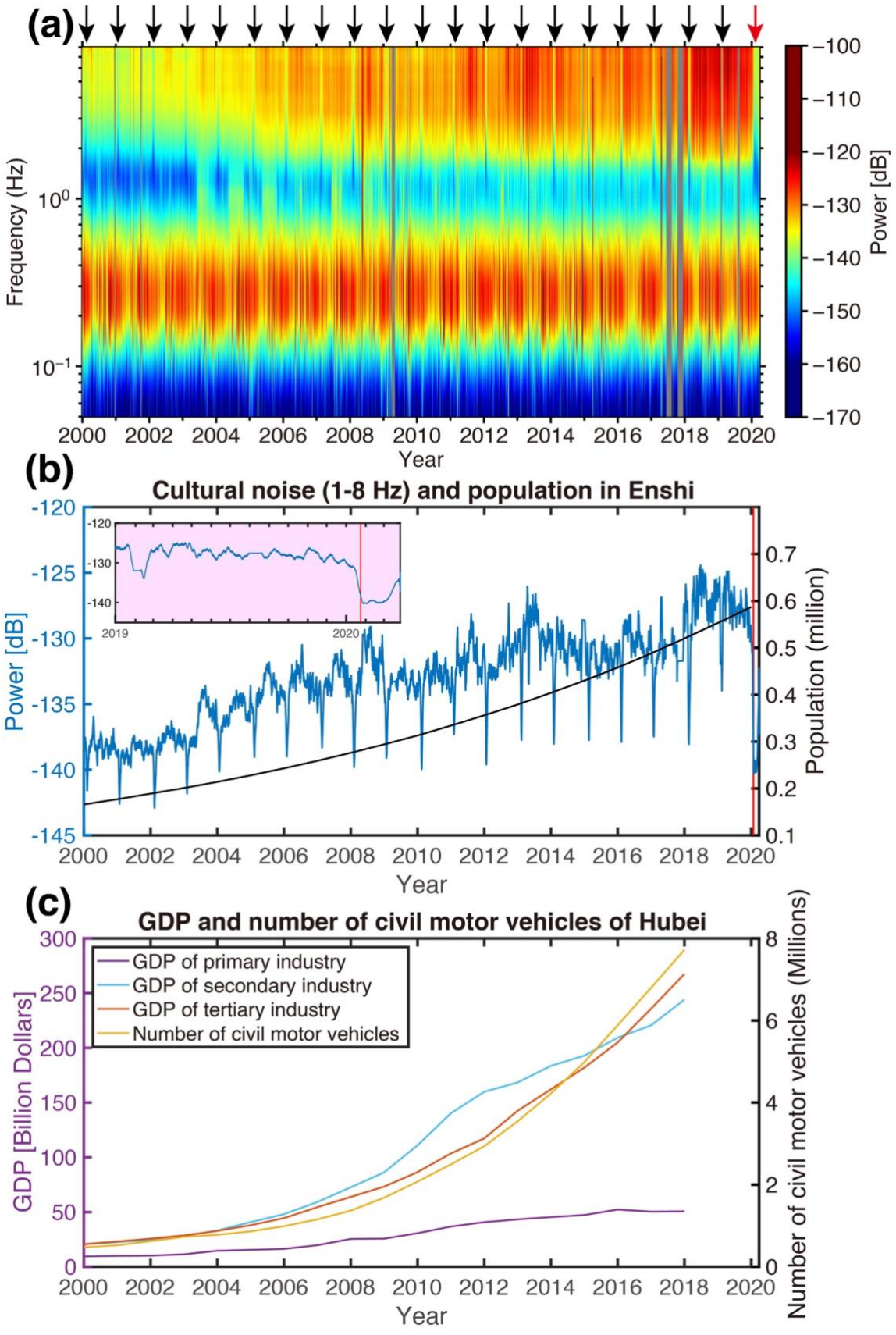
(a)
Frequency (Hz)
10^0
10^{-1}
2000 2002 2004 2006 2008 2010 2012 2014 2016 2018 2020
Year
−100 −110 −120 −130 −140 −150 −160 −170
Power [dB]
(b)
Cultural noise (1-8 Hz) and population in Enshi
Power [dB]
-120 -125 -130 -135 -140 -145
2019
2020
Population (million)
0.7 0.6 0.5 0.4 0.3 0.2 0.1
2000 2002 2004 2006 2008 2010 2012 2014 2016 2018 2020
Year
(c)
GDP and number of civil motor vehicles of Hubei
GDP of primary industry
GDP of secondary industry
GDP of tertiary industry
Number of civil motor vehicles
GDP [Billion Dollars]
300 250 200 150 100 50 0
Number of civil motor vehicles (Millions)
8 6 4 2 0
2000 2002 2004 2006 2008 2010 2012 2014 2016 2018 2020
Year

Figure 2.2. (a) Twenty years of power spectral density (PSDs) analysis for IC.ENH (Enshi, Hubei province) which has been operational since 20 September 1997. PSDs from the vertical component are shown in decibels relative to the ground acceleration with units of $10\log_{10}(\mathrm{m^2 s^{-4} Hz^{-1}})$. Black arrows indicate the timing of the Chinese Lunar New Year; the red arrow (the top-right location) indicates the time when the city went under lockdown due to COVID-19. (b) Twenty-year variation of cultural noise in the frequency band 1-8 Hz. The red line indicates the timing that Enshi went under lockdown due to COVID-19. The black line denotes the metro area population of Enshi during this period. The inset highlights the lockdown effect using a small time scale from 2019 to 2020. (c) GDP and the number of civil motor vehicles for the period 2000-2018 in Hubei province.

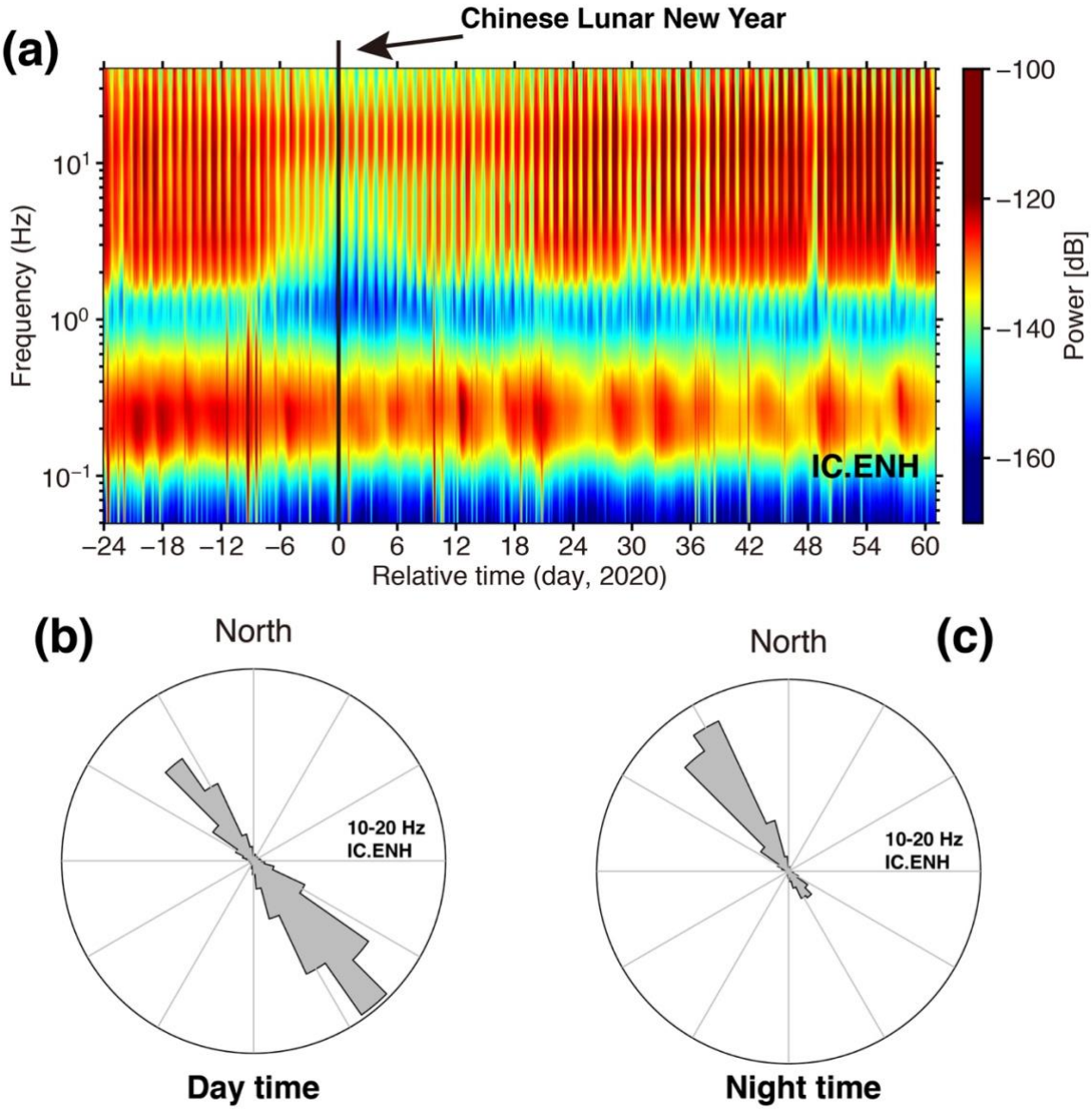

Figure 2.3. (a) Power spectral density of vertical component (HHZ) for the station IC.ENH in Enshi, Hubei province using the day of the Chinese Lunar New Year in 2018 (February 16) as a reference time. The diurnal variations of cultural noise are obvious in the PSDs; seismic noise is higher during the day than the night. Typically, the low cultural noise period is found during the Chinese Lunar New Year for a duration of about one week. (b) Distribution of back azimuths for the frequency band 10-20 Hz at daytime (7:00 a.m. to 7:00 p.m., local time) estimated from one-year data in 2018 for IC.ENH. (c) Same with (b) but at nighttime (7:00

p.m. to 7:00 a.m., local time). The source direction of cultural noise in the 10-20 Hz frequency band is from the southeast at the daytime, and from the northwest at the nighttime.

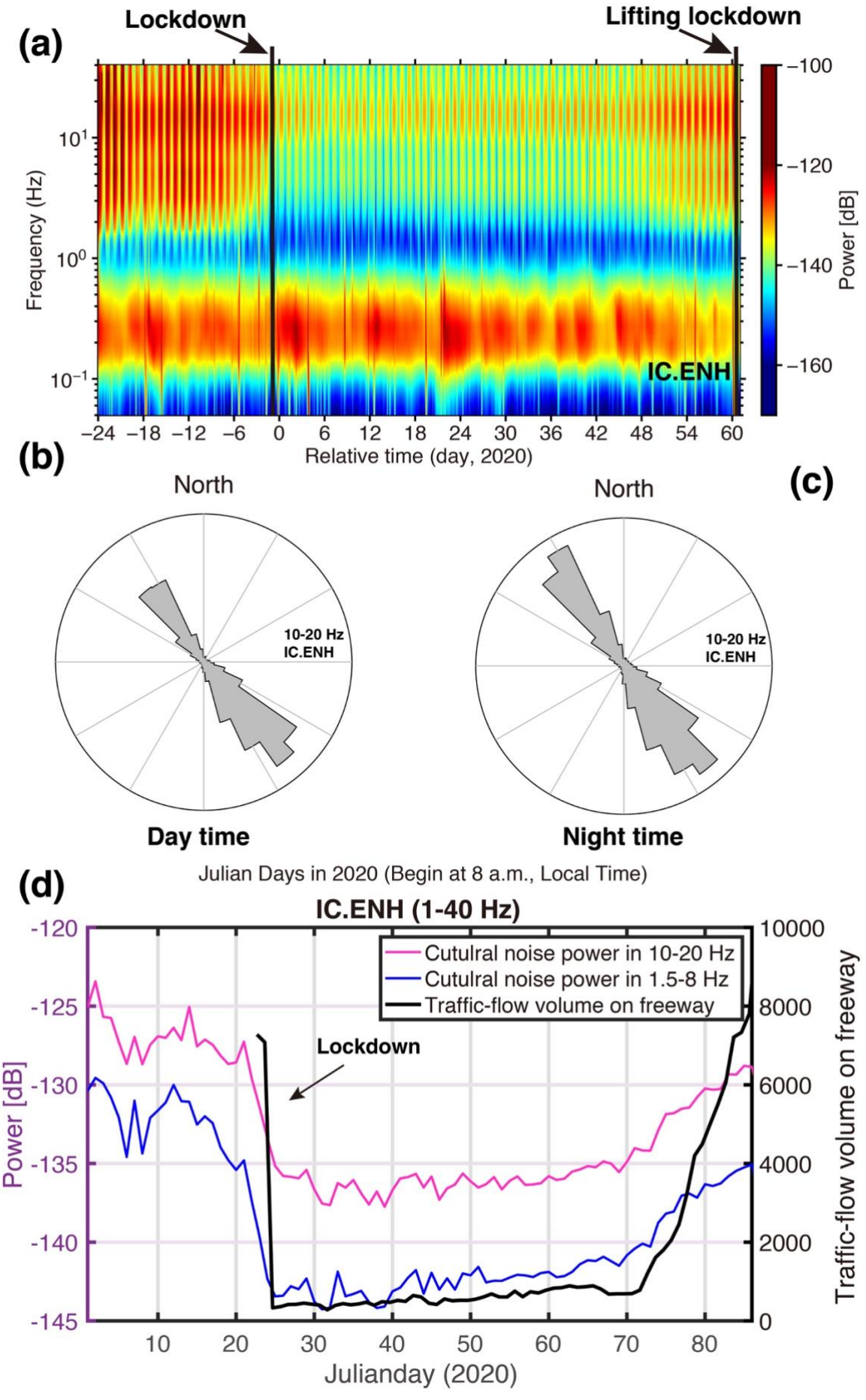
(a)
Lockdown
Lifting lockdown
Frequency (Hz)
Power [dB]
IC.ENH
Relative time (day, 2020)
(b)
North
10-20 Hz
IC.ENH
Day time
(c)
North
10-20 Hz
IC.ENH
Night time
(d)
Julian Days in 2020 (Begin at 8 a.m., Local Time)
IC.ENH (1-40 Hz)
Cutulral noise power in 10-20 Hz
Cutulral noise power in 1.5-8 Hz
Traffic-flow volume on freeway
Lockdown
Power [dB]
Traffic-flow volume on freeway
Julianday (2020)

Figure 2.4. (a) The vertical component noise PSDs for the station IC.ENH in Enshi, Hubei province using the day of the Chinese Lunar New Year in 2020 (January 25) as a reference time. The black line indicates the timing the city went under lockdown due to COVID-19. (b) Distribution of back azimuths for the frequency band 10-20 Hz at daytime (7:00 a.m. to 7:00 p.m., local time) estimated from relative days -1 to 60 when Enshi was under lockdown. (c) Same with (b) but at nighttime (7:00 p.m. to 7:00 a.m., local time). (d) Comparison of cultural noise in the frequency band 10-20 Hz (red line) and 1.5-8 Hz (blue line) with the daily traffic-flow volume.

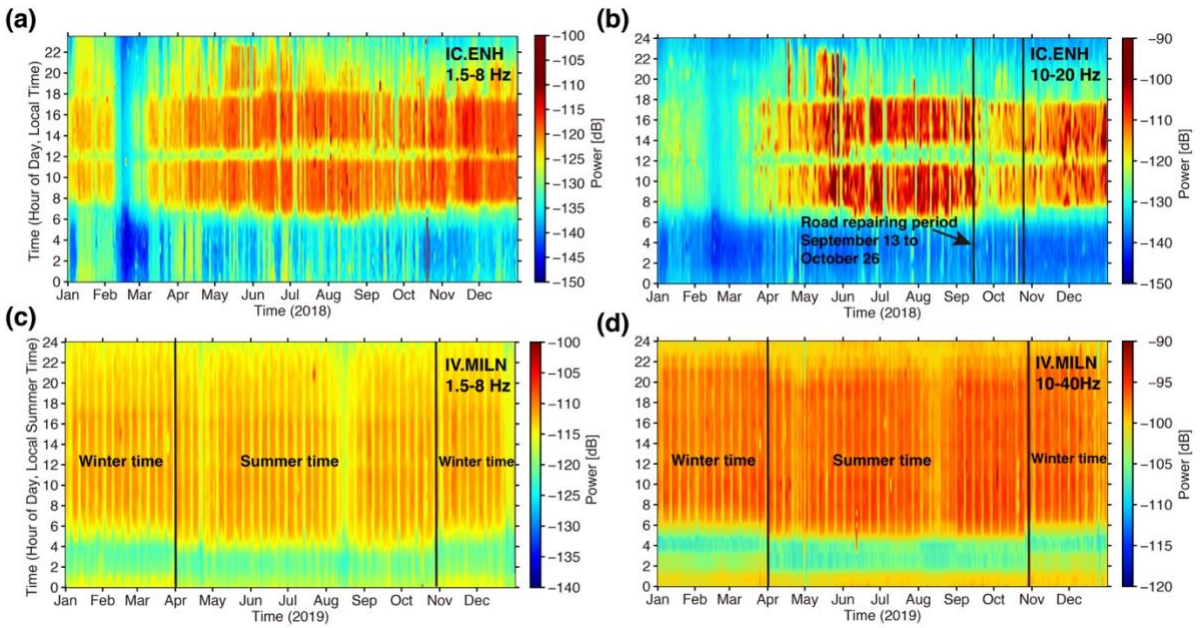

Figure 2.5. (a, b) The noise variations for the frequency band 1.5-8 Hz and 10-40 Hz in half-hour bins across the year of 2018 for the station IC.ENH in Enshi, Hubei province, China. Black lines in (b) show the repairing period of the local freeway which is located in the southeast of seismic station IC.ENH. Note there is a constant lull at 12:00 local time. (c, d) Same with (a, b) but for the station IV.MILN in Milan, Lombardy province, Italy, in 2019. The black lines show the summer time in Italy, which is from March 31 to October 27 in 2019.

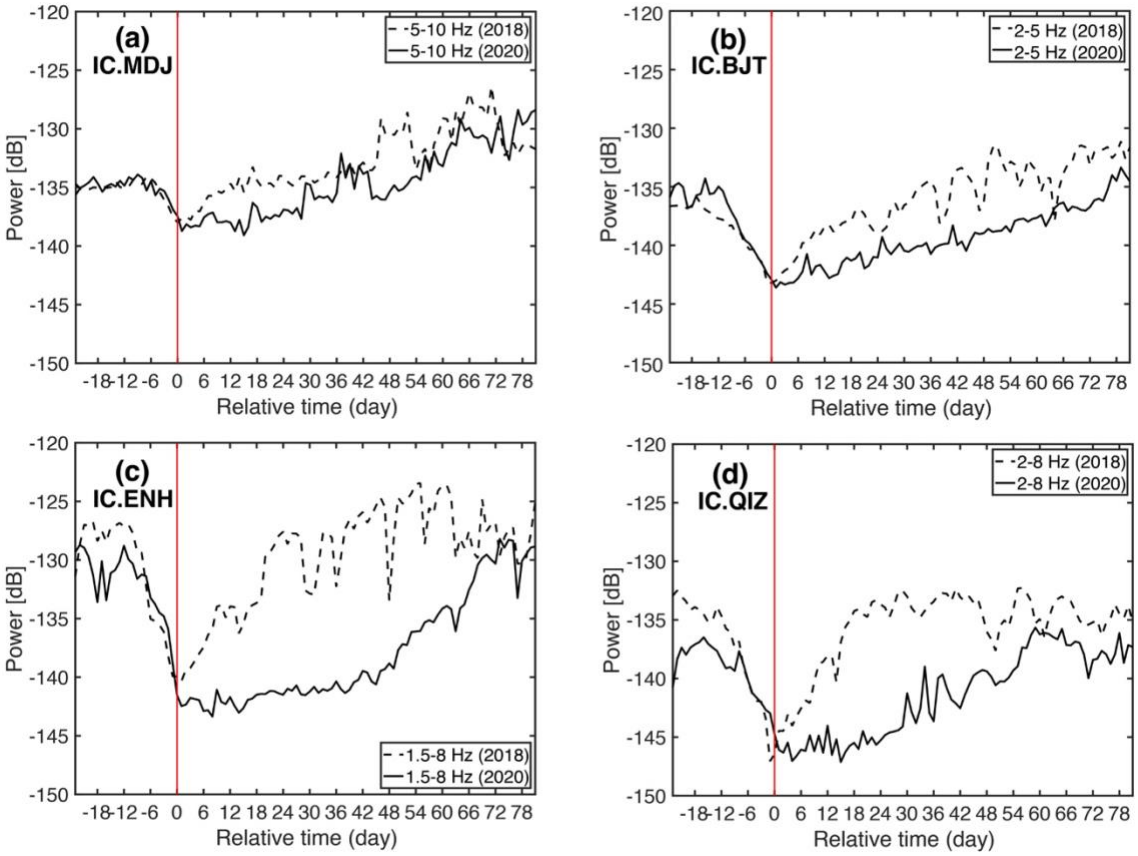

Figure 2.6. Comparison of the cultural noise power daily variation between 2018 and 2020 for the station (a) IC.MDJ (Mudanjiang), (b) IC.BJT (Beijing), (c) IC.ENH (Enshi) and (d) IC.QIZ (Qiongzhou). The time is aligned with the day of the Chinese Lunar New Year which is indicated by the red line.

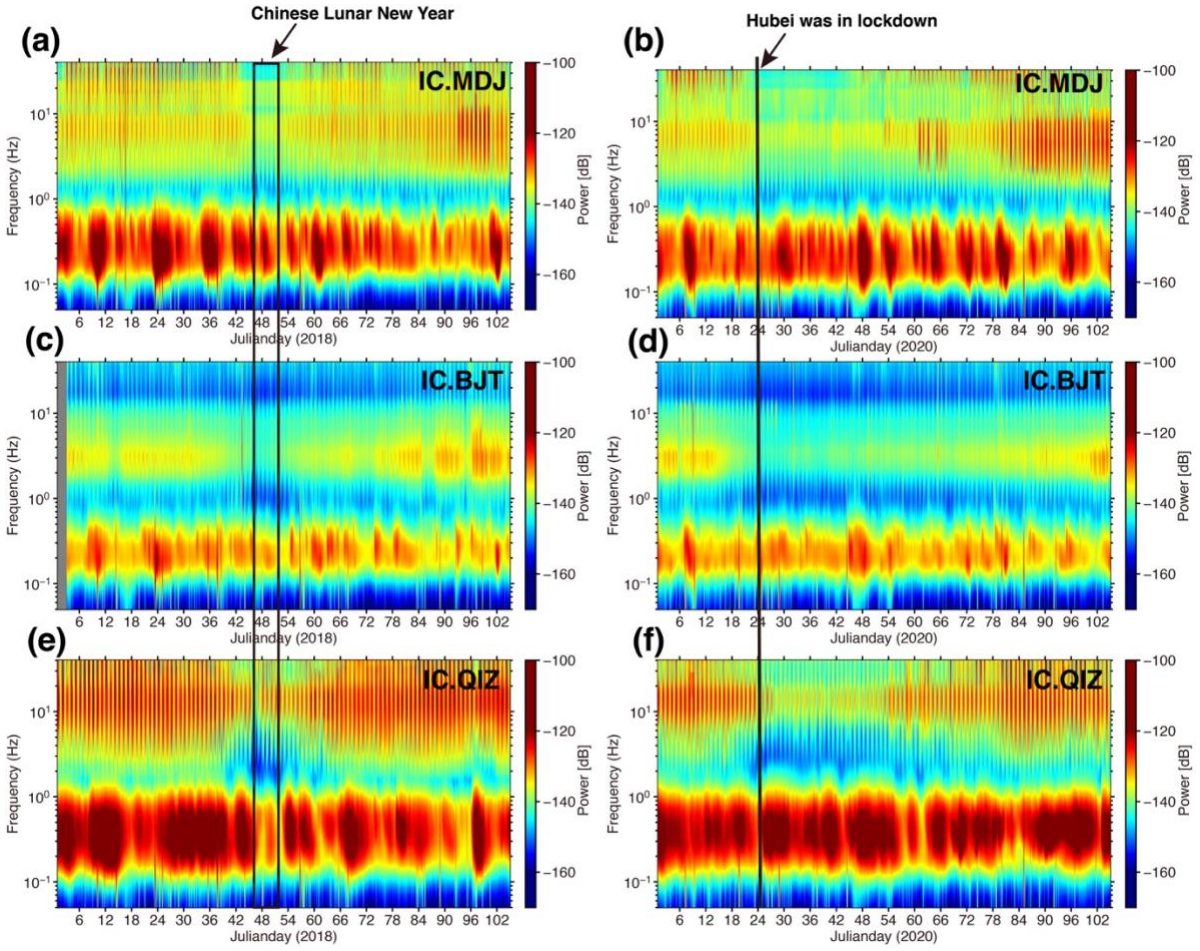

Figure 2.7. Comparison of the noise PSDs between 2018 and 2020 for the station (a, b) IC.MDJ (Mudanjiang), (c, d) IC.BJT (Beijing) and (e, f) IC.QIZ (Qiongzhou).

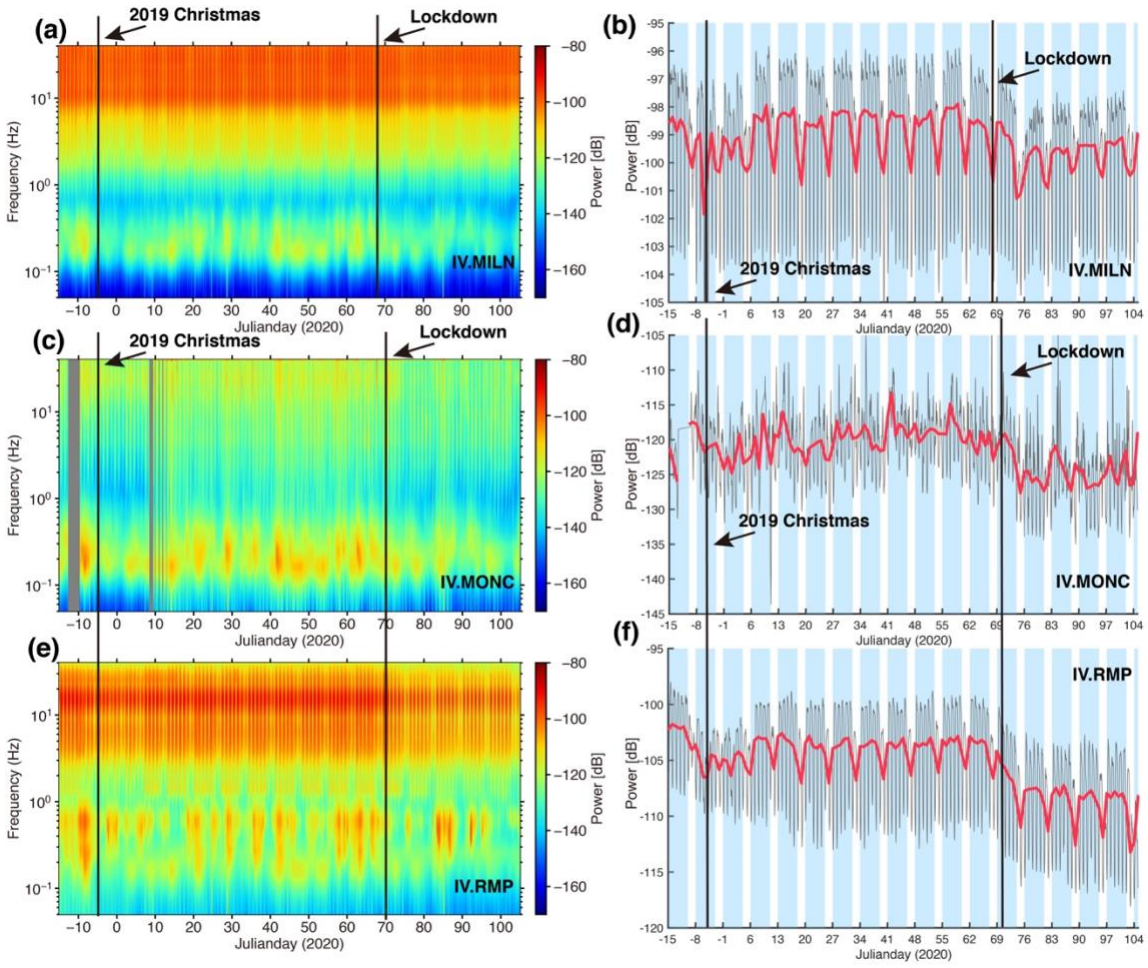

Figure 2.8. The variations of vertical-component power spectral densities at stations (a, b) IV.MILN in Milan, Italy, and (c, d) IV.MONC in the area of Torino, Italy and (e, f) IV.RMP located in ~20 km southeast of Rome, Italy. The left panels show noise power as a function of time and frequency. The black lines indicate the times that the cities where the seismic stations are located went under lockdown. The right plots show the noise variations in the frequency band 10-40 Hz. The blue background shows the time of weekdays. The grey line is plotted in half-hour bins and the red line is plotted in one-day average bins.

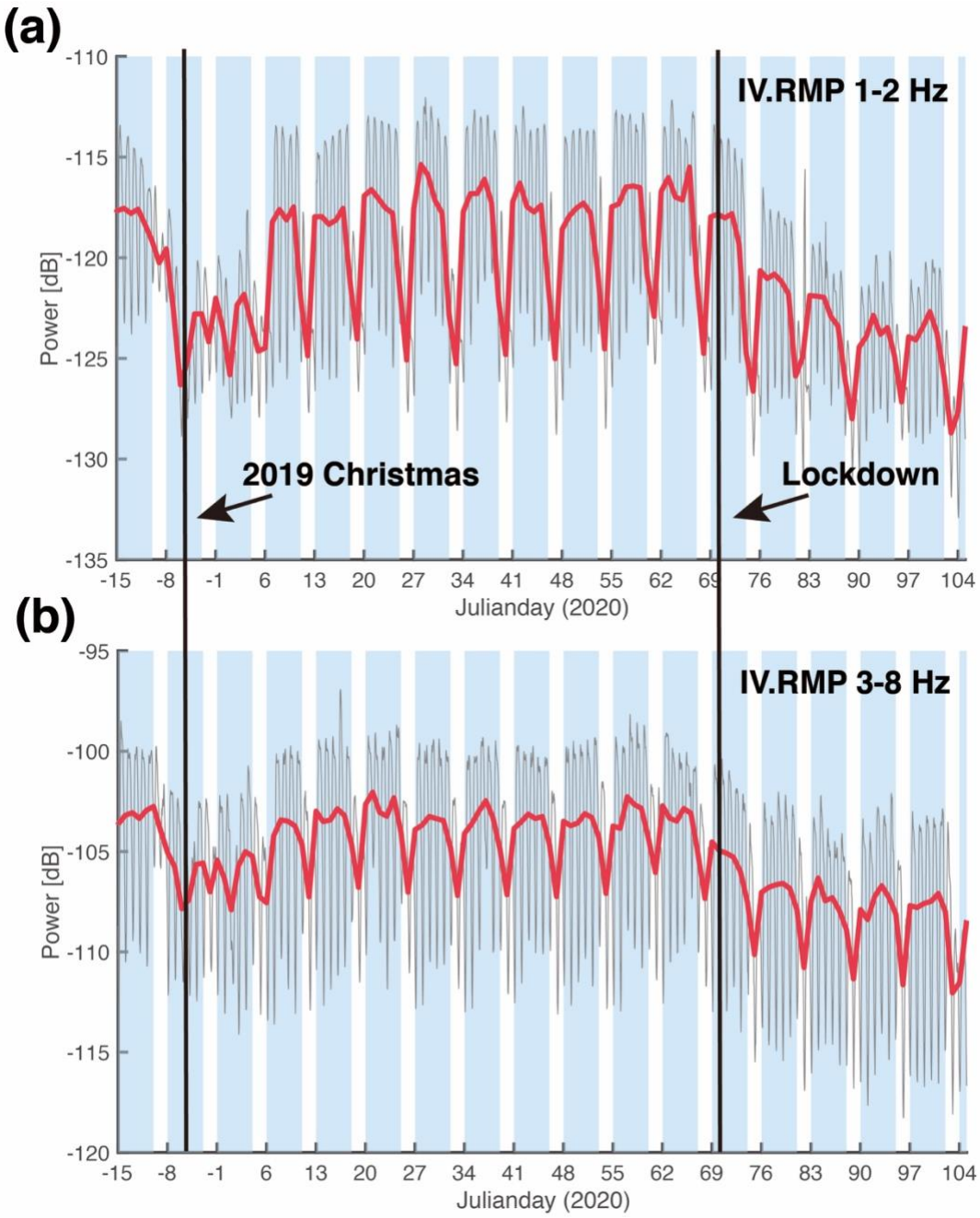

Figure 2.9. The variations of vertical-component power spectral densities at station IV.RMP (Rome, Italy) for (a) 1-2 Hz, and (b) 3-8 Hz. The blue background shows the time of weekdays. The grey line is plotted in half-hour bins and the red line is plotted in one-day average bins.

2.6 Appendix

Figure 2.A1. Rome Observatory where the station IV.RMP is located. The photo on the right is from Google Maps.

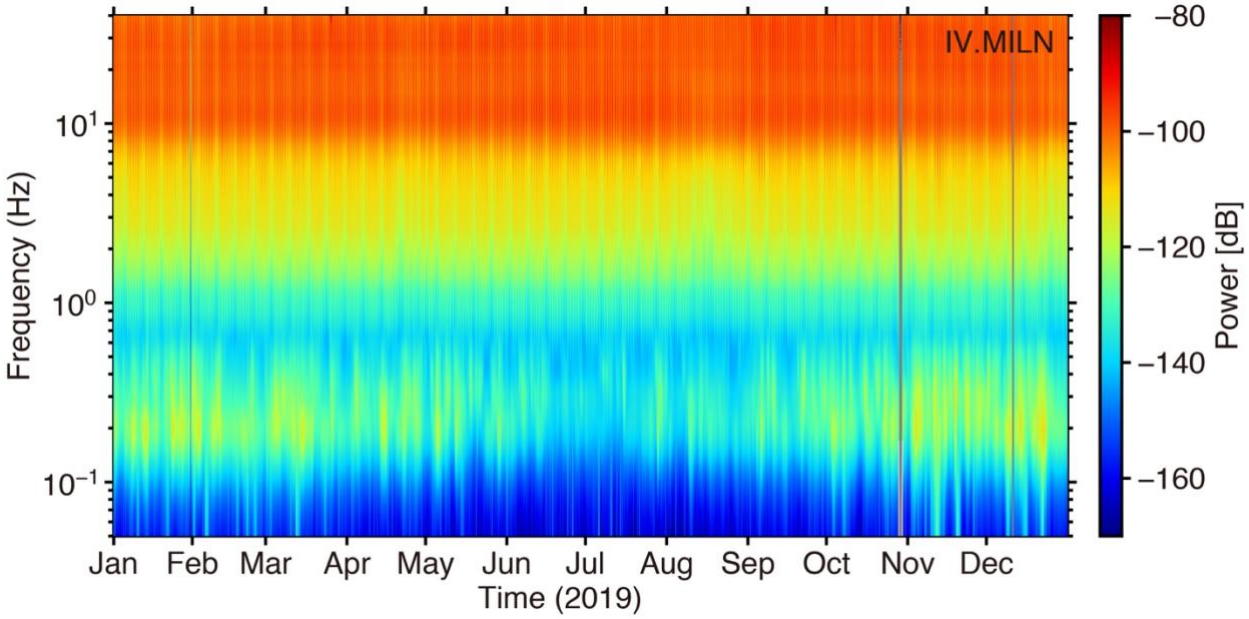

Figure 2.A2. Power spectral density of vertical component (HHZ) for the station IV.MILN in 2019.

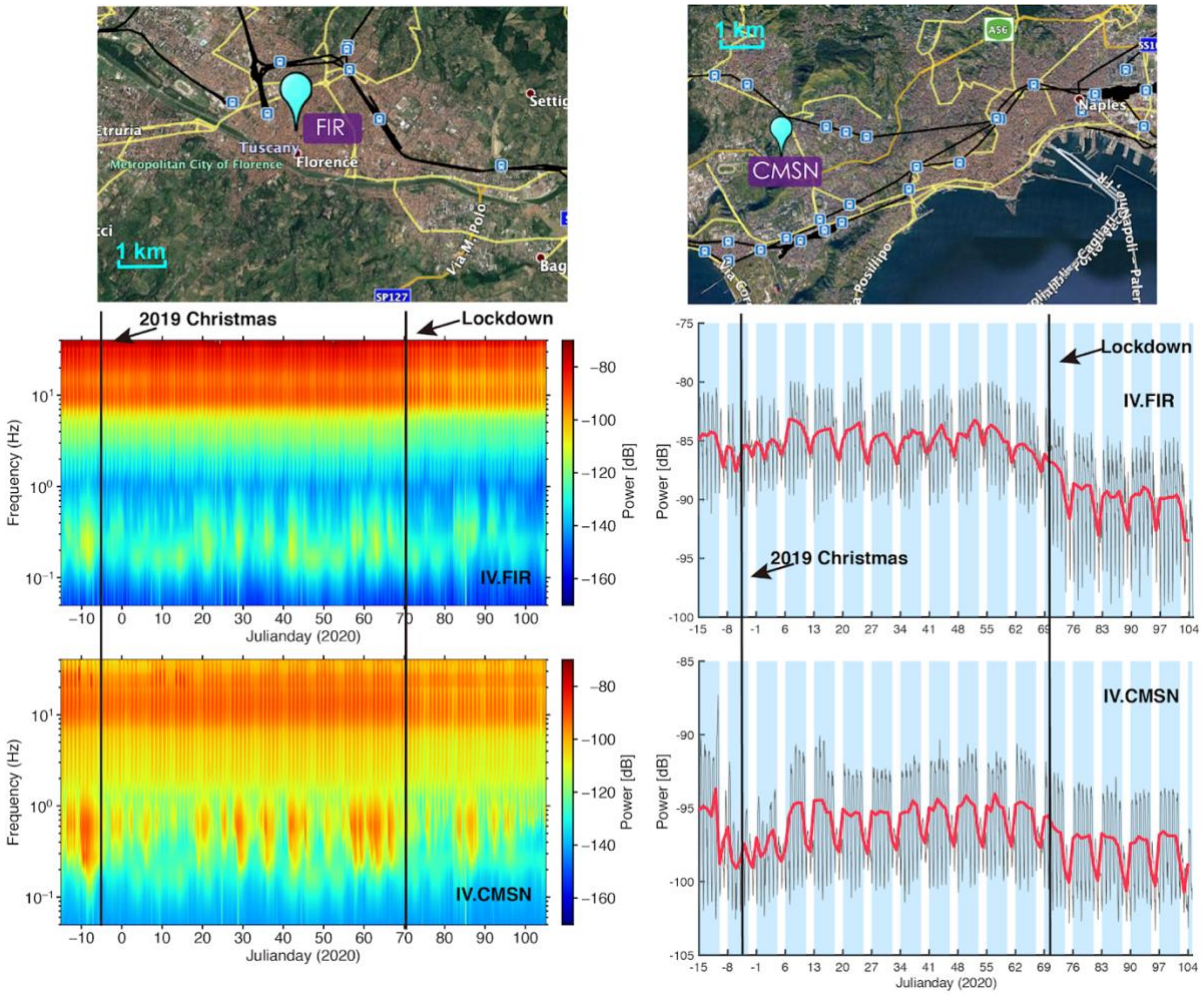

Figure 2.A3. Same as Figure 2.8 but for station IV.FIR in Florence and IV.CMSN in Naples.

2.7 References

Ajo-Franklin, J. B., Dou, S., Lindsey, N. J., Monga, I., Tracy, C., Robertson, M., et al. (2019). Distributed acoustic sensing using dark fiber for near-surface characterization and broadband seismic event detection. *Scientific reports, 9*(1), 1-14. https://doi.org/10.1038/s41598-018-36675-8

Alyamkin, S. A., & Eremenko, S. I. (2011). Pedestrian detection algorithms based on an analysis of the autocorrelation function of a seismic signal. *Optoelectronics, Instrumentation and Data Processing, 47*(2), 124-129. https://doi.org/10.3103/S8756699011020038

Andersen, K. G., Rambaut, A., Lipkin, W. I., Holmes, E. C., & Garry, R. F. (2020). The proximal origin of SARS-CoV-2. *Nature Medicine, 26*(4), 450-452. https://doi.org/10.1038/s41591-020-0820-9

Beyreuther, M., Barsch, R., Krischer, L., Megies, T., Behr, Y., & Wassermann, J. (2010). ObsPy: A Python toolbox for seismology. *Seismological Research Letters, 81*(3), 530-533. https://doi.org/10.1785/gssrl.81.3.530

Boese, C., Wotherspoon, L., Alvarez, M., & Malin, P. (2015). Analysis of anthropogenic and natural noise from multilevel borehole seismometers in an urban environment, Auckland, New Zealand. *Bulletin of the Seismological Society of America, 105*(1), 285-299. https://doi.org/10.1785/0120130288

Chang, J. P., de Ridder, S. A., & Biondi, B. L. (2016). High-frequency Rayleigh-wave tomography using traffic noise from Long Beach, CaliforniaTomography using traffic noise. *GEOPHYSICS, 81*(2), B43-B53. https://doi.org/10.1190/geo2015-0415.1

Chen, Q.-f., Li, L., Li, G., Chen, L., Peng, W.-t., Tang, Y., et al. (2004). Seismic features of vibration induced by train. *Acta Seismologica Sinica, 17*(6), 715-724. https://doi.org/10.1007/s11589-004-0011-7

Coward, D., Blair, D., Burman, R., & Zhao, C. (2003). Vehicle-induced seismic effects at a gravitational wave observatory. *Review of scientific instruments, 74*(11), 4846-4854. https://doi.org/10.1063/1.1614411

Green, D. N., Bastow, I. D., Dashwood, B., & Nippress, S. E. (2017). Characterizing broadband seismic noise in Central London. *Seismological Research Letters, 88*(1), 113-124. https://doi.org/10.1785/0220160128

Groos, J., & Ritter, J. (2009). Time domain classification and quantification of seismic noise in an urban environment. *Geophysical Journal International, 179*(2), 1213-1231. https://doi.org/10.1111/j.1365-246X.2009.04343.x

Hao, H., & Ang, T. C. (1998). Analytical modeling of traffic-induced ground vibrations. *Journal of Engineering Mechanics, 124*(8), 921-928. https://doi.org/10.1061/(ASCE)0733-9399(1998)124:8(921)

Koper, K. D., & Hawley, V. L. (2010). Frequency dependent polarization analysis of ambient seismic noise recorded at a broadband seismometer in the central United States. *Earthquake Science, 23*(5), 439-447. https://doi.org/10.1007/s11589-010-0743-5

Lu, D. (2020). Inside Wuhan's lockdown In (Vol. 245): Elsevier. https://doi.org/10.1016/S0262-4079(20)30234-7

McNamara, D. E., & Buland, R. P. (2004). Ambient noise levels in the continental United States. *Bulletin of the Seismological Society of America, 94*(4), 1517-1527. https://doi.org/10.1785/012003001

Meng, H., & Ben-Zion, Y. (2018). Characteristics of Airplanes and Helicopters Recorded by a Dense Seismic Array Near Anza California. *Journal of Geophysical Research, 123*(6), 4783-4797. https://agupubs.onlinelibrary.wiley.com/doi/abs/10.1029/2017JB015240

Nakata, N., Snieder, R., Tsuji, T., Larner, K., & Matsuoka, T. (2011). Shear wave imaging from traffic noise using seismic interferometry by cross-coherence. *GEOPHYSICS, 76*(6), SA97-SA106. https://doi.org/10.1190/geo2010-0188.1

Park, J., Vernon III, F. L., & Lindberg, C. R. (1987). Frequency dependent polarization analysis of high-frequency seismograms. *Journal of Geophysical Research: Solid Earth, 92*(B12), 12664-12674. https://agupubs.onlinelibrary.wiley.com/doi/abs/10.1029/JB092iB12p12664

Quiros, D. A., Brown, L. D., & Kim, D. (2016). Seismic interferometry of railroad induced ground motions: body and surface wave imaging. *Geophysical Journal International, 205*(1), 301-313. https://doi.org/10.1093/gji/ggw033

Riahi, N., & Gerstoft, P. (2015). The seismic traffic footprint: Tracking trains, aircraft, and cars seismically. *Geophysical Research Letters, 42*(8), 2674-2681. https://doi.org/10.1002/2015GL063558

Ribes-Llario, F., Marzal, S., Zamorano, C., Real, J., & Vibration. (2017). Numerical modelling of building vibrations due to railway traffic: Analysis of the mitigation

capacity of a wave barrier. *Shock and Vibration, 2017*. https://doi.org/10.1155/2017/4813274

Samson, J. C. (1983). Pure states, polarized waves, and principal components in the spectra of multiple, geophysical time-series. *Geophysical Journal International, 72*(3), 647-664. https://doi.org/10.1111/j.1365-246X.1983.tb02825.x

Sheen, D.-H., Shin, J. S., Kang, T.-S., & Baag, C.-E. (2009). Low frequency cultural noise. *Geophysical research letters, 36*(17). https://agupubs.onlinelibrary.wiley.com/doi/abs/10.1029/2009GL039625

Stutzmann, E., Roult, G., & Astiz, L. (2000). GEOSCOPE station noise levels. *Bulletin of the Seismological Society of America, 90*(3), 690-701. https://doi.org/10.1785/0119990025

Trnkoczy, A., Bormann, P., Hanka, W., Holcomb, L. G., Nigbor, R. L., Shinohara, M., et al. (2012). Site selection, preparation and installation of seismic stations. In P. Bormann (Ed.), *New Manual of Seismological Observatory Practice 2 (NMSOP-2)* (Vol. 2, pp. 1-139): Deutsches GeoForschungsZentrum GFZ, Potsdam, Germany. https://doi.org/10.2312/GFZ.NMSOP-2_ch7

Wessel, P., & Smith, W. H. (1991). Free software helps map and display data. *Eos, Transactions American Geophysical Union, 72*(41), 441-446. https://doi.org/10.1029/90EO00319

Withers, M. M., Aster, R. C., Young, C. J., & Chael, E. P. (1996). High-frequency analysis of seismic background noise as a function of wind speed and shallow depth. *Bulletin of the Seismological Society of America, 86*(5), 1507-1515. https://doi.org/10.1785/BSSA0860051507

WHO (2020) Director-General's Opening Remarks at the Media Briefing on Covid-19 – 11 March 2020, *World Health Organization Report* **11 March 2020,** available at https://www.who.int/dg/speeches/detail/who-director-general-s-opening-remarks-at-the-media-briefing-on-covid-19---11-march-2020.

WHO (2020) Report of the WHO-China Joint Mission on Coronavirus Disease 2019 (COVID-19), *World Health Organization Report* **28 February 2020**, available at https://www.who.int/publications/i/item/report-of-the-who-china-joint-mission-on-coronavirus-disease-2019-(covid-19).

WHO (2020) Statement on the Second Meeting of the International Health Regulations (2005) Emergency Committee Regarding the Outbreak of Novel Coronavirus (2019-Ncov), *World Health Organization Report* **30 Janaury 2020,** available at https://www.who.int/news-room/detail/30-01-2020-statement-on-the-second-meeting-of-the-international-health-regulations-(2005)-emergency-committee-regarding-the-outbreak-of-novel-coronavirus-(2019-ncov).

3. Study of S-wave Microseisms Around the Globe Using an Dense Array in Southwest China

This chapter appeared essentially in this form in:

Xiao, H., Tanimoto, T., & Xue, M. (2021). Study of S-wave microseisms generated by storms in the Southeast Australia and North Atlantic. Geophysical Research Letters, 48, e2021GL093728. doi:10.1029/2021GL093728

Xiao, H., Tanimoto, T. and Xue, M. The Origin and Seasonal Changes of S-wave Microseisms, In preparation.

3.1 Introduction

In the past twenty years, we have come to appreciate that seismic noise is quite useful for Earth structure study because we can obtain Green's functions by cross-correlating seismograms (Campillo & Paul, 2003; Shapiro et al., 2005). We have learned that the dominant seismic noise is composed of ocean-generated microseisms that are generated either by interactions between oceans waves (wave-wave interaction) or by interactions between ocean waves and the solid earth (Ardhuin et al., 2015; Ardhuin et al., 2011; Hasselmann, 1963; Kedar et al., 2008; Longuet-Higgins, 1950; Tanimoto, 2007a, 2007b; Webb, 1998). Surface waves are the dominant waves in seismic noise, including both Rayleigh and Love waves (Behr et al., 2013; Gal et al., 2017; Juretzek & Hadziioannou, 2016; Nishida et al., 2008; Tanimoto et al., 2015; Tanimoto et al., 2016), because the excitation sources are very shallow. Although modeling efforts have successfully explained seismic noise in vertical seismic spectra, including both Rayleigh waves and P waves (Ardhuin & Roland, 2012; Ardhuin et al., 2011; Gualtieri et al., 2014; Meschede et al., 2017; Stutzmann et al., 2012; Tanimoto, 2007a, 2007b; ToksöZ & Lacoss, 1968; Vinnik, 1973), the generation mechanisms of Love or SH waves have not been clear despite the fact their observations are quite robust (Juretzek & Hadziioannou, 2016; Liu et al., 2016; Meschede et al., 2017; Nishida & Takagi, 2016). Recent studies (Gualtieri et al., 2020; Gualtieri et al., 2021; Le Pape et al., 2021) have presented evidence that sediments and lateral heterogeneities can generate Love waves. In this paper, we point out that the sedimentary layer near the source regions can enhance the SH-wave signals.

In this study, we first track S-wave related signals in seismic noise, mostly body wave signals, generated by two storms in Southeast Australia and North Atlantic. We then continue our analysis of S-wave microseisms around the globe, further searching the sources and seasonal variations using two-year continuous data. We analyze each one-hour-long time series in continuous seismograms from a large aperture three-component seismic array in Southwestern China. Although the energy of body waves is smaller than that of surface waves (Koper et al., 2009; Koper et al., 2010), it has the advantage of being able to locate sources since we can get both back azimuth and an incident angle from array processing techniques, which make it possible to track deep ocean storms in real-time (Farra et al., 2016; Neale et al., 2017; Nishida & Takagi, 2016; Retailleau & Gualtieri, 2019; Ward Neale et al., 2018; Zhang, Gerstoft, & Bromirski, 2010; Zhang, Gerstoft, & Shearer, 2010). There have been compressional body waves such as P- or PP-waves (Euler et al., 2014; Gerstoft et al., 2008; Hillers et al., 2012; Landès et al., 2010; Pyle et al., 2015; Reading et al., 2014; Wang et al., 2018) as well as observations for S-wave (Liu et al., 2016; Nishida & Takagi, 2016), but the observations for SH-wave signals are still limited. The main point of this research is new observations of the SH-wave signals and their special characteristics that differ from P- and SV-wave sources.

Data and methods are discussed in section 3.2, the tracking results for the storms in Southeast Australia and the North Atlantic in section 3.3, the general characteristics of body wave microseisms from two years data in section 3.4 and their close association with thick sedimentary layer is discussed and concluded in section 3.5.

3.2 Data and methods

3.2.1 ChinArray and analysis procedure

We analyzed data from the ChinArray phase I in Southwestern China for the period from May 2011 to February 2014 (ChinArray, 2006) (Figure 3.1a). This array contained 350 portable three-component broadband stations, with a typical interstation distance of ~35 km and an aperture of ~1000 km. Each station was equipped with a Guralp CMG-3ESPC seismometer and a Reftek-130 digitizer.

In this study, we first track seismic signals from two storms when the array had its peak coverage. The first storm passed off the southeast coast of Australia from May 5 to May 10, 2012, and the second one in the North Atlantic, off the southeast coast of Greenland, from January 20 to January 30, 2013. Then we started looking at the two-year stacked results of the body wave microseisms, and their seasonal variation. Array response functions at 0.1 Hz and 0.25 Hz are shown in Figures 3.A1a and 3.A1b.

Our analysis proceeded in the following manner: the seismic waveform was obtained in velocity by removing instrument response from the original data, and then daily power spectral densities (PSDs) were calculated. We examined visually and any poor quality data were discarded at this stage. One-year averaged PSDs in the frequency band 0.05-0.3 Hz for all stations are shown in color in Figure 3.1a, which generally shows high amplitudes in the northeast and southeast parts of this array. These amplitudes indicate that seismic noise in the frequency band 0.05-0.3 Hz in this region is relatively low compared with other seismic stations around the world (Guo et al., 2020; Koper & Burlacu, 2015; McNamara & Buland, 2004; Peterson, 1993; Stutzmann et al., 2000; Xiao et al., 2018) (Figure 3.A2). This seems to

be an advantage as the low seismic noise level tends to allow detection of low-amplitude body wave signals (Reif et al., 2002).

In order to reduce effects from earthquake signals, we utilized the USGS (United States Geological Survey) earthquake catalog; we removed one hour of continuous data for each earthquake larger than magnitude 5.0. And to further reduce the effects from other transient signals, we used one-bit normalization (Bensen et al., 2007; Campillo & Paul, 2003; Shapiro & Campillo, 2004). We then calculated a two-dimensional f-k spectrum in the frequency band 0.05-0.25 Hz by performing the f-k beamforming techniques (Capon, 1969) for each hour. Capon's methods employ an optimal complex spatial weighting scheme, resulting in the minimum effect of the array response on the f-k spectrum and is quite common for ambient noise analysis. When comparing amplitudes of P- and S-wave related signals, we use the signal-to-noise ratio (SNR) as a guide for this analysis because the information on amplitudes was lost due to the one-bit normalization scheme. We defined the SNR as the seismic signal peak amplitude in the frequency-wavenumber spectrum divided by the 10 percent trimmed mean of the entire spectrum, in which the trimmed mean (Bednar & Watt, 1984; Oten & Figueiredo, 2004) can remove the outliers such as multiple seismic noise signals by excluding the highest and lowest 5 percent data values. After that, we back-projected the slowness and azimuth onto a 0.2° latitude by 0.2° longitude geographical grid using a 1D spherically symmetric Earth model AK135 (Kennett et al., 1995). For both P- and S-wave, we back-projected the seismic signals that occurred at distances between 30° and 90° from the array center. An example of array-analysis beam results for P-, SV- and SH-wave is shown in Figure 3.1b.

3.2.2 Accuracy of source location

The resolution limit of an array for locating sources depends on its aperture, configuration, the number of stations, velocity model, signal duration and the wavelength of the seismic waves that we want to observe (Bormann, 2012; Rost & Thomas, 2002). To test the locating ability of this array, we located several earthquakes that occurred in different directions and distances during the operation period using both P and S waves. We applied the same analysis and used one-bit data to calculate frequency-slowness spectra for locating earthquakes. An example of P- and S-wave analysis for the Mw 6.2 earthquake at Fox Islands (52.6°N, 167.4°W, Depth 13.0 km) on August 10, 2012, is shown in Figures 3.A1c and 3.A1d. The positioning error between the peak P-wave beam sources and the earthquake epicenter is ~280 km. For most other earthquakes, the estimated locations from the back-projection were about 200-500 km from the epicenters of the earthquakes (Table 3.A1). These location errors might be attributed to the 3D seismic structure. In order to improve the accuracy of back-projected source locations, we used two earthquakes to obtain station corrections by eliminating the averaged relative arrival-time residuals using the multi-channel cross-correlation (MCCC) method (Nishida & Takagi, 2016; VanDecar & Crosson, 1990). And, the resolution of back-projected earthquake locations after station corrections is ~100-130 km in Southeast Australia (Table 3.A2) and the North Atlantic (Table 3.A3).

3.2.3 Comparison with IFREMER source models

To further verify our back-projection source locations of seismic noises, we compared them with predicted seismic sources using the IFREMER (French Research Institute for Exploitation of the Sea) source model of ocean-induced microseisms (Ardhuin & Herbers, 2013; Ardhuin & Roland, 2012; Ardhuin et al., 2011; Stutzmann et al., 2012). This model

makes use of WAVEWATCH-III (WW3) (Tolman, 2009) to calculate the power spectral density (PSD) of equivalent pressure generated by the ocean surface gravity waves. And the output files for monthly simulations are available on the IFREMER public domain FTP site. Those outputs are global-scale models with a spatial resolution of 0.5˚ in both latitude and longitude and a temporal resolution of 3 hours. We downloaded the output files which account for the coastal reflection effects from the FTP site and compared the equivalent pressure PSD with our back-projection results. We also calculated the power spectrum of the vertical ground displacement, following the procedure described in previous studies (Ardhuin & Herbers, 2013; Ardhuin & Roland, 2012; Ardhuin et al., 2011; Stutzmann et al., 2012).

3.3 Body wave beams from two storms

We report our results for two storms, one off the southeast coast of Australia and the other off the southeast coast of Greenland. For each case, we compare the body-wave beams (P-, SV- and SH-wave) with IFREMER models and examine their association with ocean depths and sediment thicknesses on the seafloor. We searched for the exact locations of low-pressure systems but we were unable to find them. All we could find were the movement of low-pressure systems indicated by arrows in the figures (Figures 3.2a and 3.4a). We do not believe they cause any serious problems for our analysis and interpretation because seismic waves are generated by wave-wave interactions of ocean waves that are not necessarily concentrated near the center of a low-pressure system.

3.3.1 Off the southeast coast of Australia

According to ECMWF (European Centre for Medium-Range Weather Forecasts), this storm was formed in the southeast of Australia on May 5, 2012, with the maximum wind speed of 21.9 m/s, and moved to the southwest in the next two days (Figure 3.2a). Black arrows show the movement of this storm over about five days. The longitudes (top) and latitudes (bottom) of P-wave (blue) and SH-wave (green) sources are shown in Figure 3.2b. Same for SV-wave sources (purple) are shown in Figure 3.2c, plotted with the same P-wave sources. Size of symbols indicate the strength of this storm, quantified from SNR as discussed in (3.2.1), and the variations of P-wave and SV-wave sources show similarities in Figure 3.2c; both are weak on May 6 but became strong on May 7 and remained so for a little longer than a day. On the other hand, strength variations of SH-wave sources are different from them as they were strong on May 6 and the earlier part of May 7 but became weak for the latter part of May 7. These strength variations show distinct differences between SH-wave sources and P- and SV-wave sources.

The same features can also be seen in Figure 3.3a; when the storm moved from about 40°S to 50°S, SH-wave sources (green) were distinctly large. In terms of timing, this was from May 6 to earlier part of May 7 (Figure 3.2b). P-wave (blue) and SV-wave (purple) sources got stronger near 50°S on May 7 and remained strong as the storm moved southward to about 55°S. They thus indicate that SH-wave sources were strong initially but P- and SV-wave sources became large later.

Figure 3.3a also shows that the combined region for the strong SH-wave sources and the P- and SV-wave sources coincide with the strong PSD of ocean wave equivalent pressure predicted by the IFREMER source model. We obtained the pink region in Figure 3.3a by

stacking the IFREMER pressure PSD from May 5 to May 10, 2012. The pink region basically encapsulates the source regions of all back-projected body wave sources and this agreement does not seem to be fortuitous.

This encapsulating pink source region seems to imply that the storm was strong and capable of generating body waves throughout the entire period (May 6-8 as in Figure 3.2). But somehow, the switching from the SH-wave source to P- and SV-wave sources occurred on May 7. What could possibly be the reason for this switching?

We propose that the answer is in the distribution of thick sedimentary layers. Figure 3.3b shows the locations of SH-wave sources plotted over the sediment thickness map; the thickness of sediments on the ocean floor is indicated by white to black shades in this figure, with the strongest black reaching 1200 m in sediment thickness. There are approximately two broad regions of strong SH-wave sources in Figure 3.3b (shown in green dots), one on the east side of Tasmania and the other just south of Tasmania. These two locations match with dark grey to black regions in Figure 3.3b, suggesting that SH-wave sources exist at locations with thick sediments. It is also important that SH-wave sources became weak as the storm moved to the south of 50°S where sediments are thin.

At the same time, there is no clear connection between SH-wave source locations with ocean depths or bathymetry gradients (Figure 3.3c, Figures 3.A3a and 3.A3b). This is clear from the fact that one of the strong SH-wave sources exists at deep ocean sites (east of Tasmania), while the other strong SH-wave sources exist at shallow ocean sites (south of Tasmania). Therefore, strong SH-wave sources are located in both shallow and deep ocean regions.

All of the above discussions were based on body-wave signals at 0.14 Hz. As Figure 3.3d shows, the (normalized) power distributions of P-wave (blue line), SV-wave (purple line), and SH-wave (green line) peak at about 0.14 Hz. The SNR of SV-wave and SH-wave at 0.14 Hz is about 26% and 18% of P-wave, respectively. We note that there is a peak at 0.18 Hz, and that the major sources are from where the storm started on May 5 and May 6 (Figures 3.A4a and 3.A4b). The ocean depth-related resonant frequencies are also approximately 0.18 Hz in those places (Ardhuin & Herbers, 2013; Farra et al., 2016; Gualtieri et al., 2014; Meschede et al., 2017). A local seismic station II.TAU in Tasmania has also observed different frequencies of seismic waves when the storm is at different locations (Figures 3.A4c and 3.A4d), which proves that our observations are accurate. Besides, the SNR of SH-wave at 0.18 Hz is relatively low, which may be due to the different resonance frequencies of the local sediments.

3.3.2 Off the south coast of Greenland: North Atlantic site

This example has three extratropical cyclones in the North Atlantic near Greenland from January 20 to January 30, 2013 (Figure 3.4a). According to the forecast by ECMWF, the highest wind speed during this period was 27.5 m/s on January 26. The black arrows in Figure 3.4a show the tracks of three extratropical cyclones, and the red dots indicate two local earthquakes that were used for station corrections. Similar to Figures 3.2b and 3.2c, Figures 3.4b and 3.4c show the movement of the P-wave (blue dots), and SH-wave (green dots), and SV-wave (purple dots) sources in longitude (top) and latitude (bottom). In general, the P-, SH- and SV-wave sources follow the cyclones tracks in Figure 3.4a closely.

Similar to Figures 3.3a-3.3c, Figures 3.5a-3.5c show the geographic locations of seismic noise sources with the same pattern. Figure 3.5a illustrates that the seismic noise observations

are consistent with predicted sources by the IFREMER pressure PSD model (pink region). The P- and SV-wave sources are spread out from southeast to northwest in Figure 3.5a. On the other hand, strong SH-wave sources primarily exist in regions with thick sediments (black regions) such as on the east coast of Greenland and the east side of the Mid-Atlantic Ridge (Figure 3.5b) (Nishida & Takagi, 2016). There is a region of thin sediments between them, approximately coinciding with the Mid-Atlantic Ridge.

We also found that there is no clear correlation between SH-wave source locations and ocean bathymetry (Figure 3.5c). We also checked ocean bathymetry gradients but they were also not correlated with SH-wave source locations (Figures 3.A3c and 3.A3d). These facts support that the amplitude enhancement by thick sedimentary layers is an important process for generating SH-wave microseisms. It is worth noting that the dominant frequency of SH-wave is 0.14 Hz which is similar to the P- and SV-wave (0.15 Hz) in the North Atlantic (Figure 3.5d). And the SNR of SV-wave and SH-wave is about 29% and 9% of P-wave at 0.14 Hz for this region.

3.4 General characteristics of body wave microseisms from two years data

3.4.1 Two years stacked results for P-, SV-, and SH-wave over 2011-2013

In order to locate the source regions of P- and S-wave, we back-projected the stacked beamforming results from 2011 to 2013 in the frequency band 0.11-0.19 Hz (Figures 3.6a-3.6c). There are multiple P-wave microseisms sources regions in the northern and southern hemispheres (Figure 3.6a), such as the North Atlantic, North Pacific, Gulf of Alaska, southern Madagascar, Kerguelen Plateau, eastern and southeastern Australia. And the maximum power

of P-wave in the frequency band 0.11-0.19 Hz is from the South Indian Ocean, especially near the Kerguelen Plateau (Figure 3.6a). Those P-wave source regions are consistent with earlier studies (Gerstoft *et al.*, 2008; Zhang *et al.*, 2010; Euler *et al.*, 2014; Reading *et al.*, 2014; Gal *et al.*, 2015; Pyle *et al.*, 2015; Wang *et al.*, 2018). At the same time, the positions of these back-projection sources are consistent with the high PSD area of the simulated ocean wave equivalent pressure (Figure 3.6e). Similarly, the SV-wave sources are also found in the same regions as the P-wave sources, but the power is much lower (Figure 3.6b). However, as shown by Figure 3.6c, compared with the P- and SV-wave, the SH-wave has a much smaller distribution area and only appears around the thick sedimentary layer (Indicated by the blue circles in Figure 3.6d). For example, in the southern Madagascar, although the power of P- and SV-wave is high (Indicated by the pink circle in Figures 3.6a and 3.6b), the power of SH-wave is very low (Figure 3.6c). At the same time, it can be seen from Figure 3.6d that the thickness of the sedimentary layer in this area is relatively thin, indicating the sedimentary layer play an important role in the generation of SH-wave microseisms (Xiao *et al.*, 2021). Therefore, we speculate that SH-wave may be converted from P- or SV-wave in the sediments layer.

In order to further study the distribution of SH-wave, we have back-projected one-year (2012) stacked noise sources of SH-wave at each frequency in Figure 3.7. We found that SH-wave of different frequencies come from different regions. For example, for 0.11 Hz, the seismic noise of SH-wave mainly comes from the southeastern part of the Kerguelen Plateau, and for 0.12 Hz, the noise mainly comes from the Kerguelen Plateau and Gulf of Alaska. From 0.13 Hz to 0.16 Hz, the SH-wave seismic noise comes from multiple regions, including the North Atlantic, North Pacific, Gulf of Alaska, Kerguelen Plateau, and Southeast Australia.

Among them, the power of 0.14 Hz SH-wave is the largest. At the same time, we can see that there are some SH-wave from northeast Australia at 0.13 Hz, and very weak SH-wave from southern Madagascar at 0.14 Hz and 0.15 Hz. For higher frequencies, the 0.17 Hz SH-wave mainly comes from the North Atlantic Ocean, Northeast Japan, Kerguelen Plateau and Southeast Australia. The 0.18 Hz SH-wave comes from the North Atlantic Ocean, Kerguelen Plateau, eastern and southeastern Australia. But for 0.19 Hz, SH-wave almost only come from eastern Australia. In general, although SH-wave of different frequencies come from different areas, they have one thing in common that they basically only come from those areas with thick sediments (Figure 3.6d).

3.4.2 Seasonal variations of P-, SV-, and SH-wave

Figure 3.8 shows the seasonal variation of the noise source at 0.14 Hz. This analysis shows that P-, SV-, and SH-wave share similar source regions in the different seasons. In the northern hemisphere springtime, the main sources of P-wave microseisms are located near the Kerguelen Plateau and northeastern Australia (Figure 3.8a). Some weak sources of noise have been found in the northern hemisphere, including the Central Pacific and North Pacific, as well as the North Atlantic along the Greenland coastline. For SV-wave sources (Figure 3.8b), the clear energy is still found in the same regions with P-wave, most notably near the Kerguelen Plateau and the Northern Pacific Ocean, and a lesser extent in the Northern Atlantic Ocean and the south of Madagascar. However, for the SH-wave source (Figure 3.8c), the energy mainly comes from the Kerguelen Plateau where the sedimentary layer is relatively thick (Figure 3.7d), while the power in the Central Pacific and North Pacific is weak. P-, SV- and SH-wave sources show similar behavior in summer and autumn (Northern hemisphere),

and the strong sources tend to gather in the Kerguelen Plateau and southeastern Australia (Figures 3.8d-4.4i). At the same time, there are still some P-wave signals arriving from the Northern Atlantic Ocean in both summer and autumn (Figures 3.8d and 3.8g), and from the central Pacific Ocean in autumn (Figure 3.8g). It is worth noting that the weak energies of SV- and SH-wave also appear in the Mid-Pacific and North Pacific in autumn (Figures 3.8h and 3.8i), but the source locations are slightly different from the P-wave. In the northern hemisphere wintertime, the microseisms sources of P-wave are found in the source areas similar to that in spring, but there are strong sources in the North Atlantic and North Pacific (Figure 3.8j). SV- and SH-wave sources are mainly located in the Northern Pacific Ocean and the Northern Atlantic Ocean (Figures 3.8k and 3.8l). In the meantime, the clear SV-wave energy arrives from several discrete sources in the Southern Indian Ocean such as the south of Madagascar, the Kerguelen Plateau, and the west side of Australia, while there is no obvious SH-wave generated in the Southern Hemisphere.

At the frequency of 0.17 Hz (Figure 3.9), the noise sources are different from 0.14 Hz (Figure 3.8), especially for SH- and SV-wave. For example, in the springtime of the northern hemisphere, the strongest SH-wave noise source comes from the northeastern of Japan and the North Atlantic (Figure 3.9c) instead of from the Kerguelen Plateau like the 0.14 Hz (Figure 3.8c). At the same time, the SV-wave in the North Pacific is also closer to the northeastern of Japan (Figure 3.9b). And the SV-wave noise in southern Madagascar is stronger than that at 0.14 Hz (Figure 3.8b). In the northern hemisphere summertime (Figures 3.9d-4.5f), the distribution of noise sources of P-, SV- and SH-wave is similar to 0.14 Hz, but the power is much weaker. In the northern hemisphere autumntime (Figures 3.9g-4.5i), P-wave come from different sources, such as southern Madagascar, Kerguelen Plateau, southeastern Australia,

North Atlantic, North Pacific, and southeastern Japan. However, the noise power of S-wave microseisms is very low and mainly comes from the northern hemisphere, such as the North Atlantic and North Pacific. Only some weak SV-wave comes from southern Madagascar, Kerguelen Plateau and southeastern Australia, and very weak SH-wave energy comes from the Kerguelen Plateau, which is completely different from 0.14 Hz (Figures 3.8h and 3.8i). In wintertime (Figures 3.9j-4.5l), P-, SV- and SH-wave mainly come from the northern hemisphere, such as the North Atlantic Ocean, North Pacific Ocean, and the seas of northeastern Japan. But there still some weaker P- and SV-wave microseisms are generated in southern Madagascar and Kerguelen Plateau.

3.4.3 Time variations for P-, SV-, and SH-wave in 2012

The results from sections 3.1 and 3.2 show that the global P- and S-wave microseisms sources present seasonal changes. To further examine the time variations in seismic noise sources, we analyzed the daily changes of power for both P- and S-wave in each noise source area in 2012. Figure 3.10 shows the normalized beam power of P-wave (blue line), SV-wave (purple line), and SH-wave (green line) in the frequency band 0.05-0.25 Hz as a function of time in the North Atlantic, the North Pacific, the Kerguelen Plateau, and the Southeastern of Australia. All three types of body waves in the four regions show similar behaviors, with the maximum SNR in the local winter and the minimum SNR in the local summer, which is consistent with the local ocean wave dynamics. Besides, it can be seen from Figure 3.10 that the power of these body waves is not continuous, but generated by individual storms, which is also consistent with the actual ocean conditions. The most interesting part is that the power of the SH-wave changes over time differently from the P- and SV-wave. That is to say,

although sometimes the power of P- and SV-wave is very high, the power of SH-wave is very low, as shown by the black vertical arrows in Figure 3.10. And from the previous discussion, we know that this is because SH-wave can only be generated in the sedimentary layer. Another interesting feature is that even though the P-wave signal is very strong, there are occasionally no SV-wave. This may indicate that the conversion of P-wave to SV-wave requires additional conditions, such as the angle of incidence to the seabed when the conversion occurs.

3.4.4 Statistical analysis for P-, SV-, and SH-wave in 2012

In order to understand the P- and S-wave distribution of different frequencies, we visually check the beamforming results every day and count the distribution of P-, SV- and SH-wave signals in 2012 (Figure 3.11a). We can see that the number of days of clean P-wave signals surged from 0.05 Hz for 5 days a year to 0.14 Hz for 348 days a year, and remained at the same level, up to 0.23 Hz. However, the statistical distribution of S-wave signals including SV- and SH-wave is different from P-wave in that they are normally distributed. The peak frequency of the SV-wave is 0.15 Hz, which can be observed on 249 days in a year, and the peak SH-wave frequency is 0.14 Hz, which can be clearly observed on 153 days in a year. Figures 3.11b-4.7f show the normalized SNR distributions of P-wave (blue line), SV-wave (purple line) and SH-wave (green line) sources in different regions at different frequencies. The statistics of P-wave sources show that the highest peak in the North Atlantic Ocean is 0.16 Hz (Figures 3.11c), and the highest peak in the North Pacific Ocean is 0.19 Hz (Figure 3.11d), which is consistent with the results of Meschede *et al.* (2017). At the same time we can see the highest peak in Kerguelen Plateau is at 0.17 Hz (Figure 3.11e). An interesting feature of the P-wave source in southeastern Australia is that there are two different spectral

peaks at 0.15 Hz and 0.22 Hz (Figure 3.11f). This is because there are two different seismic sources in this area, and their main noise frequencies are different due to the influence of water depth, which has been confirmed in our previous research (Xiao *et al.*, 2021). The S-wave sources in North Atlantic and southeastern Australia, including both SV- and SH-wave, have similar spectral peaks with P-wave. However, the peaks of S-wave in the North Pacific and Kerguelen Plateau are 0.15 Hz and 0.13 Hz, which are different with the local P-wave (0.19 Hz and 0.17 Hz). One possible reason is that, unlike P-wave, the amplitude and dominant frequency is controlled by the local ocean pressure source and water column resonance (Meschede *et al.*, 2017), other geological features, such as the resonance frequency of sediments of different thicknesses, may be critical to the generation of SH-wave. Besides, the power ratio between S- and P-wave in different regions is different, such as 10.6% for SV-wave and 2.5% for SH-wave in the North Atlantic, 2.5% for SV-wave and 1.5% for SH-wave in the North Pacific, 2.4% for SV-wave and 1% for SH-wave in the Kerguelen Plateau, and 6% for SV-wave and 1.4% for SH-wave in southeastern Australia.

3.4.5 Power ratio of P- and SH-wave under different sediments thickness

To further understand the relationship between SH-wave and the thickness of the sediments layer. As shown in Figure 3.12, we summarized and plotted the SNR of P- and SH-wave as a function of sediment thickness based on two years data. At 0.14 Hz (Figure 3.12a), the maximum P-wave power cluster around those areas where the thicknesses of sediments less than 200 m since the sediments are generally thin corresponding to the most source regions of P-wave microseisms. In contrast, the SH-wave peaked at approximately 960 meters in thickness of the sediment. Figure 3.12b shows the SH-wave/P-wave SNR ratio at different

thicknesses of the sediments for different frequencies. The maximum ratio is found at 960 m for 0.14 Hz with a value of ~0.25. For other frequencies, 0.12 Hz has a peak ratio of 0.12 at ~840 m, and 0.16 Hz has a peak ratio of 0.19 at ~1140 m. Those peak depths generally match the expected thickness of the sedimentary layer inferred from resonant frequencies of SH-wave (Van Der Baan, 2009).

3.4.6 Example of Pg-, PkP-, PS- and ScS-wave in microseisms

Although this research focuses on S-wave microseisms, it is worth mentioning that we have also discovered many other phases of body waves. For example, we found Pg-wave signals with a group velocity around 19 s/deg (5.8 km/s) in one-year (2012) stacked radial component beamforming result in the frequency band 0.1-0.2 Hz (Figure 3.13a). The Pg-wave signals arrival from different directions including north and west for which the array is far away from the ocean. And we also observe PKP-wave, including PKP_{ab}, PKP_{bc}, PKP_{df} in our daily beamforming results (Figure 3.13b). Moreover, assuming that the different phases are from the same source region, we also observe PS- and ScS-wave in the radial and transverse components (Figures 3.13c, 3.13d and Figures 3.A5, 3.A6). Sometimes, we can also detected PP-wave in our results which is often considerably attenuated by its long upper-mantle path. Although it always appears along with the P-wave in the Northern Atlantic Ocean and the Southern Pacific Ocean (Wang *et al.*, 2018), they have to be examined with care because they can be explained as a direct P-wave with half the distance. In this study, using P- and S-wave as references, if we perform back projection, we can more confidently distinguish PP-wave because they come from the same source area as other sources. However, we will not discuss

PP-wave, but mainly focus on P- and S-wave, which have the strongest signals in our observations.

3.5 Discussion and conclusions

In this study, the array in the southwest China has provided an unprecedented view of global S-wave microseisms field. We found clear P- and S-wave microseisms signals in the beamforming results, and they have obvious seasonal changes. Not surprisingly, the P-wave microseisms sources and seasonal changes we observed are consistent with the previous studies (Euler *et al.*, 2014; Gal *et al.*, 2015; Pyle *et al.*, 2015; Wang *et al.*, 2018).

According to our one-year average global result (Figure 3.11b), the SNR of SV- and SH-wave is about 5% and 1.5% of P-wave, respectively. During the storm period, especially when the storm passes through areas with thick sediments, the SNR of SV- and SH-wave can reach 30% and 18% of P-wave, respectively (Xiao *et al.*, 2021). However, according to the prediction from a model for the excitation of body waves (Gualtieri *et al.*, 2014), the relative power of SV-wave that converted from the multiply reflected P-wave in the water column at the interface between the ocean and the solid earth is only about 1% of P-wave. Therefore, it is possible that P-wave can also generate P-to-SV converted phases at sharp interfaces below the ocean bottom.

Our primary motivation for this study was to improve our understanding of the generation mechanism and source locations of SH-wave. Based on two years seismic data recorded by an array in China, we demonstrated that the locations of SH-wave sources coincide with regions of thick sediments. Recent studies (Gualtieri *et al.*, 2020; Gualtieri *et al.*, 2021; Le Pape *et al.*, 2021) reported that the Love-wave microseisms are generated by sediments and

lateral heterogeneities in Earth structure. We generally agree with their statements but what we have shown in this paper is the direct evidence that amplitude enhancement by a sedimentary layer is important for SH-wave generation in seismic noise. The dominant frequency of SH-wave is different in different regions. This may be related to the thickness of the local sedimentary layer and its resonance frequency (Figure 3.12b).

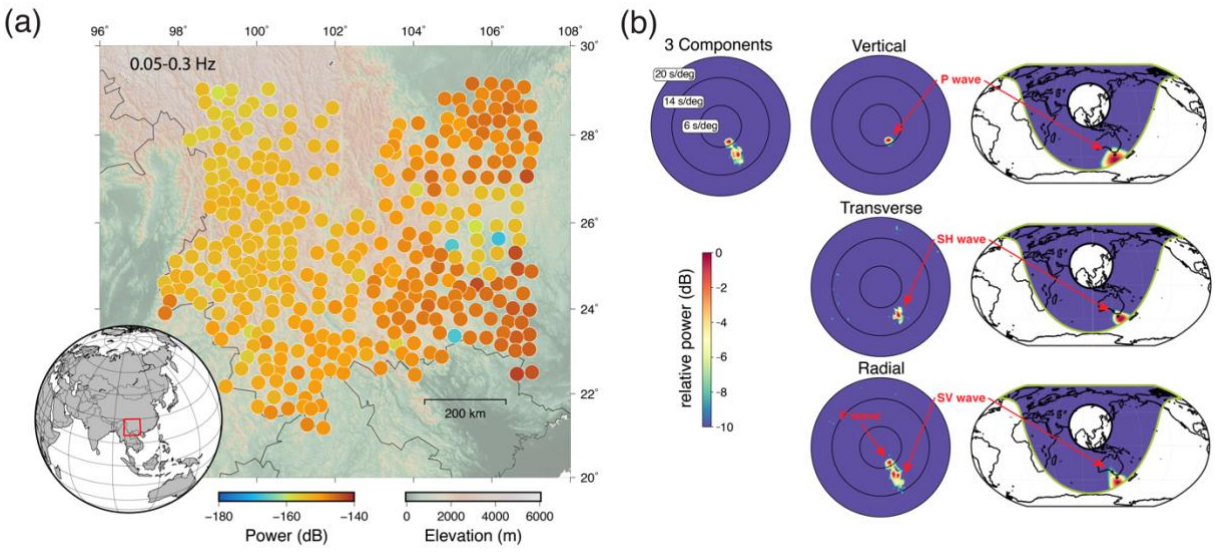

Figure 3.1. (a) The geographic location of the seismic array in this study. The color indicates one-year averaged power spectral density (PSDs) in the frequency band 0.05-0.30 Hz in 2012. Unit is $10log_{10}(m^2s^{-4}Hz^{-1})$. (b) An example of three-component f-k analysis and back-projection at 0.14 Hz. The results are from one-day records on May 7, 2012. We found that both P- and S-wave are from the similar source regions.

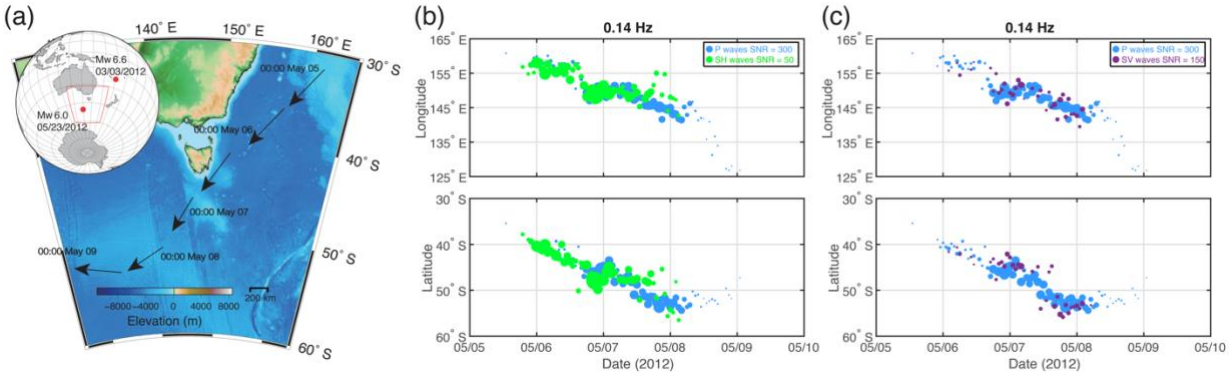

Figure 3.2. Tracking a distant storm in Southeast Australia from May 5 to May 10, 2012 using hourly beamforming results for P-, SH- and SV-wave. (a) The storm tracks and bathymetry. The black arrows show the track of this storm over time. The red dots represent the two earthquake locations that we used for station correction. (b) Longitude (top) and latitude (bottom) of back-projection sources for P-wave (blue dots) and SH-wave (green dots) as a function of time. The size of those dots shows the seismic wave amplitude by the SNRs. (c) Same with (b) but for the P-wave (blue dots) and SV-wave (purple dots).

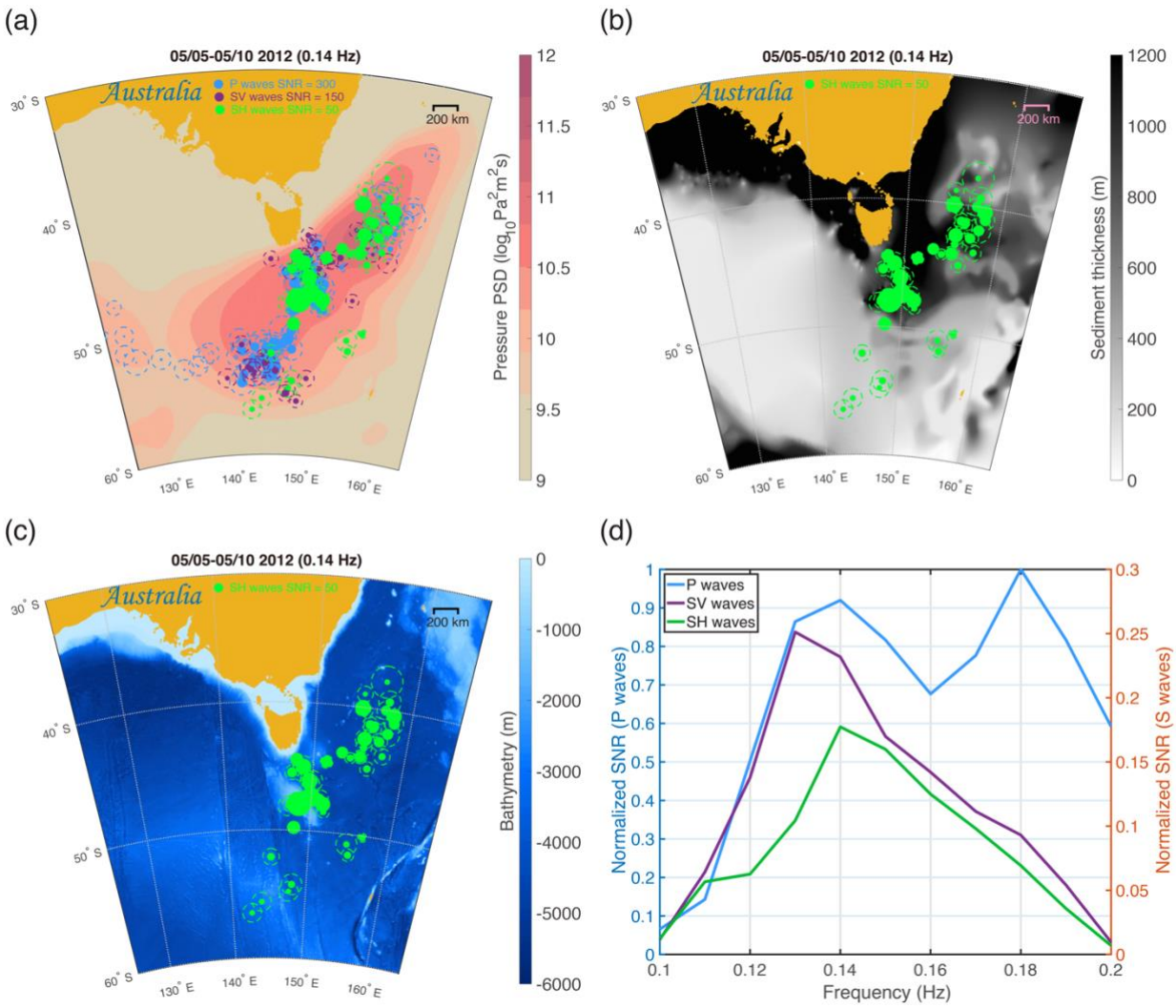

Figure 3.3. (a) Geographic locations of back-projection sources of P-wave (blue dots), SV-wave (purple dots), and SH-wave (green dots) for the storm in Southeast Australia. The size of those dots shows the seismic wave amplitude by SNRs and the dashed circles show the locating uncertainty. The background image shows the 5 days stacked PSD of the ocean wave equivalent pressure between May 5 to May 10, 2012. (b) Same with (a) but the image shows the thickness of the sediments with the sources of SH-wave. (c) Same with (b) but the background is ocean bathymetry. (d) The normalized stacked amplitude of P-wave (blue line), SV-wave (purple line), and SH-wave (green line) waves as a function of frequency from May 5 to May 10, 2012. A full animation for (a) is available in the electronic supplement.

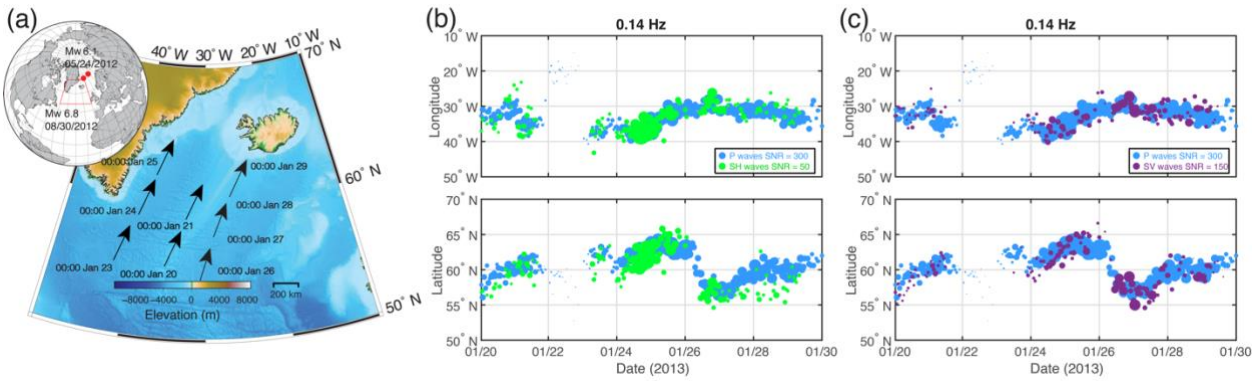

Figure 3.4. Same with Figure 3.2, but for the storms in the North Atlantic near Greenland from January 20 to January 30, 2013.

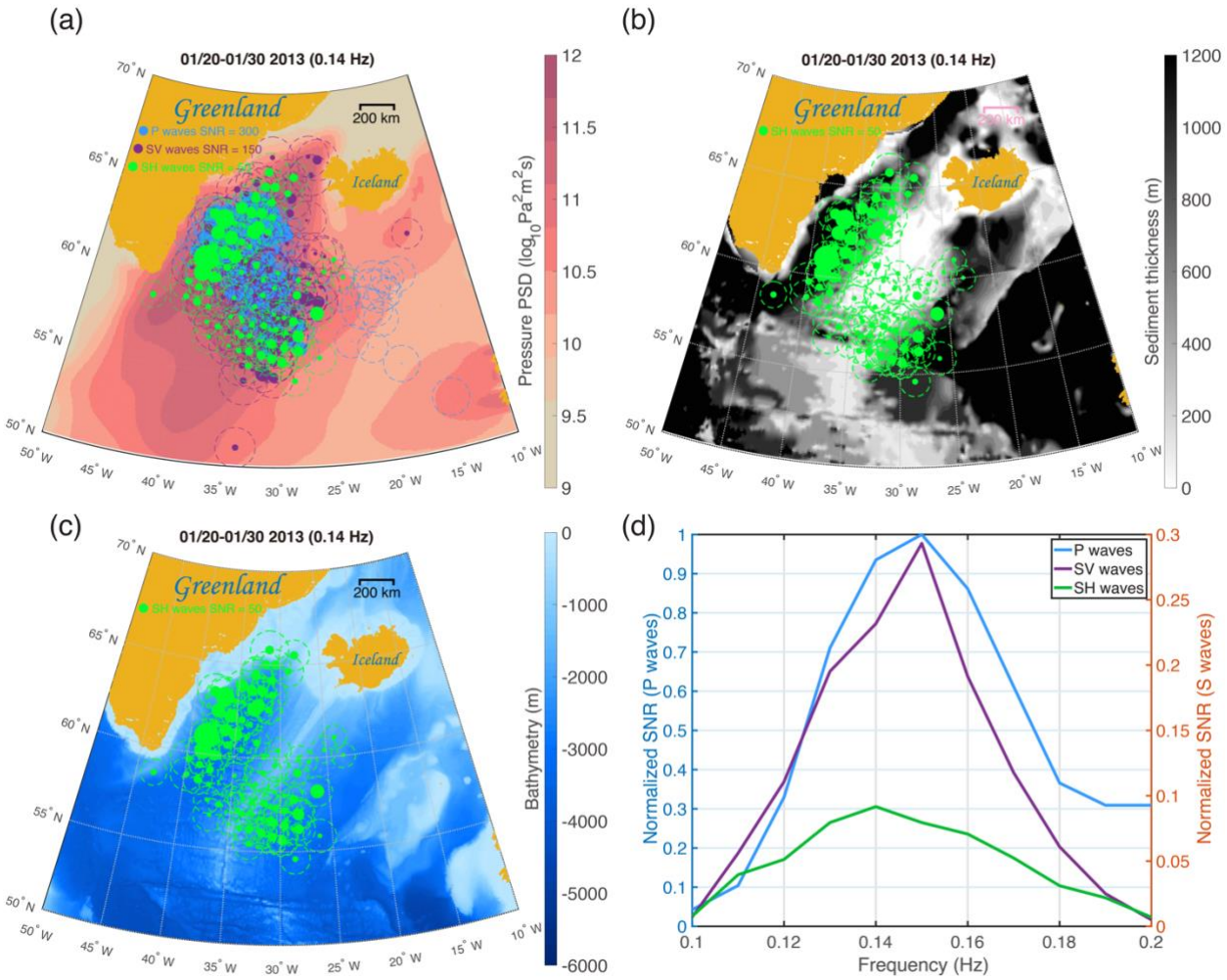

Figure 3.5. Same with Figure 3.3, but for the storms in the North Atlantic near Greenland from January 20 to January 30, 2013.

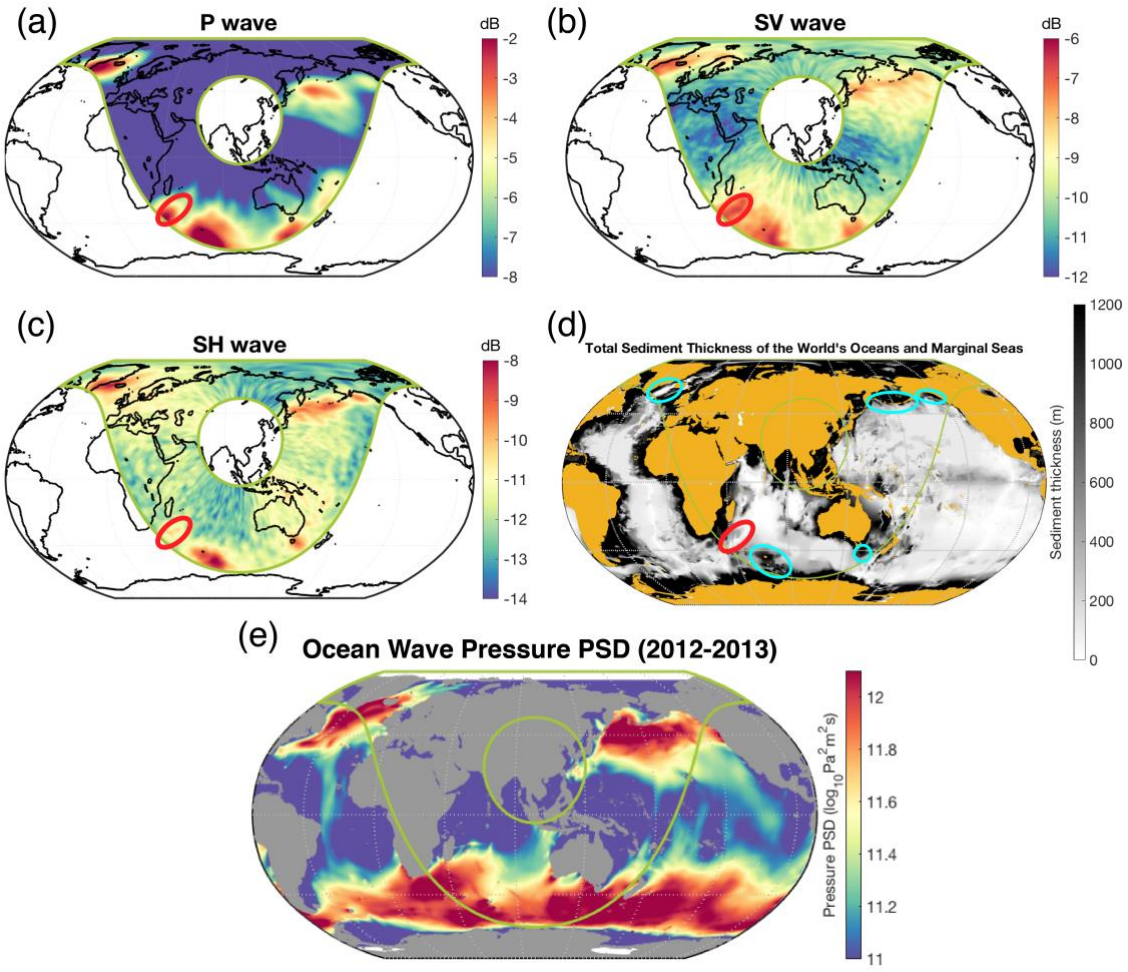

Figure 3.6. (a) The stacked back-projection results in the frequency band 0.11-0.19 Hz from 2011 to 2013 for P waves, (b) SV-wave, and (c) SH-wave. Color scales are different for each type of waves. (d) Total sediment thickness of the world's oceans and marginal sea, the data was downloaded from NOAA (https://www.ngdc.noaa.gov/mgg/sedthick/). The blue circles show the SH-wave source locations with power above -10 dB from beamforming results. (e) The stacked power spectral density of the ocean wave equivalent pressure between 2012 and 2013.

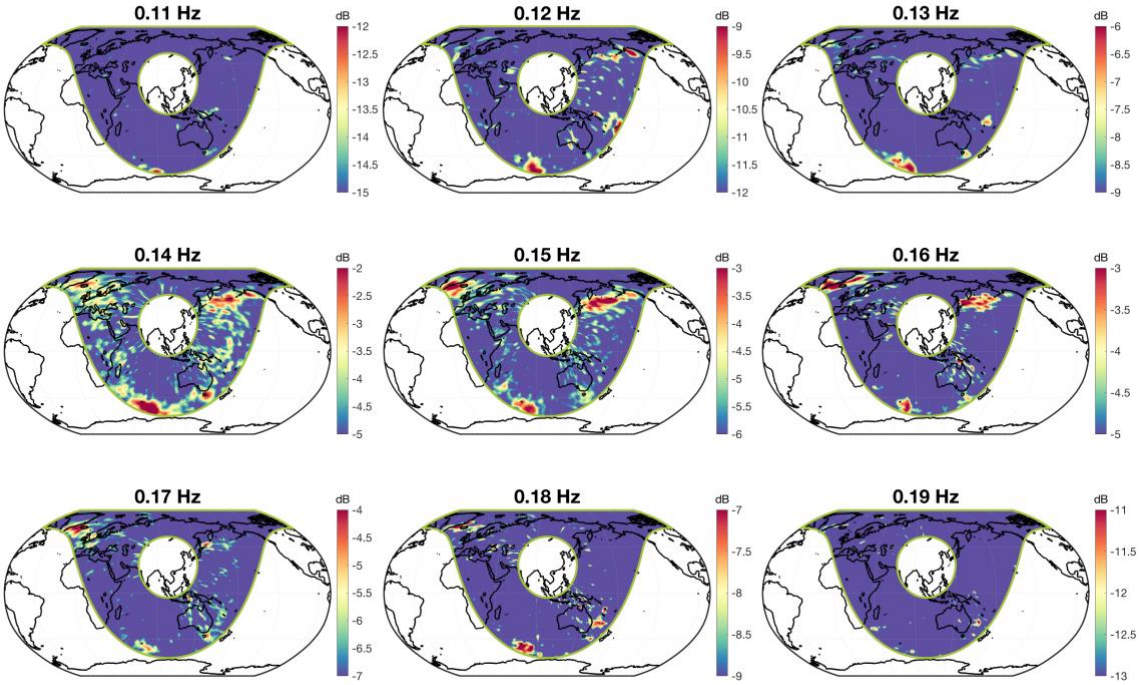

Figure 3.7. The stacked back-projection results of SH-wave from 2012 to 2013 for various frequencies.

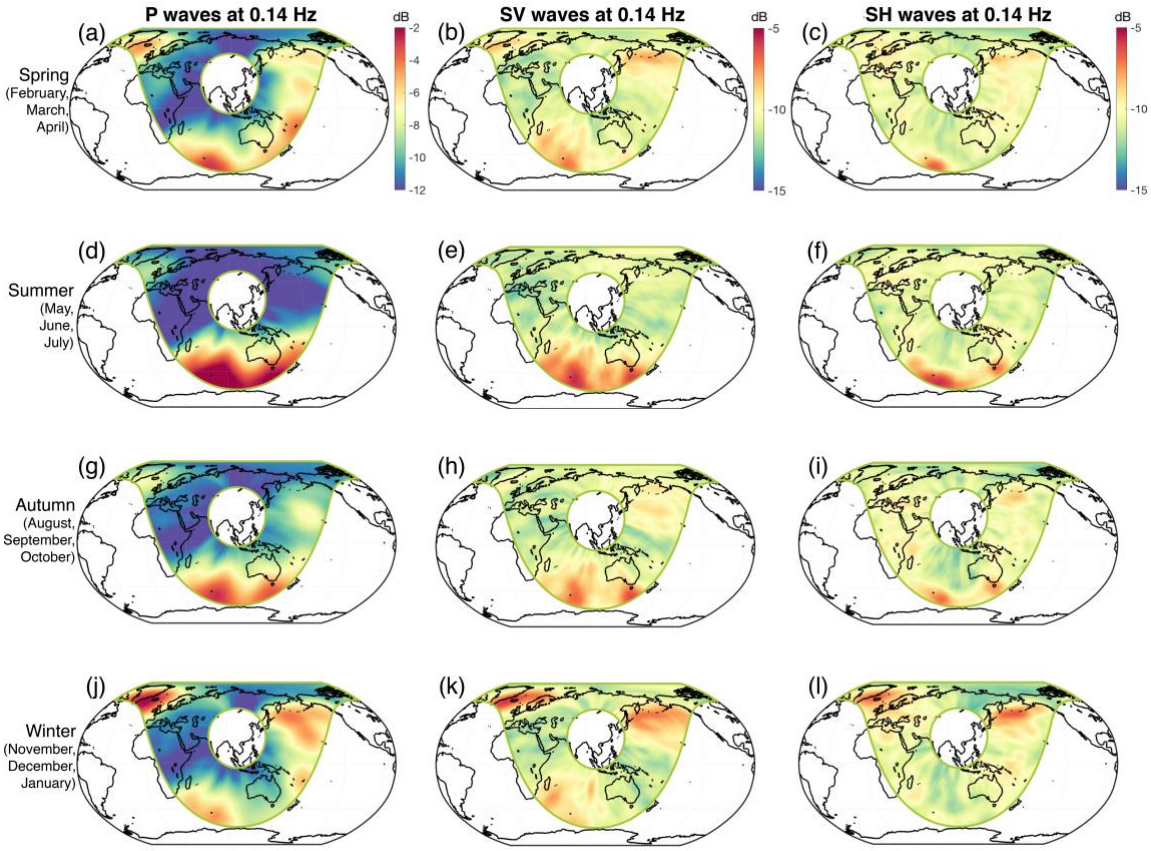

Figure 3.8. Back-projection results for different seasons from 2012 to 2013 at 0.14 Hz. (a) P-wave, (b) SV-wave and (c) SH-wave in spring. Corresponding results for summer are shown in (d-f), autumn in (g-i), and winter in (j-l). Color scales are different for each type of waves but for each type, the scale is the same for four seasons.

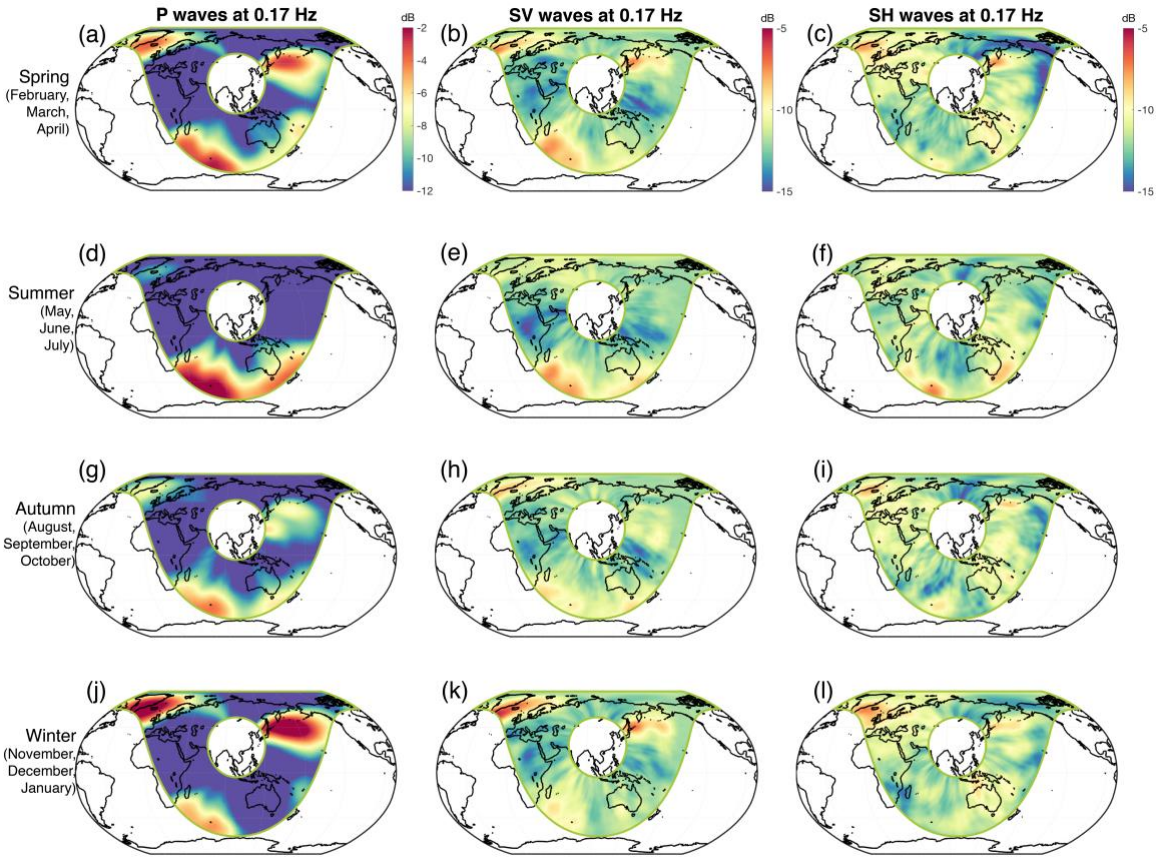

Figure 3.9. Same with Figure 3.8 but at 0.17 Hz.

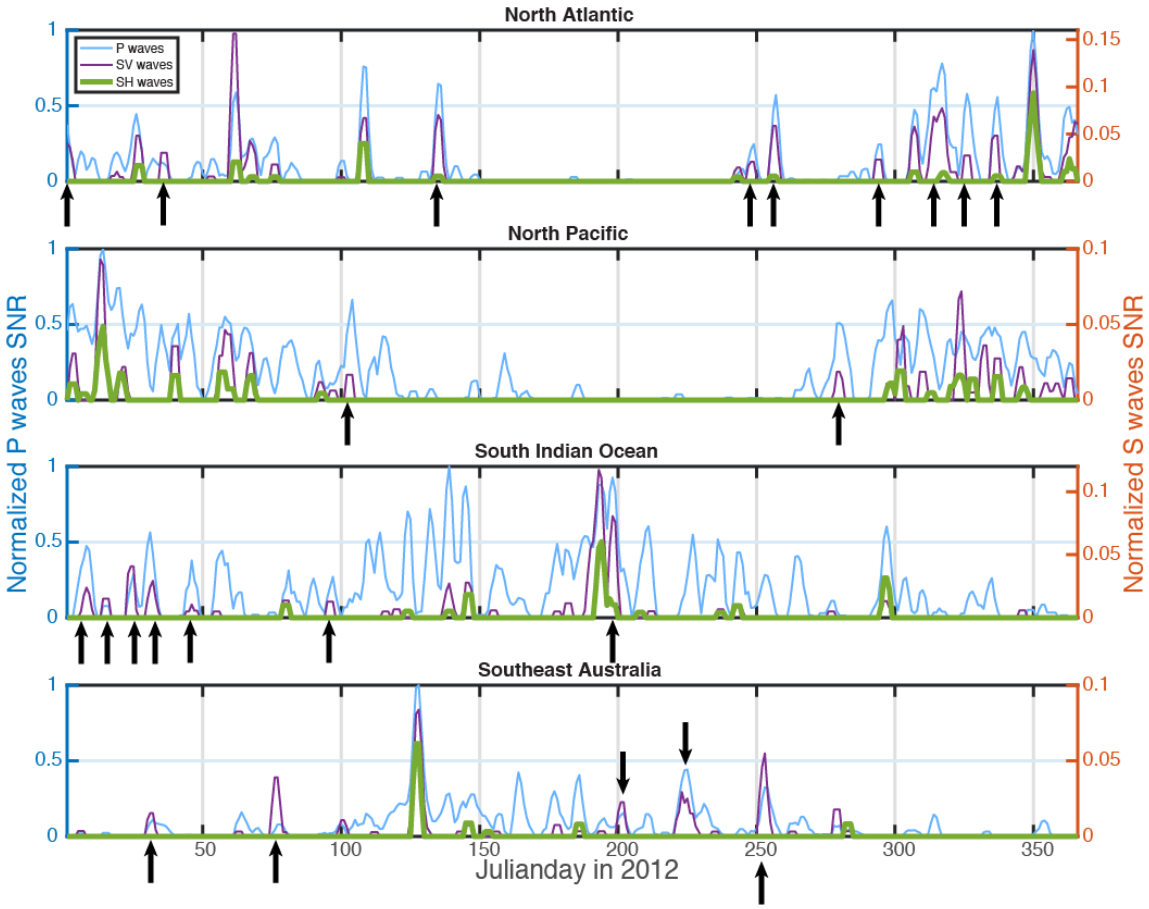

Figure 3.10. The normalized SNR of P-wave (blue line), SV-wave (purple line) and SH-wave (green line) between 0.05 Hz and 0.25 Hz in the North Atlantic, the North Pacific, Including Kerguelen Plateau and the Southeastern Australia as a function of time in 2012. The black arrows highlight the period in absence of SH-wave but have detected SV-wave.

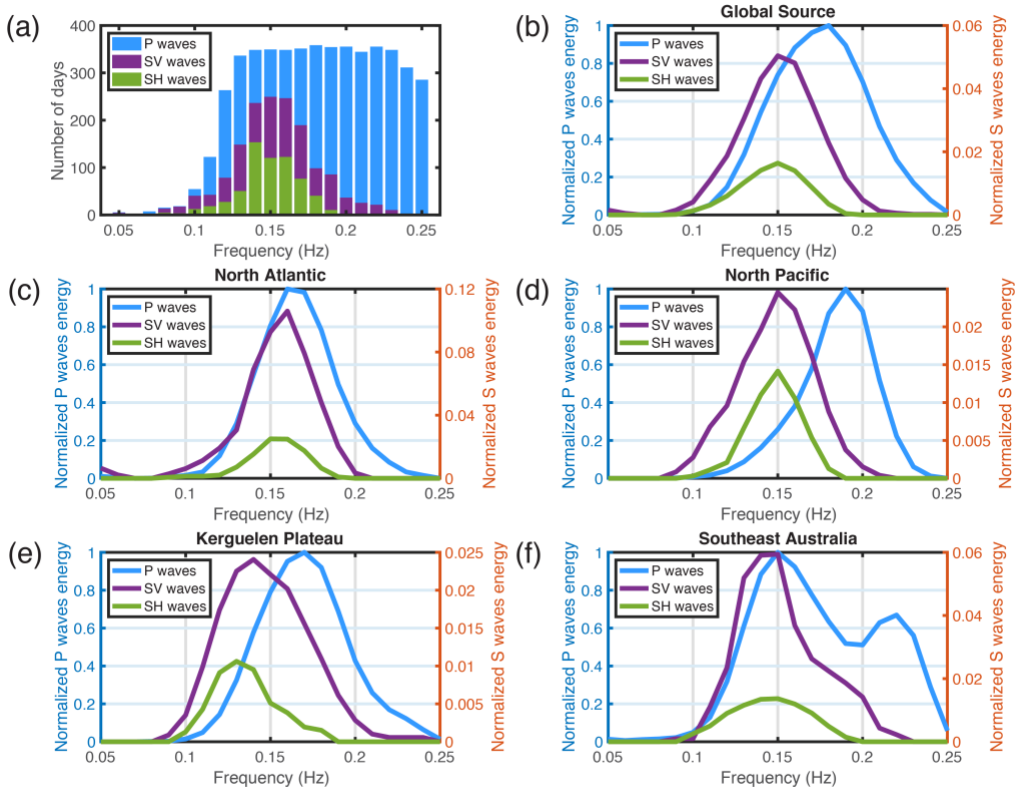

Figure 3.11. (a) The observed number of days for P-wave (blue bars), SV-wave (purple bars), and SH-wave (green bars) from daily-stacked results in 2012 for various frequencies. (b-f) The normalized power distribution of P-wave (blue line), SV-wave (purple line), and SH-wave (green line) for (b) Global stacked source, (c) North Atlantic, (d) North Pacific, (e) Kerguelen Plateau, and (f) Southeastern Australia as a function of frequency.

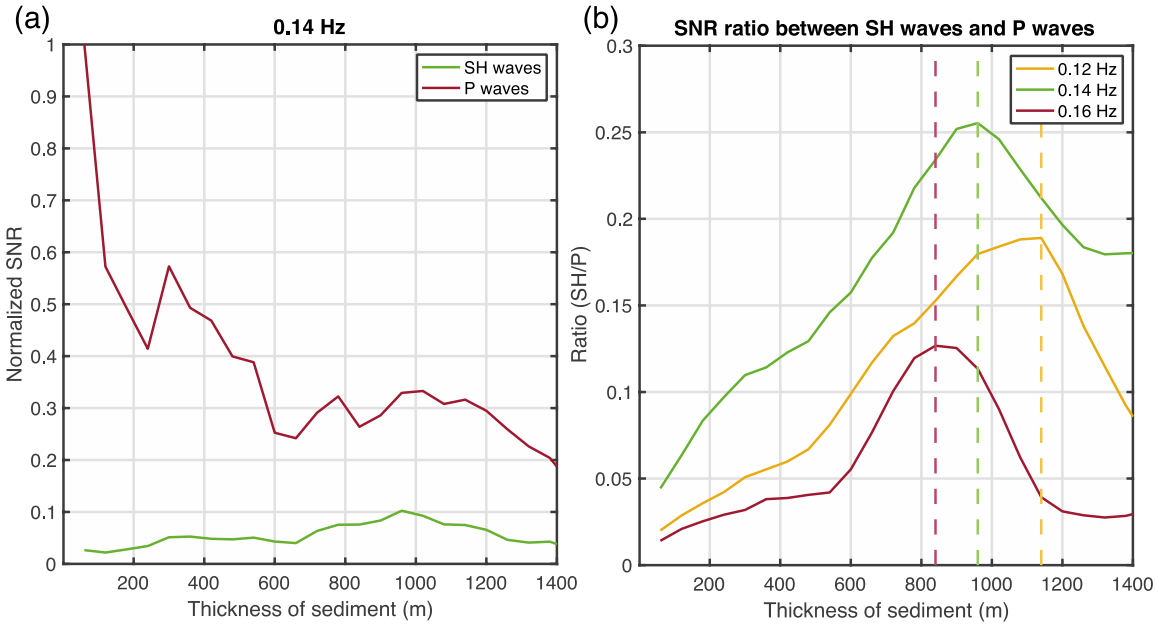

Figure 3.12. The SNR comparisons between P- and SH-wave for the various thicknesses of sediment. (a) The normalized SNR for P- and SH-wave at 0.14 Hz. (b) The SNR ratios between P- and SH-wave at 0.12 Hz, 0.14 Hz and 0.16 Hz.

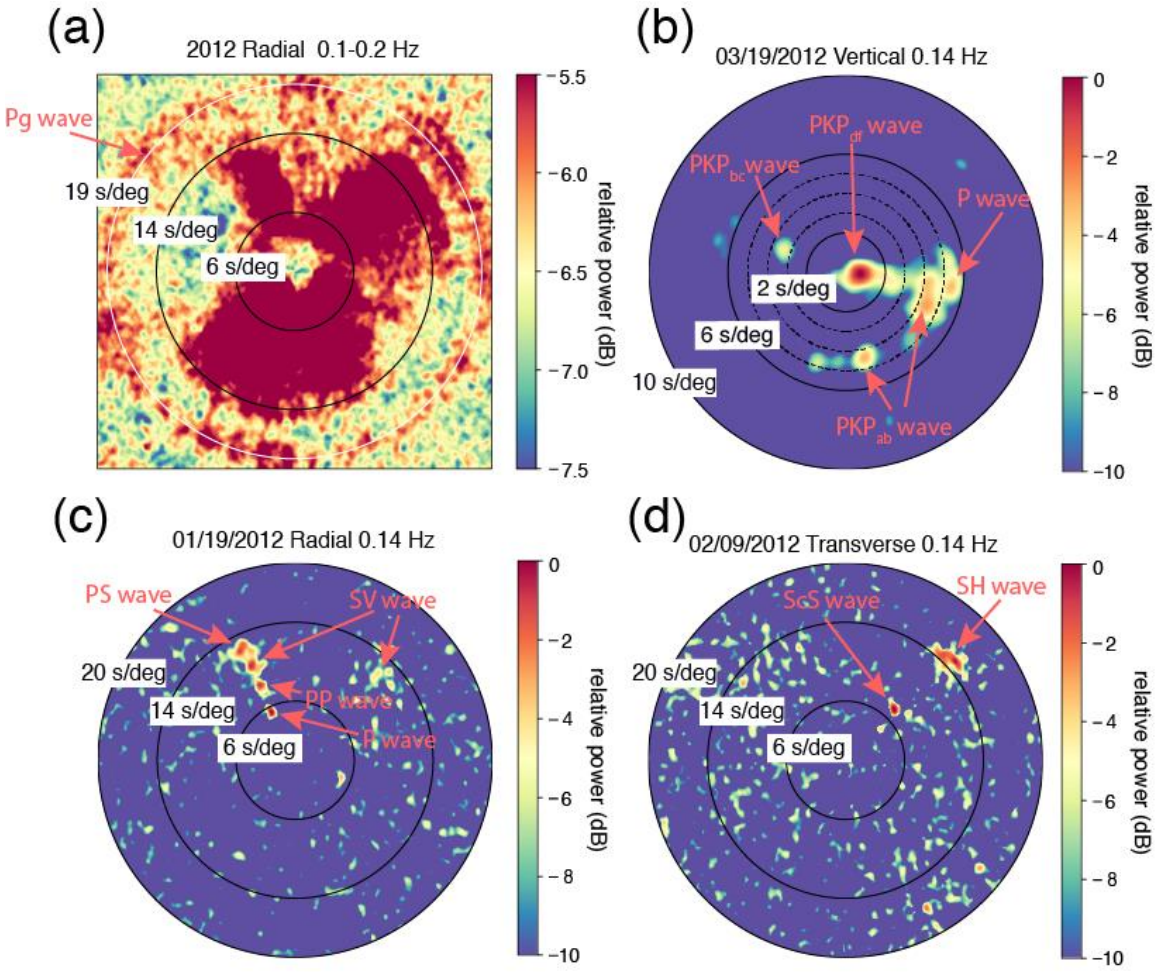

Figure 3.13. (a) One-year stacked radial component results in the frequency band 0.1-0.2 Hz in 2012. Pg-wave are recognized at the slowness of about 19 s/deg. (b) Example of PkPab-, PkPbc-, and PkPdf-wave observed on March 19, 2012. (c) Example of PS-wave in the radial component on January 19, 2012. (d) Example of ScS-wave in the transverse component on February 9, 2012.

3.6 Appendix

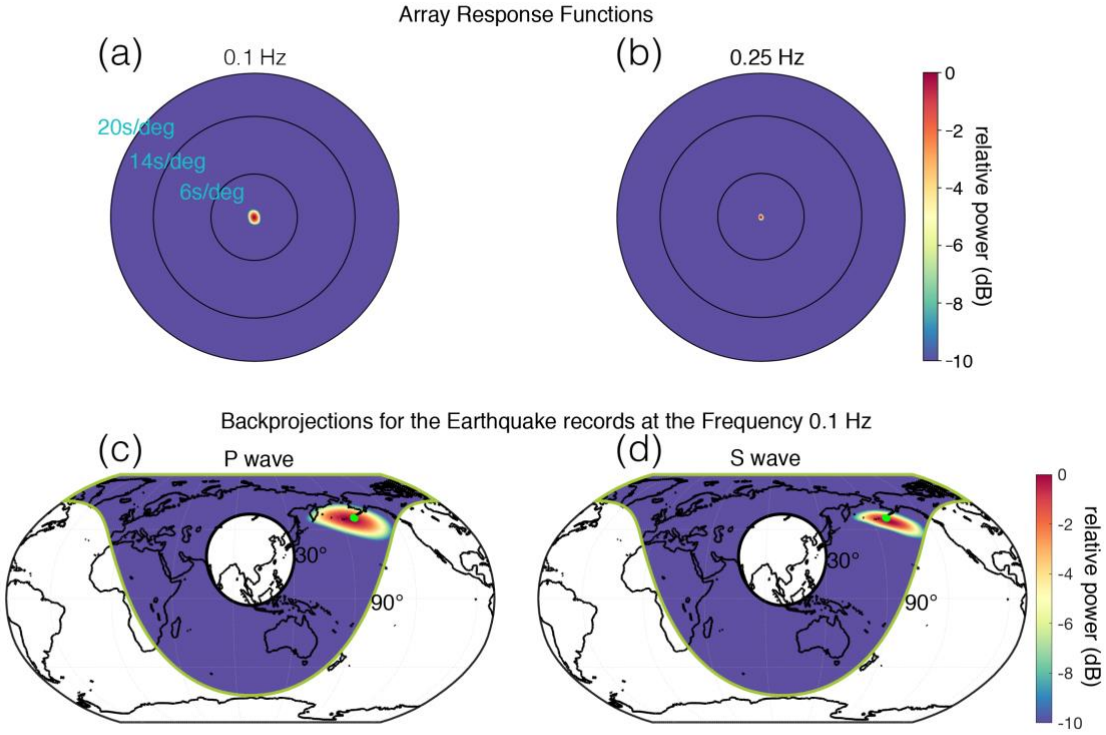

Figure 3.A1. Slowness versus azimuth theoretical array response function at the frequency (a) 0.1 Hz and (b) 0.25 Hz. (c) and (d) show the back-projection results of P and S waves at 0.1 Hz for an M_w 6.2 earthquake (green dot) that occurred on August 10, 2012. The SNR are 109.7, 218.2 and 150.7 for P-, SV- and SH-wave respectively.

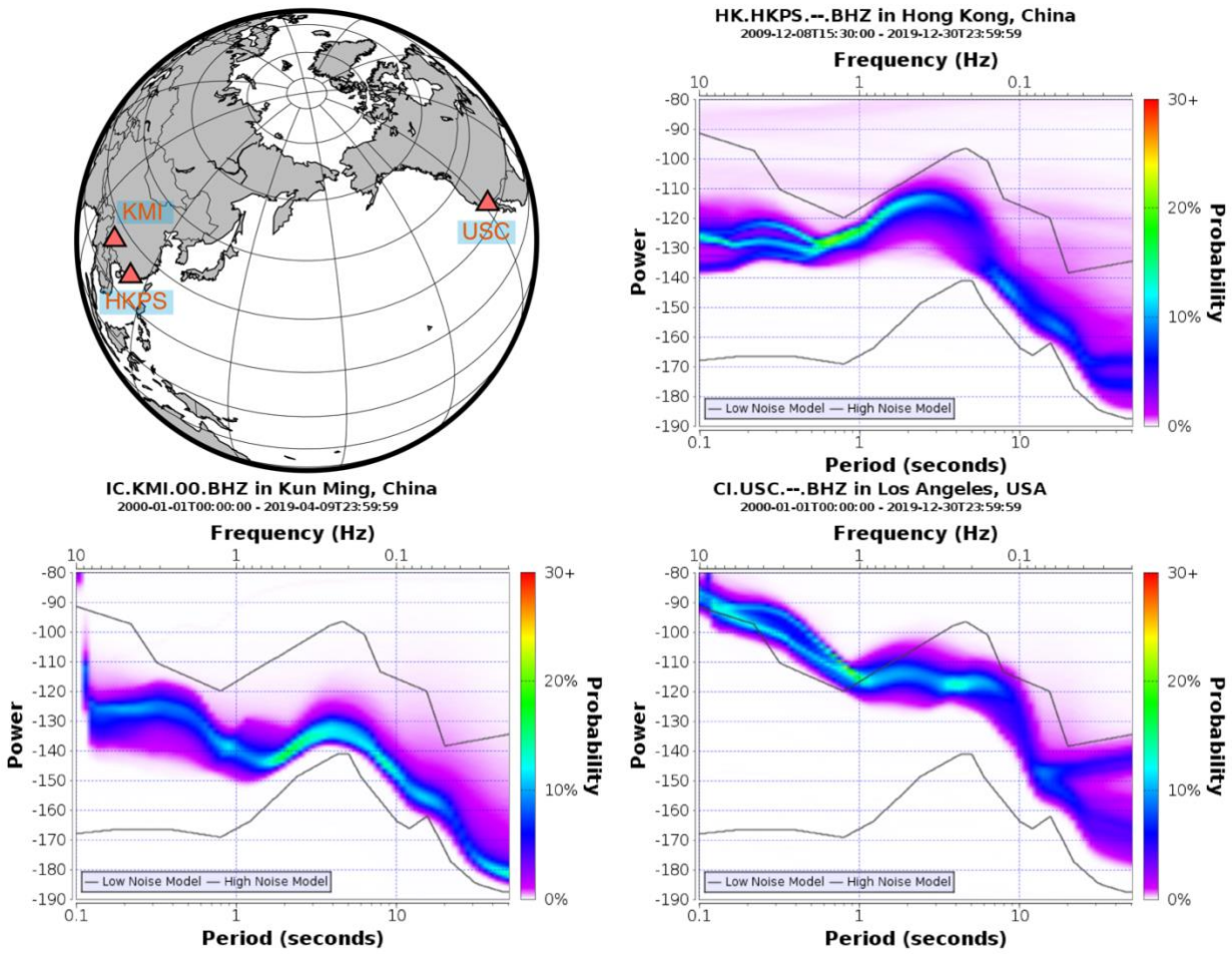

Figure 3.A2. Example power density function (PDF) for the stations IC.KMI in Kunming, China, HK.HKPS in Hong Kong, China, and CI.USC in California, USA.

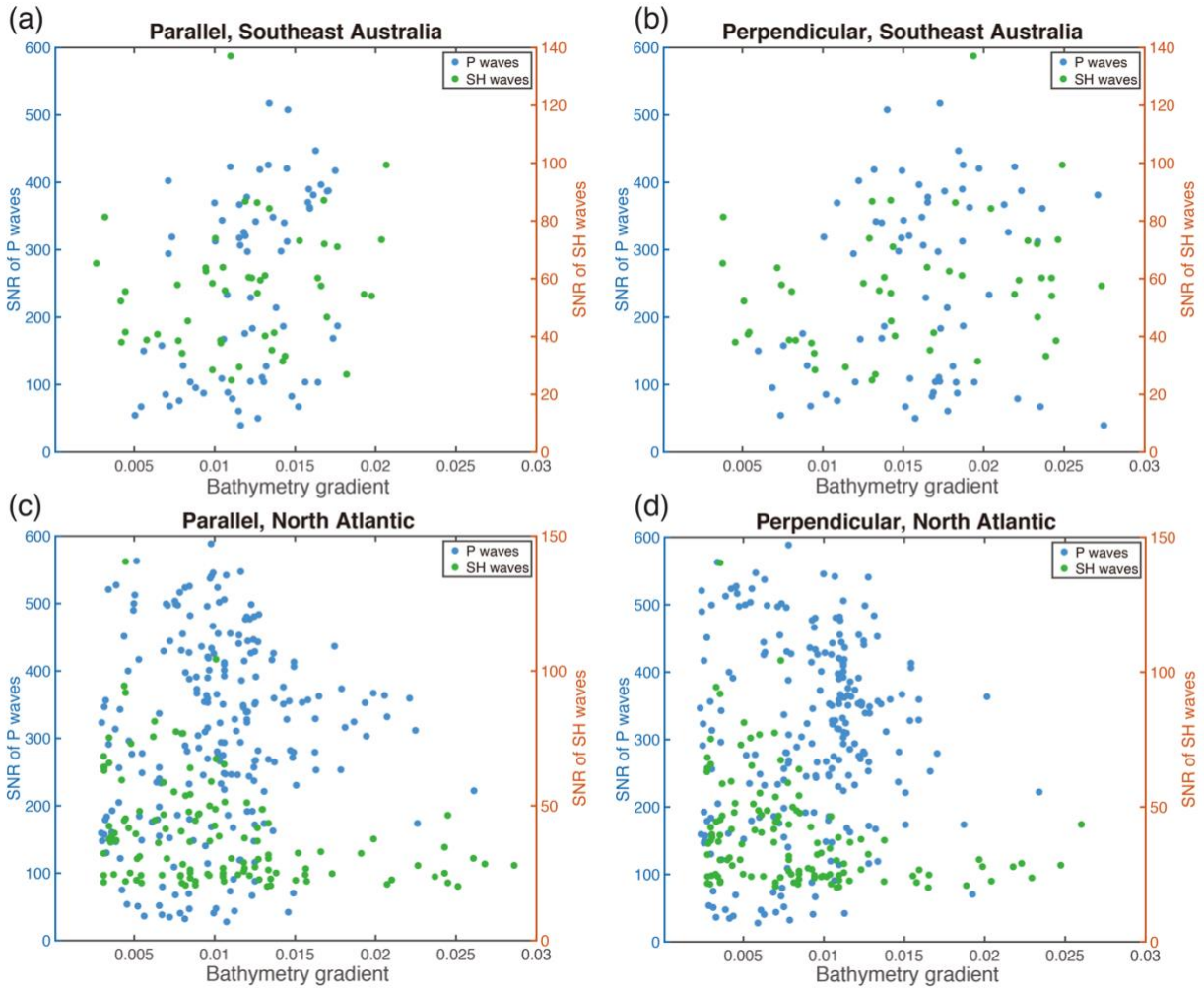

Figure 3.A3. The SNR of P and SH waves as a function of the bathymetry gradient. (a) The direction of the bathymetry gradient parallels the great circle between the array and the seismic sources in Southeast Australia. (b) same with (a) but the direction of the bathymetry gradient is perpendicular to the great circle. (c) same with (a) but for the seismic noise in the North Atlantic. (d) same with (b) but for the seismic noise in the North Atlantic.

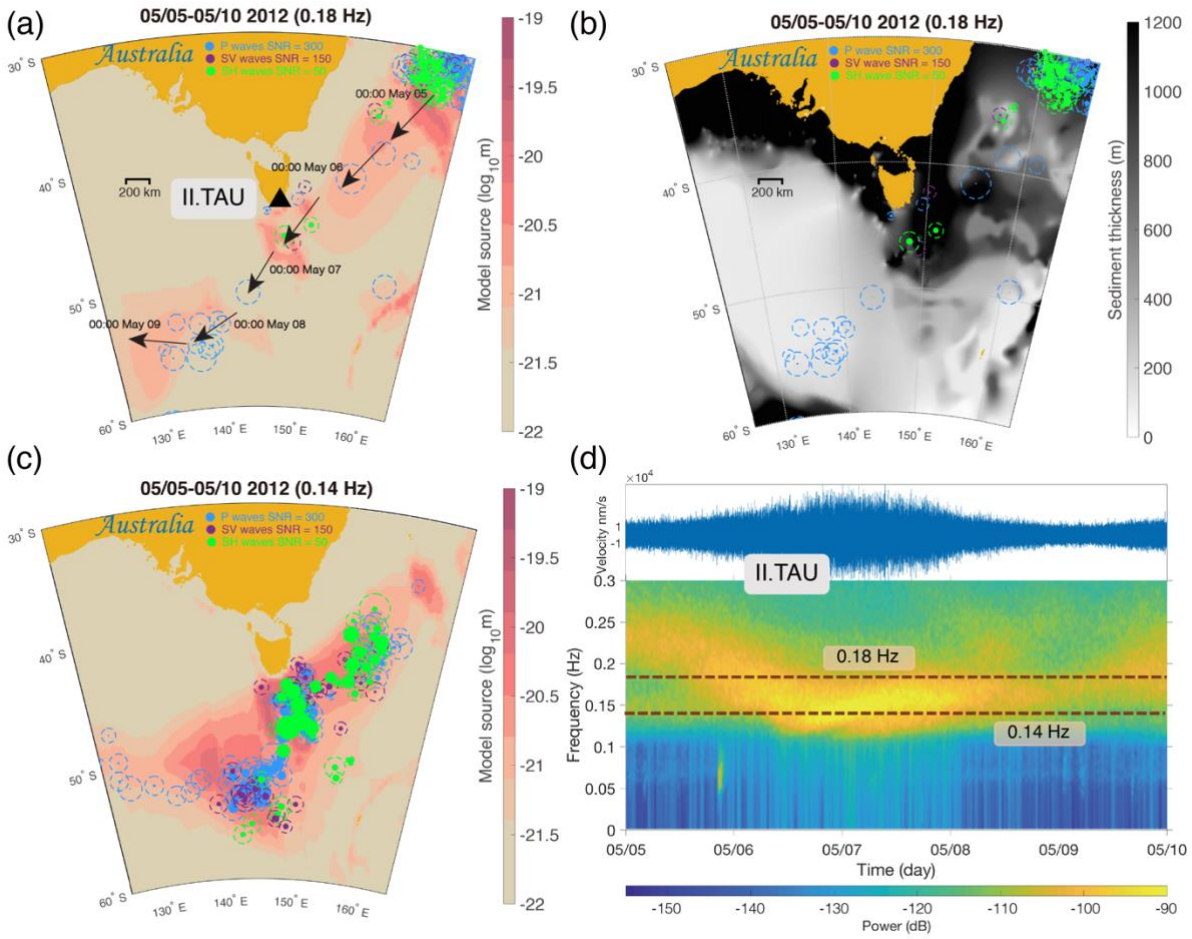

Figure 3.A4. (a) is similar to Figure 3.3a but the background image is the power spectrum of the vertical ground displacement at 0.18 Hz. The black triangle indicates a local seismometer of II.TAU. (b) is similar to Figure 3.3b but at 0.18 Hz. (c) is similar to Figure 3.3a but the background image is the power spectrum of the vertical ground displacement. (d) shows the seismic waveform and spectrum of station II.TAU in Tasmania from May 5 to May 10. We found that on May 5 and early May 6, when the storm was still in eastern Australia, the dominant frequency was around 0.18 Hz. On May 7 and 8, as the storm moved toward southeastern Australia, the dominant frequency changed to 0.14 Hz. Therefore, the spectrum from station II.TAU matches the back projection and modeling results in both time and frequency.

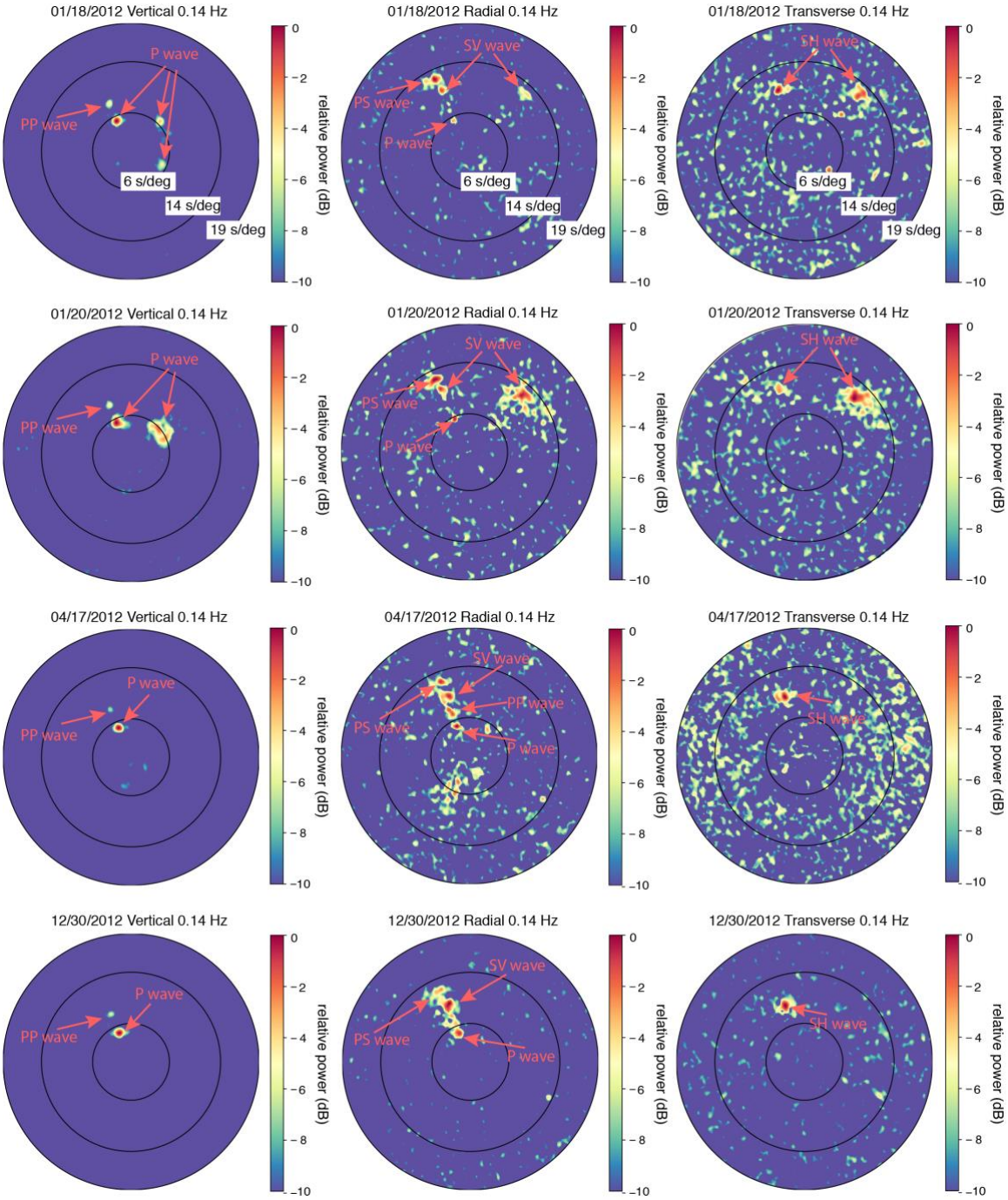

Figure 3.A5. Example of PS-wave that observed at different dates.

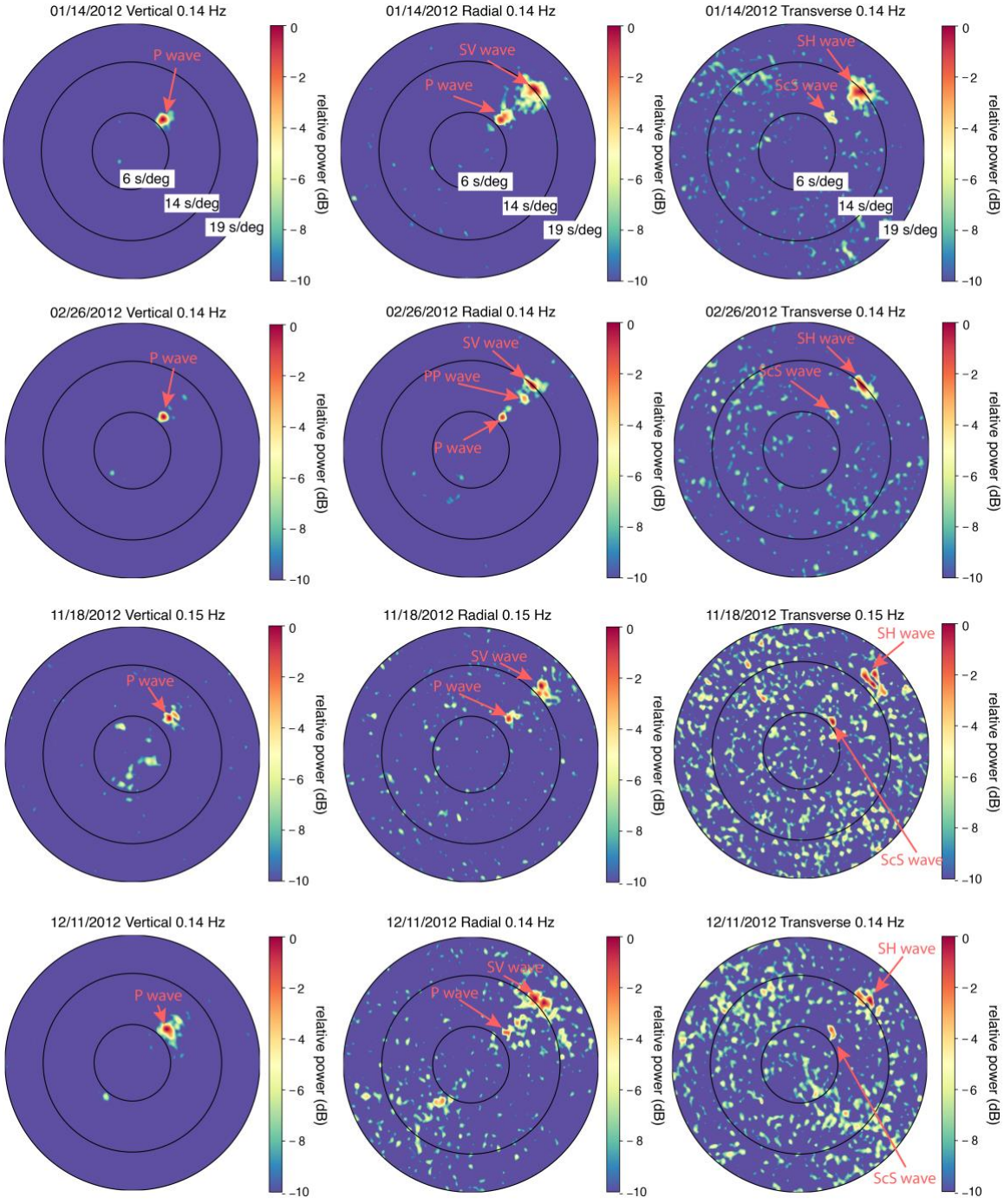

Figure 3.A6. Example of ScS-wave that observed at different dates.

Table 3.A1

Measurements of back-projection for the different earthquakes before stations corrections

Time	Magnitude	Depth	Latitude	Longitude	Latitude inferred from P waves	Longitude inferred from P waves	Signal to noise ratio for P waves	Misfit	Latitude inferred from SH waves	Longitude inferred from SH waves	Misfit	Signal to noise ratio for SH waves
2012-03-03	Mw 6.6	14 km	22.141° S	170.340° E	21.20° S	173.00°E	295.35	291.79 km	18.80°S	171.20°E	381.07 km	139.5
2012-04-14	Mw 6.2	11 km	18.972° S	168.741° E	15.60° S	169.80°E	276.88	391.41 km	14.80°S	168.40°E	464.80 km	126.8
2012-05-20	Mw 6.0	6.3 km	44.890° N	11.230°E	46.60° N	10.40°E	50.3	200.85 km	46.20°N	14.60°E	299.85 km	76.2
2012-05-23	Mw 6.0	10 km	50.420° S	139.516° E	50.40° S	146.00°E	135.3	459.06 km	52.20°N	143.40°E	334.46 km	229.3
2012-05-24	Mw 6.1	10 km	72.960° N	5.683°E	76.40° N	12.40°E	51.4	458.05 km	76.40°N	13.60°W	475.24 km	56.0
2012-08-30	Mw 6.8	14 km	71.441° N	10.605°W	73.20° N	13.00°W	216.0	211.66 km	74.40°N	19.80°W	444.55 km	121.9
2013-01-05	Mw 7.5	8.7 km	55.228° N	134.859° W	54.00° N	138.80°W	215.2	288.33 km	53.80°N	135.40°W	162.34 km	151.6
2013-07-21	Mw 6.5	17 km	41.704° S	174.337° E	38.80° S	170.80°E	159.2	441.02 km	40.20°S	173.60°E	178.43 km	179.2
2013-08-17	Mw 6.2	10 km	34.885° S	54.093°E	34.60° S	49.80°E	152.9	393.22 km	33.20°S	49.60°E	449.23 km	119.1
2013-08-30	Mw 7.0	29.0 km	51.537° N	175.230° W	49.00° N	178.80°W	127.6	378.11 km	51.80°N	179.60°W	295.89 km	71.1

Table 3.A2

Measurements of back-projection after stations corrections in the Southeast Australia

Time	Magnitude	Depth	Latitude	Longitude	Latitude inferred from P waves	Longitude inferred from P waves	Signal to noise ratio for P waves	Misfit	Latitude inferred from SH waves	Longitude inferred from SH waves	Misfit	Signal to noise ratio for SH waves
2012-05-23	Mw 5.9	6.6 km	50.352° S	139.536° E	51.2°S	140.2°E	110.0	105.03 km	49.20°S	139.6°E	127.9 km	80.5
2012-10-09	Mw 6.6	10.0 km	60.326° S	153.699° E	59.2°S	153.8°E	155.6	125.1 km	59.60°S	151.8°E	132.75 km	73.5

Table 3.A3												
Measurements of back-projection after stations corrections in the North Atlantic												
Time	Magnitude	Depth	Latitude	Longitude	Latitude inferred from P waves	Longitude inferred from P waves	Signal to noise ratio for P waves	Misfit	Latitude inferred from SH waves	Longitude inferred from SH waves	Misfit	Signal to noise ratio for SH waves
2012-10-21	Mw 5.5	10.0 km	66.309° N	18.666°W	67.2°N	19.0°W	85.2	100.1 km	65.2°N	18.0°W	129.3 km	76.2
2013-01-20	Mw 5.5	10.0 km	53.873° N	15.127°W	52.8°N	14.8°W	72.5	121.1 km	52.8 °N	15.8°W	127.18 km	65.8

3.7 References

Ardhuin, F., Gualtieri, L., & Stutzmann, E. (2015). How ocean waves rock the Earth: Two mechanisms explain microseisms with periods 3 to 300 s. *Geophysical research letters, 42*(3), 765-772. https://doi.org/10.1002/2014GL062782

Ardhuin, F., & Herbers, T. H. C. (2013). Noise generation in the solid Earth, oceans and atmosphere, from nonlinear interacting surface gravity waves in finite depth. *Journal of Fluid Mechanics, 716*, 316-348. https://doi.org/10.1017/jfm.2012.548

Ardhuin, F., & Roland, A. (2012). Coastal wave reflection, directional spread, and seismoacoustic noise sources. *Journal of Geophysical Research: Oceans, 117*(C11). https://doi.org/10.1029/2011JC007832

Ardhuin, F., Stutzmann, E., Schimmel, M., & Mangeney, A. (2011). Ocean wave sources of seismic noise. *Journal of Geophysical Research, 116*(C9). https://doi.org/10.1029/2011JC006952

Bednar, J., & Watt, T. (1984). Alpha-trimmed means and their relationship to median filters. *IEEE Transactions on acoustics, speech, and signal processing, 32*(1), 145-153. https://doi.org/10.1109/TASSP.1984.1164279

Behr, Y., Townend, J., Bowen, M., Carter, L., Gorman, R., Brooks, L., & Bannister, S. (2013). Source directionality of ambient seismic noise inferred from three-component beamforming. *Journal of Geophysical Research: Solid Earth, 118*(1), 240-248. https://doi.org/10.1029/2012JB009382

Bensen, G., Ritzwoller, M., Barmin, M., Levshin, A., Lin, F., Moschetti, M., et al. (2007). Processing seismic ambient noise data to obtain reliable broad-band surface wave

dispersion measurements. *Geophysical Journal International, 169*(3), 1239-1260. https://doi.org/10.1111/j.1365-246X.2007.03374.x

Bormann, P. (2012). *New Manual of Seismological Observatory Practice (NMSOP-2)*. Potsdam: IASPEI, GFZ German Research Centre for Geosciences. https://doi.org/10.2312/GFZ.NMSOP-2

Campillo, M., & Paul, A. (2003). Long-range correlations in the diffuse seismic coda. *Science, 299*(5606), 547-549. https://doi.org/10.1126/science.1078551

Capon, J. (1969). High-resolution frequency-wavenumber spectrum analysis. *Proceedings of the IEEE, 57*(8), 1408-1418. https://doi.org/10.1109/PROC.1969.7278

ChinArray. (2006). China Seismic Array waveform data. *China Earthquake Administration*.

Euler, G. G., Wiens, D. A., & Nyblade, A. A. (2014). Evidence for bathymetric control on the distribution of body wave microseism sources from temporary seismic arrays in Africa. *Geophysical Journal International, 197*(3), 1869-1883. https://doi.org/10.1093/gji/ggu105

Farra, V., Stutzmann, E., Gualtieri, L., Schimmel, M., & Ardhuin, F. (2016). Ray-theoretical modeling of secondary microseism P waves. *Geophysical Journal International, 206*(3), 1730-1739. https://doi.org/10.1093/gji/ggw242

Gal, M., Reading, A., Ellingsen, S., Koper, K., & Burlacu, R. (2017). Full wavefield decomposition of high‐frequency secondary microseisms reveals distinct arrival azimuths for Rayleigh and Love waves. *Journal of Geophysical Research: Solid Earth, 122*(6), 4660-4675. https://doi.org/10.1002/2017JB014141

Gal, M., A. M. Reading, S. Ellingsen, L. Gualtieri, K. Koper, R. Burlacu, H. Tkalčić and M. Hemer (2015). The Frequency Dependence and Locations of Short‐Period

Microseisms Generated in the Southern Ocean and West Pacific, *Journal of Geophysical Research: Solid Earth* **120,** no. 8, 5764-5781, doi: https://doi.org/10.1002/2015JB012210.

Gerstoft, P., Shearer, P. M., Harmon, N., & Zhang, J. (2008). Global P, PP, and PKP wave microseisms observed from distant storms. *Geophysical research letters*, *35*(23). https://doi.org/10.1029/2008GL036111

Gualtieri, L., Bachmann, E., Simons, F. J., & Tromp, J. (2020). The origin of secondary microseism Love waves. *Proceedings of the National Academy of Sciences*, *117*(47), 29504-29511. https://doi.org/10.1073/pnas.2013806117

Gualtieri, L., Bachmann, E., Simons, F. J., & Tromp, J. (2021). Generation of secondary microseism Love waves: effects of bathymetry, 3-D structure and source seasonality. *Geophysical Journal International*, *226*(1), 192-219. https://doi.org/10.1093/gji/ggab095

Gualtieri, L., Stutzmann, É., Farra, V., Capdeville, Y., Schimmel, M., Ardhuin, F., & Morelli, A. (2014). Modelling the ocean site effect on seismic noise body waves. *Geophysical Journal International*, *197*(2), 1096-1106. https://doi.org/10.1093/gji/ggu042

Guo, Z., Xue, M., Aydin, A., & Ma, Z. (2020). Exploring source regions of single-and double-frequency microseisms recorded in eastern North American margin (ENAM) by cross-correlation. *Geophysical Journal International*, *220*(2), 1352-1367. https://doi.org/10.1093/gji/ggz470

Hasselmann, K. (1963). A statistical analysis of the generation of microseisms. *Reviews of Geophysics*, *1*(2), 177-210. https://doi.org/10.1029/RG001i002p00177

Hillers, G., Graham, N., Campillo, M., Kedar, S., Landès, M., & Shapiro, N. (2012). Global oceanic microseism sources as seen by seismic arrays and predicted by wave action models. *Geochemistry, Geophysics, Geosystems, 13*(1). https://agupubs.onlinelibrary.wiley.com/doi/abs/10.1029/2011GC003875

Juretzek, C., & Hadziioannou, C. (2016). Where do ocean microseisms come from? A study of Love-to-Rayleigh wave ratios. *Journal of Geophysical Research: Solid Earth, 121*(9), 6741-6756. https://doi.org/10.1002/2016JB013017

Kedar, S., Longuet-Higgins, M., Webb, F., Graham, N., Clayton, R., & Jones, C. (2008). The origin of deep ocean microseisms in the North Atlantic Ocean. *Proceedings of the Royal Society A: Mathematical, Physical and Engineering Sciences, 464*(2091), 777-793. https://doi.org/10.1098/rspa.2007.0277

Kennett, B. L., Engdahl, E., & Buland, R. (1995). Constraints on seismic velocities in the Earth from traveltimes. *Geophysical Journal International, 122*(1), 108-124. https://doi.org/10.1111/j.1365-246X.1995.tb03540.x

Koper, K. D., & Burlacu, R. (2015). The fine structure of double‐frequency microseisms recorded by seismometers in North America. *Journal of Geophysical Research: Solid Earth, 120*(3), 1677-1691. https://doi.org/10.1002/2014JB011820

Koper, K. D., de Foy, B., & Benz, H. (2009). Composition and variation of noise recorded at the Yellowknife Seismic Array, 1991–2007. *Journal of Geophysical Research: Solid Earth, 114*(B10). https://doi.org/10.1029/2009JB006307

Koper, K. D., Seats, K., & Benz, H. (2010). On the composition of Earth's short-period seismic noise field. *Bulletin of the Seismological Society of America, 100*(2), 606-617. https://doi.org/10.1785/0120090120

Landès, M., Hubans, F., Shapiro, N. M., Paul, A., & Campillo, M. (2010). Origin of deep ocean microseisms by using teleseismic body waves. *Journal of Geophysical Research: Solid Earth*, *115*(B5). https://doi.org/10.1029/2009JB006918

Le Pape, F., Craig, D., & Bean, C. J. (2021). How deep ocean-land coupling controls the generation of secondary microseism Love waves. *Nature Communications*, *12*(1), 2332. https://doi.org/10.1038/s41467-021-22591-5

Liu, Q., Koper, K. D., Burlacu, R., Ni, S., Wang, F., Zou, C., et al. (2016). Source locations of teleseismic P, SV, and SH waves observed in microseisms recorded by a large aperture seismic array in China. *Earth and Planetary Science Letters*, *449*, 39-47. https://doi.org/10.1016/j.epsl.2016.05.035

Longuet-Higgins, M. S. (1950). A Theory of the Origin of Microseisms. *Philosophical Transactions of the Royal Society of London A-Mathematical and Physical Sciences*, *243*(857), 1-35. https://doi.org/10.1098/rsta.1950.0012

McNamara, D. E., & Buland, R. P. (2004). Ambient noise levels in the continental United States. *Bulletin of the Seismological Society of America*, *94*(4), 1517-1527. https://doi.org/10.1785/012003001

Meschede, M., Stutzmann, É., Farra, V., Schimmel, M., & Ardhuin, F. (2017). The Effect of Water Column Resonance on the Spectra of Secondary Microseism P Waves. *Journal of Geophysical Research: Solid Earth*, *122*(10), 8121-8142. https://doi.org/10.1002/2017JB014014

Neale, J., Harmon, N., & Srokosz, M. (2017). Monitoring remote ocean waves using P-wave microseisms. *Journal of Geophysical Research: Oceans*, *122*(1), 470-483. https://doi.org/10.1002/2016JC012183

Nishida, K., Kawakatsu, H., Fukao, Y., & Obara, K. (2008). Background Love and Rayleigh waves simultaneously generated at the Pacific Ocean floors. *Geophysical research letters, 35*(16). https://doi.org/10.1029/2008GL034753

Nishida, K., & Takagi, R. (2016). Teleseismic S wave microseisms. *Science, 353*(6302), 919-921. https://doi.org/10.1126/science.aaf7573

Oten, R., & Figueiredo, R. J. P. d. (2004). Adaptive alpha-trimmed mean filters under deviations from assumed noise model. *IEEE Transactions on Image Processing, 13*(5), 627-639. http://doi.org/10.1109/TIP.2003.821115

Peterson, J. R. (1993). Observations and modeling of seismic background noise. *U.S. Geological SurveyS Open‐File Report*, 93–322 (pp. 394). https://doi.org/10.3133/ofr93322

Pyle, M. L., Koper, K. D., Euler, G. G., & Burlacu, R. (2015). Location of high‐frequency P wave microseismic noise in the Pacific Ocean using multiple small aperture arrays. *Geophysical Research Letters, 42*(8), 2700-2708. https://doi.org/10.1002/2015GL063530

Reading, A. M., Koper, K. D., Gal, M., Graham, L. S., Tkalčić, H., & Hemer, M. A. (2014). Dominant seismic noise sources in the Southern Ocean and West Pacific, 2000–2012, recorded at the Warramunga Seismic Array, Australia. *Geophysical research letters, 41*(10), 3455-3463. https://doi.org/10.1002/2014GL060073

Reif, C., Shearer, P. M., & Astiz, L. (2002). Evaluating the performance of global seismic stations. *Seismological Research Letters, 73*(1), 46-56. https://doi.org/10.1785/gssrl.73.1.46

Retailleau, L., & Gualtieri, L. (2019). Toward High‐Resolution Period‐Dependent Seismic Monitoring of Tropical Cyclones. *Geophysical research letters*, *46*(3), 1329-1337. https://doi.org/10.1029/2018GL080785

Rost, S., & Thomas, C. (2002). Array seismology: Methods and applications. *Reviews of Geophysics*, *40*(3), 1008. https://doi.org/10.1029/2000RG000100

Shapiro, N. M., & Campillo, M. (2004). Emergence of broadband Rayleigh waves from correlations of the ambient seismic noise. *Geophysical research letters*, *31*(7). https://doi.org/10.1029/2004GL019491

Shapiro, N. M., Campillo, M., Stehly, L., & Ritzwoller, M. H. (2005). High-resolution surface-wave tomography from ambient seismic noise. *Science*, *307*(5715), 1615-1618. http://doi.org/10.1126/science.1108339

Straume, E. O., Gaina, C., Medvedev, S., Hochmuth, K., Gohl, K., Whittaker, J. M., et al. (2019). GlobSed: Updated Total Sediment Thickness in the World's Oceans. *Geochemistry, Geophysics, Geosystems*, *20*(4), 1756-1772. https://doi.org/10.1029/2018GC008115

Stutzmann, E., Ardhuin, F., Schimmel, M., Mangeney, A., & Patau, G. (2012). Modelling long-term seismic noise in various environments. *Geophysical Journal International*, *191*(2), 707-722. https://doi.org/10.1111/j.1365-246X.2012.05638.x

Stutzmann, E., Roult, G., & Astiz, L. (2000). GEOSCOPE station noise levels. *Bulletin of the Seismological Society of America*, *90*(3), 690-701. https://doi.org/10.1785/0119990025

Tanimoto, T. (2007a). Excitation of microseisms. *Geophysical Research Letters*, *34*(5). https://doi.org/10.1029/2006GL029046

Tanimoto, T. (2007b). Excitation of normal modes by non-linear interaction of ocean waves. *Geophysical Journal International, 168*(2), 571-582. https://doi.org/10.1111/j.1365-246X.2006.03240.x

Tanimoto, T., Hadziioannou, C., Igel, H., Wasserman, J., Schreiber, U., & Gebauer, A. (2015). Estimate of Rayleigh‐to‐Love wave ratio in the secondary microseism by colocated ring laser and seismograph. *Geophysical research letters, 42*(8), 2650-2655. https://doi.org/10.1002/2015GL063637

Tanimoto, T., Lin, C.-J., Hadziioannou, C., Igel, H., & Vernon, F. (2016). Estimate of Rayleigh-to-Love wave ratio in the secondary microseism by a small array at Piñon Flat observatory, California. *Geophysical research letters, 43*(21), 11,173-111,181. https://doi.org/10.1002/2016GL071133

ToksöZ, M. N., & Lacoss, R. T. (1968). Microseisms: Mode Structure and Sources. *Science, 159*(3817), 872-873. https://doi.org/10.1126/science.159.3817.872

Tolman, H. L. (2009). User manual and system documentation of WAVEWATCH III TM version 3.14. *J Technical note, MMAB Contribution, 276*, 220.

VanDecar, J. C., & Crosson, R. S. (1990). Determination of teleseismic relative phase arrival times using multi-channel cross-correlation and least squares. *Bulletin of the Seismological Society of America, 80*(1), 150-169. https://doi.org/10.1785/BSSA0800010150

Van Der Baan, M. (2009). The Origin of Sh-Wave Resonance Frequencies in Sedimentary Layers, *Geophysical Journal International* **178,** no. 3, 1587-1596. https://doi.org/10.1111/j.1365-246X.2009.04245.x

Vinnik, L. P. (1973). Sources of microseismic P waves. *pure and applied geophysics, 103*(1), 282-289. https://doi.org/10.1007/BF00876404

Wang, W., Gerstoft, P., & Wang, B. (2018). Seasonality of P wave microseisms from NCF-based beamforming using ChinArray. *Geophysical Journal International, 213*(3), 1832-1848. https://doi.org/10.1093/gji/ggy081

Ward Neale, J., Harmon, N., & Srokosz, M. (2018). Improving Microseismic P Wave Source Location With Multiple Seismic Arrays. *Journal of Geophysical Research: Solid Earth, 123*(1), 476-492. https://doi.org/10.1002/2017JB015015

Webb, S. C. (1998). Broadband seismology and noise under the ocean. *J Reviews of Geophysics, 36*(1), 105-142. https://doi.org/10.1029/97RG02287

Wessel, P., & Smith, W. H. (1991). Free software helps map and display data. *Eos, Transactions American Geophysical Union, 72*(41), 441-446. https://doi.org/10.1029/90EO00319

Xiao, H., Xue, M., Yang, T., Liu, C., Hua, Q., Xia, S., et al. (2018). The Characteristics of Microseisms in South China Sea: Results From a Combined Data Set of OBSs, Broadband Land Seismic Stations, and a Global Wave Height Model. *Journal of Geophysical Research: Solid Earth, 123*, 3923–3942. https://doi.org/10.1029/2017JB015291

Zhang, J., Gerstoft, P., & Bromirski, P. D. (2010). Pelagic and coastal sources of P-wave microseisms: Generation under tropical cyclones. *Geophysical Research Letters, 37*(15). https://doi.org/10.1029/2010GL044288

Zhang, J., Gerstoft, P., & Shearer, P. M. (2010). Resolving P-wave travel-time anomalies using seismic array observations of oceanic storms. *Earth and Planetary Science Letters, 292*(3-4), 419-427. https://doi.org/10.1016/j.epsl.2010.02.014

4. Locating the Precise Sources of High-Frequency Microseisms Using Distributed Acoustic Sensing

This chapter was submitted in this form in:

Xiao, H., Tanimoto, T., Spica, Z., Gaite, B., Ruiz-Barajas, S., Pan, M., Viens. L., Locating the precise sources of high-frequency microseisms using distributed acoustic sensing Submitted to *Geophysical Research Letters*, in revision

4.1 Introduction

There is a long history of studying ambient seismic noise, especially the predominant ocean-generated microseisms (Hasselmann, 1963; Longuet-Higgins, 1950; Wiechert, 1904). It is now well established that there are two main frequency bands that are referred to as the primary (0.05-0.07 Hz) and secondary microseisms (0.13-0.40 Hz) (Hasselmann, 1963; Le Pape et al., 2021; Longuet-Higgins, 1950; Retailleau & Gualtieri, 2021; Stutzmann et al., 2000; Tanimoto, 2007; Toksöz & Lacoss, 1968; Xiao et al., 2021). But this is a crude classification as new seismic data have shown more details in the structure of seismic noise. For example, there is evidence that the secondary microseisms consist of two separate peaks within their frequency band (Koper & Burlacu, 2015). Other evidence shows the arrivals of teleseismic signals at about 0.2 Hz that are generated by far-away storms mix with locally generated secondary microseisms (Kedar et al., 2008; Nishida & Takagi, 2016). Microseisms can excite both surface and body waves (Koper et al., 2010; Nishida & Takagi, 2016; Retailleau & Gualtieri, 2021; Xiao et al., 2021), which are extensively used to explore and monitor the Earth's interior at all scales through cross-correlations (F. Brenguier et al., 2008; Florent Brenguier et al., 2008; Denolle et al., 2014; Poli et al., 2012; Shapiro et al., 2005). Thus far, the lack of high-density offshore seismic observations prevented seismologists from fully characterizing the complexity of microseisms. We can now move beyond this limitation using distributed acoustic sensing (DAS) and existing underwater telecommunication infrastructures (Lindsey et al., 2019; Sladen et al., 2019; Spica et al., 2020; Williams et al., 2019).

DAS is a new method to measure the Earth's vibrations at an unprecedented resolution. It uses the optical phase changes of Rayleigh backscattered light to turn fibre-optic cables into

dense arrays of seismic sensors measuring dynamic longitudinal strain or strain rate. At the end of the fibre, an interrogator unit (IU) sends laser pulses down the cable. The propagation of the laser pulses is affected by heterogeneities in the fibre and some of the energy travels back to the IU. When the fibre is disturbed by external forcing, changes in the phase of the backscattered light are measured by the IU and can be turned into continuous strain measurements along the fibre with a very high spatial resolution (Muanenda, 2018; Posey et al., 2000). For an extensive review of the DAS technology, we refer the reader to Hartog (2017).

In this study, DAS data were recorded along a sea-bottom cable linking Valencia to Palma de Mallorca, Spain (Figure 4.1). By using short-term cross-correlation methods, we achieved for the first time precise localisation of the sources of microseisms. We report our observations on the variations of microseism source locations for frequencies about 0.5-2.0 Hz. To distinguish this high-frequency signal from the well-known microseisms, we use the term "the High-Frequency microseisms (HF microseisms)" in this study. We found that the excitation source locations of HF microseisms are confined to a zone of about 7-27 km from the coast. Furthermore, the spatial extent of the source at a given time is much smaller, only a few kilometres in extent and this source region moves with the wind constantly. It suggests that the wind-generated ocean waves near the coast are exciting HF microseisms through the wave-wave interactions (Hasselmann, 1963; Longuet-Higgins, 1950). A theoretical analysis by the normal-mode theory supports this scenario.

4.2 Results

We used a pre-installed telecommunication fibre-optic cable operated by IslaLink that connects the Spanish peninsula to Mallorca Island from Valencia to Palma de Mallorca (Figure 4.1). From September 1st to September 15th, 2020, a FEBUS Optics A1-R interrogator was connected to the Valencia side of the cable to probe the first 50 kilometres of the cable. The initial 8,555 meters are located on land, and the following 41,445 meters are under the seabed. According to the installation report provided by the cable operator, the cable is buried ~1 m below the seabed for the full length of the measurement. The data were acquired with a sampling frequency of 1000 Hz, a gauge length of 30.4 m, and a spatial resolution of 16.8 m, turning the first 50 km of the cable into a seismic array of 2977 channels. We only analyse the data recorded between September 1st and September 7th, which are continuous, and exclusively focus on the underwater portion of the cable.

4.2.1 Ocean surface gravity waves and Scholte waves

Each channel exhibits two energy peaks in the frequency domain (Figure 4.2a). The first peak has a frequency band of 0.05-0.2 Hz. It is mainly observed in shallow waters, and its power decreases with increasing water depth. The same signal can be observed in the frequency-wave number analysis (Figure 4.3a) and travels with a phase velocity of ~10 m/s. This corresponds to the propagation of ocean surface gravity waves in the shallow waters, where these waves can directly exert pressure on the fibre-optic cable (Lindsey et al., 2019; Sladen et al., 2019; Spica et al., 2020; Williams et al., 2019). The second peak is found in the 0.5-2 Hz frequency band. This signal travels with a phase velocity of 500-1000 m/s (Figure 4.3b) and corresponds to the propagation of the fundamental-mode Scholte waves (Figures.

5.A1-5.A3), whose energy is essentially trapped under the seabed (Lindsey et al., 2019; Nishida, 2017; Nolet & Dorman, 1996; Scholte, 1958; Sladen et al., 2019; Spica et al., 2020; Williams et al., 2019).

Figure 4.2b shows 40 seconds of the strain rate data filtered between 0.5 and 1 Hz. The propagations of the HF microseisms are revealed through oblique stripes travelling either up to the right toward the land (i.e., landward) or propagating seaward down to the right. In addition, Figure 4.2c shows that ocean waves that propagate in opposite directions mainly occur in the 0.25-0.5 Hz frequency range (period 2-4 s in Figure 4.2c), which corresponds to approximately the double-frequency relationship between the microseism signals and the ocean waves. The modal analysis (Figures 5.A1-5.A5) supports that the wave-wave interactions of ocean surface waves generate the wavefield at the seabed that dominates the HF microseisms (Longuet-Higgins, 1950).

4.2.2 The sources of HF microseisms

To better understand the wavefield created by the HF microseisms, we computed cross-correlation functions (CCFs) of DAS data for every 1.5-km (i.e., 90 channels) interval along the cable. To increase the stability of the CCF signals, we stacked five adjacent channels. Then, we performed a CCF calculation with the following five stacked channels at 1.5 km away. In the CCFs, we identify acausal (negative) and causal (positive) wave packets propagating landward and seaward, respectively. These are the same propagating waves observed in Figure 4.2b. The correlation technique allows us to track the propagation directions of the HF microseisms (Figures 5.4a and 5.4b). Due to the strong energy of this signal, we found that stable CCFs are obtained for time series as short as 10 minutes. These

10-minute CCFs match the 6-day-long stacked CCFs (Figures 5.4a and 5.4b), implying that Scholte waves are propagating parallel to the fibre. Therefore, we used the 10-minute-long time series to gain higher temporal resolution in this study. We computed the CCFs between all channel pairs spaced by 1.5 km for each 10-minute time series. Therefore, for every 10 minutes, it provides us 2374 CCF results for the entire 2468 DAS channels along the seabed.

We used the signal-to-noise ratio (SNR) to evaluate the existence and significance of HF microseisms. The SNR was computed by taking the maximum amplitudes of the signals, independently for the acausal part and the causal part, and taking their ratio to the noise amplitude, which was estimated from the average amplitude in the trailing CCF coda for a duration of 200 sec (Figure 4.A6). Figure 4.4a is an example of CCF that clearly shows the landward propagation of HF microseism (acausal part in red) with an SNR of 12.3. The wave propagation of waves toward the deeper sea (causal part in blue) is, however, unclear even though SNR becomes 3.1. Figure 4.4b is a case in which there are clear seaward signals but not a hint of landward propagation. In this case, SNR is 9.8 for seaward propagation and 3.2 for landward propagation. In general, SNR is larger than 4.0 when we see a recognisable wave packet in the CCF. Figure 4.4c shows the results for all the CCFs computed for all 10-minute intervals for the entire six days and expressed as a function of their SNR for both landward (red) and seaward propagation (blue).

Figure 4.4c illustrates that between 0 and 7 km from the coast, the causal part of the CCFs (i.e., blue lines) exhibit an overall SNR lower than 3, which means that there is no significant seaward propagation. However, the landward propagating signals are much larger. On the other hand, beyond ~27 km from the coastline, seaward propagation becomes dominant. The landward propagating signals show SNR under 4, suggesting that the wavefield beyond 27

km is dominated by HF microseisms propagating toward the deeper sea. Until now, an excitation source of HF microseisms was assumed to emit seismic waves in both the landward and seaward directions from the source (Ardhuin & Herbers, 2013; Hasselmann, 1963; Longuet-Higgins, 1950; Tanimoto, 2007). However, the patterns in Figure 4.4c suggest that the source regions of the HF microseism are mostly confined within 7-27 km from the coast and the sources can radiate seismic waves in either landward or seaward direction and/or both.

4.2.3 Spatiotemporal variations of HF microseisms sources

To see the temporal fluctuation of the sources, Figures 5.5a and 5.5b show the SNR results as a function of time. For every 10-minute interval, the SNR of seaward and landward signals are plotted from left to right for about six days with respect to distance from the coast. This figure shows that patterns in SNR change rapidly in time, meaning that the source locations are constantly moving. Sometimes, the source is all the way out to 25 km from the coast (black circle on Sept. 2). This indicates that the landward propagation dominates the wavefield. On Sept. 3 (green circle), the wavefield mostly consists of seaward propagation, which means the excitation source is about 10 km from the coast. And most of the time, the source seems to be somewhere between 15 and 20 km from the coast (pink circle). It is important to recognise that the position of the HF microseisms sources is constantly changing, and the extent of the source is relatively small for a given time instance.

By putting the variations of SNR in Figures 5.5a and 5.5b in a single plot, we can constrain the source locations for the frequency band 0.5-1 Hz (Figure 4.6a). The positions between the two-colour regions (red and blue) must be the source location because away from the source,

the SNR of landward (red) should become smaller toward the deeper sea, and the SNR of seaward (blue) should become smaller toward the coast. This range cannot be determined precisely, but in Figure 4.6b, we show a case where we treat the region of SNR larger than 5 in both landward and seaward propagations as the source region. The orange area shows the source extent, which oscillates in time and space. For each time instance, the spatial extent of the source is limited to an area of a few kilometres to 10 km. A similar analysis was applied to HF microseisms for a higher frequency band 1-2 Hz (Supplementary Figure 4.7b) and shows that the timing of changes in source location mostly agrees with those in Figure 4.6b. These results depend on the threshold selection of SNR 5, and a different choice would provide broader or narrower estimates. Nonetheless, in most cases, the extent of the source region appears to be limited to a strip of 10 kilometres, most often within a few kilometres. Such a source area is constantly changing within the 7-27 km region from the coast, which is where the bathymetry varies from 25 to 100 m in depth.

4.3 Discussion and conclusions

How can we explain such changes in the excitation source of HF microseisms? We believe that the wave-wave interaction of ocean waves, generated by local winds, can explain these behaviours. As Figure 4.2c shows, the dominant period range of opposing winds is 2-4 seconds. Through the frequency doubling process from the collision of opposing ocean waves (Ardhuin et al., 2011; Hasselmann, 1963; Longuet-Higgins, 1950; Tanimoto, 2007), they can create seismic wavefields in the range 0.5-1.0 Hz, which is found in our data. The modal analysis shows that this process preferentially excites the fundamental-mode surface waves, as shown in Supplementary Figure 4.4. This mode may be called the Scholte wave as the

maximum displacements occur at the sea bottom (Figure 4.A3) and decay upward and downward from the seabed. Its large horizontal amplitude indicates an efficient excitation of extensional strain, which is the primary signal in DAS data. The constantly changing source locations are most likely related to the ephemeral behaviours of wind and its related ocean waves (black line in Figure 4.6a). Locations of wave-wave interactions should naturally change if the wind were the source of this process.

The water depth must be an influential parameter as shown in modal analysis, and thus the efficiency of excitation of such modes can change significantly concerning depth. A relatively flat and shallow Mediterranean seabed with a depth range of 25-100 m may have played a prevailing role in our observations. Excitation of the HF microseisms should differ under different bathymetric conditions.

There is no question, however, that DAS will soon play a significant role in understanding the excitation mechanisms of microseisms worldwide.

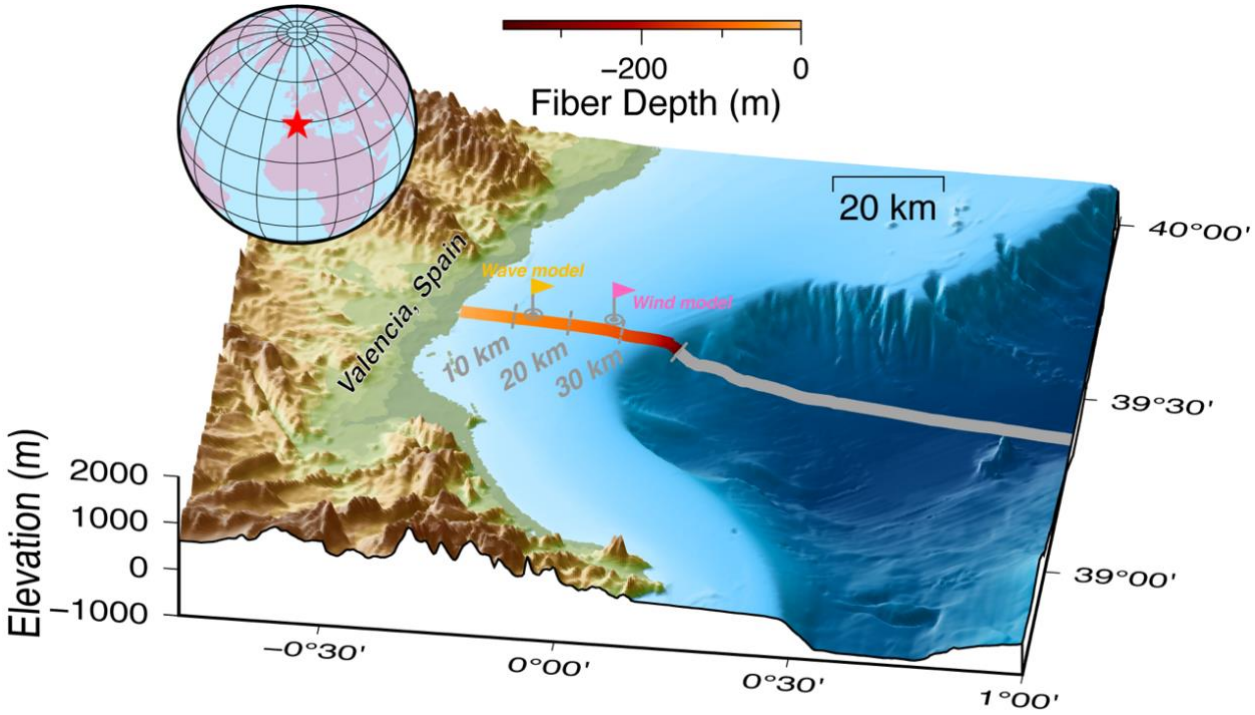

Figure 4.1. The geographic location of the fibre-optic cable in this study. The red line is the portion of the fibre-optic cable we analysed, and its colour represents its depth. The grey line is the portion that was not used. The yellow and pink flags indicate the location of simulated waves and wind, respectively.

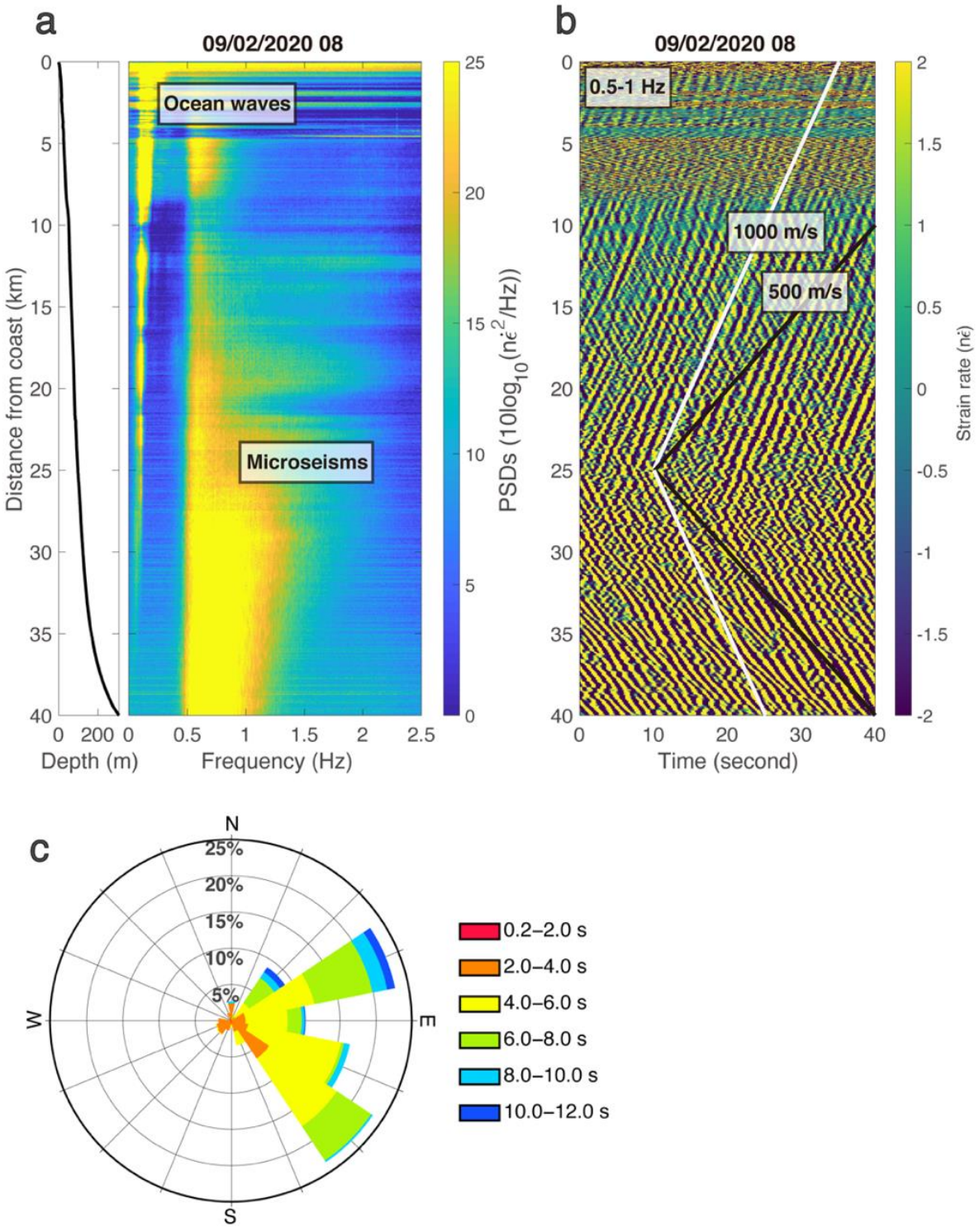

Figure 4.2. DAS data and wave rose. (a) Power spectral densities of one-hour DAS strain rate data on September 2nd, 2020. (b) Forty seconds of DAS data filtered between 0.5 and 1 Hz along the fibre-optic cable showing HF microseism propagating landward and seaward. (c)

Rose of the peak period of ocean waves during September 2020 at the location indicated by the yellow flag in Figure 4.1. Note that ocean waves propagating in the opposite directions are mainly 2-4 seconds (0.25-0.5 Hz).

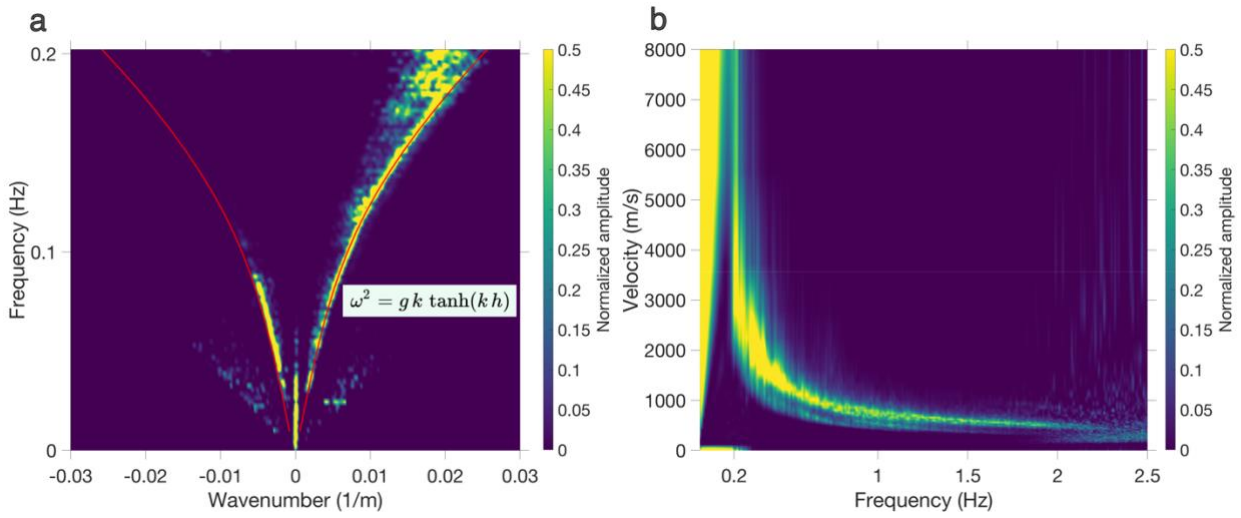

Figure 4.3. One-hour F-K beamforming analysis for DAS data on September 3rd, 2020. (a) The data are taken between 8 and 9 km from the coast, where the water depth is about 40 m. The red lines represent the theoretical dispersion curve of ocean surface gravity waves for a water depth of 40 m. (b) The phase velocity of Scholte waves was observed between 25 and 40 km from the coast versus frequency. Clear surface-wave dispersion can be seen for frequencies higher than 0.2 Hz. Note that our analysis focuses on the 0.5-2.0 Hz frequency range.

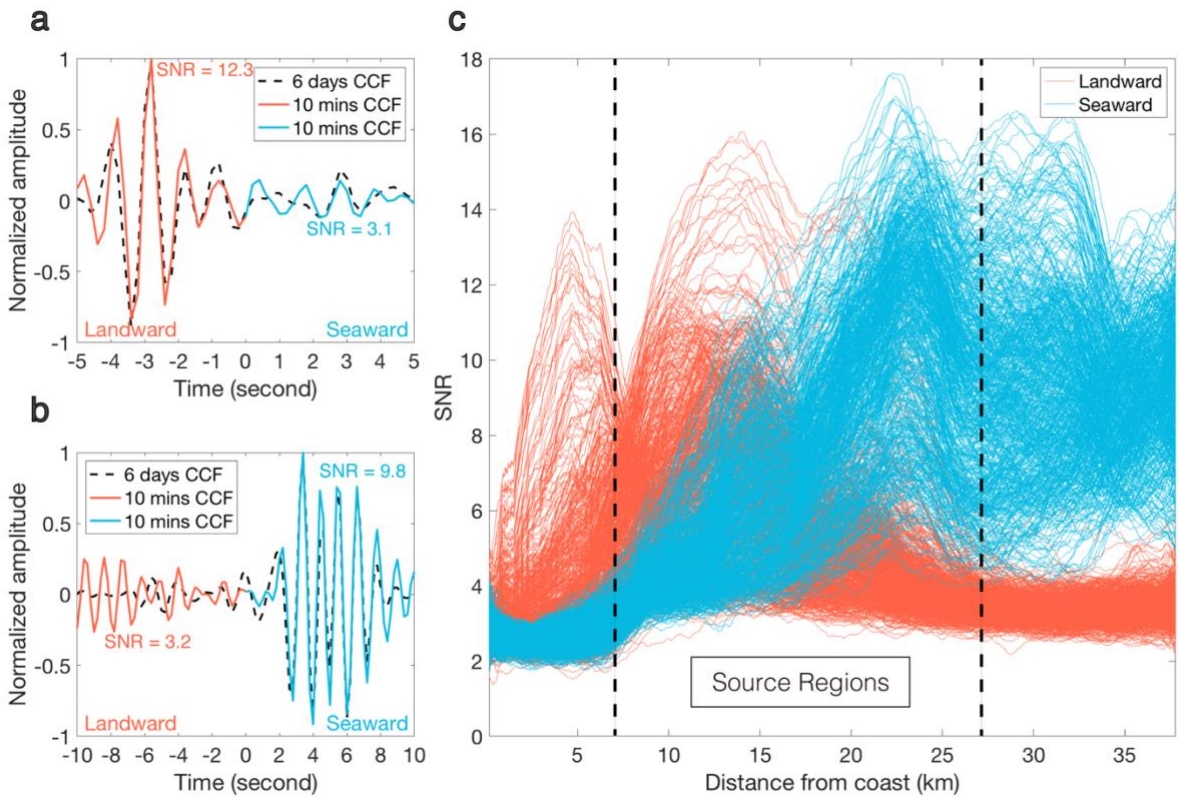

Figure 4.4. Cross-correlation function results. (a) CCF between channels 300-305 (channel 300 is at 5.0 km from the coast) and 390-395 (channel 390 is at 6.5 km from the coast) in the 0.5-1 Hz frequency band. The dashed line shows the 6-day stacked CCF result. The red and blue lines show the 10-minute CCF results. The positive correlation lags (blue line) are the seaward propagation, and the negative lags (red line) are the landward propagation of HF microseism. (b) Same as (a) but for channels 2000-2005 (channel 2000 is at 33.6 km from the coast) and channels 2090-2095 (channel 2090 is at 35.1 km from the coast). (c) SNR of HF microseisms in the frequency band 0.5-1 Hz. Each line represents the SNR variation of the Scholte wave along the fibre, obtained from the 10-minute CCFs. All the results for the 6 days are plotted on this graph. Beyond 27 km from the coast, the seaward propagation dominates, while closer to the coast at 7 km, the landward propagation prevails.

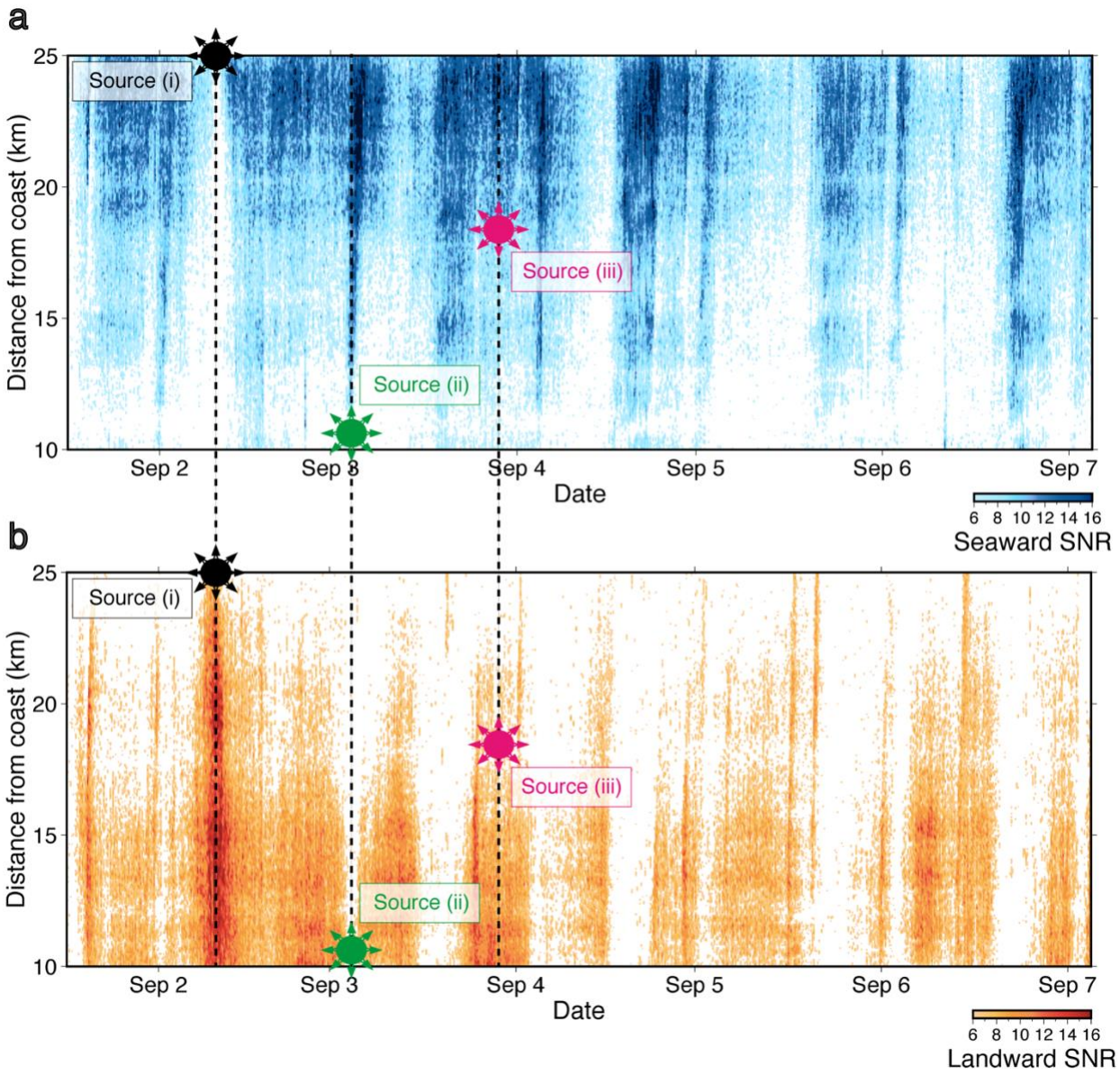

Figure 4.5. Variations in SNR of the HF microseisms. (a) seaward and (b) landward propagations from CCF with SNR higher than 6 and filtered between 0.5 and 1 Hz. The three different coloured circles show three representative source locations of the HF microseisms.

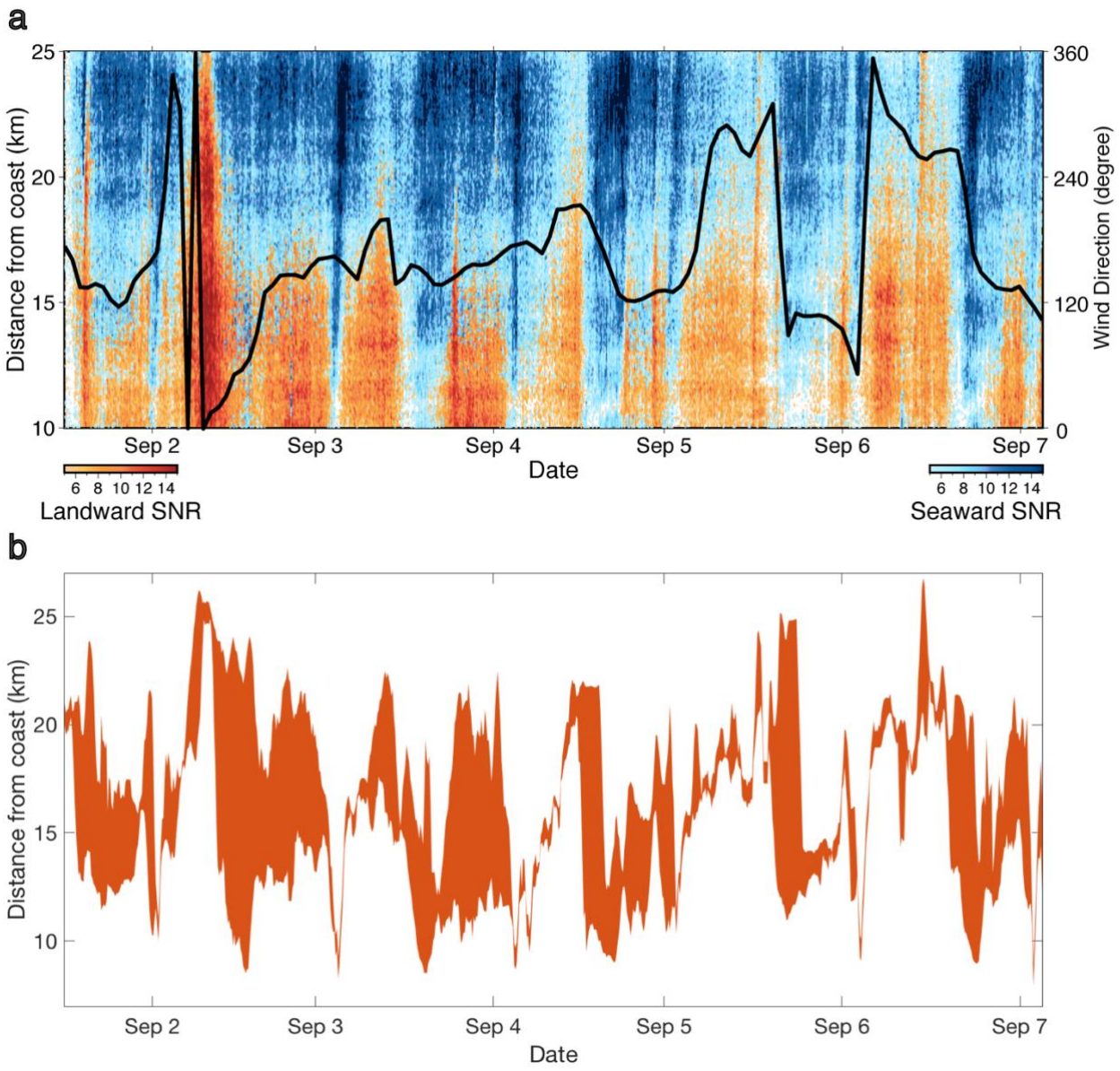

Figure 4.6. HF microseisms source locations. (a) Same data as Figures 5.5a and 5.5b but plotted the intersection between the two colors to observe better changes in HF microseism source locations in the frequency band 0.5-1 Hz. The position between the two-color series defines the source locations of HF microseisms. The black line depicts the local wind direction change, measured at the location marked in Figure 4.1. (b) The source regions of HF microseisms in the frequency band 0.5-1 Hz. We define the locations of the HF microseism source using a SNR higher than 5 for both seaward and landward propagating Scholte waves.

4.4 Appendix

4.4.1 F-K beamforming

We calculated the two-dimensional frequency-wavenumber (F-K) spectrum by applying a F-K beamforming technique to each hour of the data (Capon, 1969). The aperture of the seismic array determines the resolution of the smallest wavenumber (Schweitzer et al., 2002). Arrays with large apertures can acquire high-speed seismic waves. For ocean waves, which have relatively large wavenumbers, we used DAS data recorded over 1 kilometre (Figure 4.2a). To observe Scholte waves (Figure 4.2b), we used data recorded over 15 kilometres.

4.4.2 Wind and ocean waves data

Waves and wind data were obtained from the Spanish Ports Authority database (Puertos del Estado), called SIMAR (SImulación MARina in Spanish). SIMAR comes from WANA and is based on WAM (Group, 1988) and WaveWatch III (Tolman, 2009). The temporal sampling resolution of the wind data is 1 hour.

4.4.3 Excitation of modes by the wave-wave interaction of wind ocean waves

The far-field Green's tensor for a spherical Earth (Dahlen & Tromp, 2021) can be written as

$$G(\mathbf{x},\mathbf{x}'\,;\,\omega) = \sum \frac{1}{cCI\sqrt{8\pi k_l|sin\Delta|}}\left[\hat{r}U - i\hat{k}V + i(\hat{r}\times\hat{k})W\right]\left[\widehat{r'}\,U' + i\widehat{k'}\,V' - i\left(\widehat{r'}\times\widehat{k'}\right)W'\right]$$

$$\times \exp\left\{-i\left(k_l\Delta + \frac{\pi}{4}\right) - \frac{\omega\Delta}{2CQ}\right\} \tag{5.1}$$

where **x**, **x**′, and ω are the station location, the source location, and the angular frequency ($\omega = 2\pi f$ where f is the frequency), respectively. The summation is conducted for modes in each modal branch (e.g., the fundamental mode branch, the 1st overtone branch, etc.). c is the phase velocity of a given mode, C is the group velocity, I is the normalization for a spheroidal mode defined by $k_l = \sqrt{l(l+1)}$, Δ is the angular distance from the source to the station, Q is the attenuation parameter for a given mode. Note that this equation is for the spherical Earth.

We consider a modal excitation problem by the wave-wave interaction of ocean surface waves in a flat-layered model. The horizontal displacement in the cylindrical coordinate can be defined as:

$$u_r(\omega) = \sum \frac{1}{cCI\sqrt{8\pi kr}}\{-iV(0)U'(H)\} \times \exp\left\{-i\left(kr + \frac{\pi}{4}\right) - \frac{\omega r}{2CQ}\right\} \tag{5.2}$$

in the radial direction (r). The normalization factor I is defined as:

$$I = \int \rho(U^2 + V^2)dz \tag{5.3}$$

where $U(z)$ and $V(z)$ are the vertical and horizontal eigenfunction of a spheroidal mode (Rayleigh-wave mode) and z is the vertical coordinate (positive upward) where the sea bottom is $z = 0$ and the ocean surface is $z = H$.

The wave-wave interaction of ocean waves near the ocean surface generates pressure (Longuet-Higgins, 1950) and with an introduction of a surface area dS, it creates a vertical force $f = -pdS$. This force can be multiplied to the above formula to obtain the generation of horizontal displacements at sea floor.

Since DAS measures strain along the fibre-optic cable, we differentiate the above formula with respect to $\boldsymbol{r}$ and derive the following formula for the extensional strain in the radial direction:

$$e_{rr}(\omega) = \sum \frac{1}{cCI}\sqrt{\frac{k}{8\pi r}}\{-V(0)U'(H)\} \times \exp\left\{-i\left(k\mathrm{r} + \frac{\pi}{4}\right) - \frac{\omega \mathrm{r}}{2CQ}\right\} \qquad (5.4)$$

where we only kept the term that differentiates the exponential oscillation term. Differentiation with respect to $1/\sqrt{r}$ should rapidly become small with distance and the differentiation of the attenuation term should also be small. In this formula, k is the horizontal wavenumber. We can rewrite this formula as

$$e_{rr}(\omega) = \sum a_s \exp\left\{-i\left(k\mathrm{r} + \frac{\pi}{4}\right) - \frac{\omega \mathrm{r}}{2CQ}\right\} \qquad (5.5)$$

where a_s is the excitation coefficient for a mode defined by:

$$a_s = \frac{1}{cCI}\sqrt{\frac{k}{8\pi r}}\{-V(0)U'(H)\} \qquad (5.6)$$

The efficiency of excitation of various mode branches is related to the size of this term and is computed for various models.

4.4.4 Modal analysis

We vary the ocean depth from 25 m to 500 m and examine the effects on modal excitations. Below the sea bottom, all models have a sedimentary layer of a thickness of 1 km (density (ρ): 2000 kg/m^3, Vp: 2.0 km/s, Vs: 1.0 km/s), a transition layer with a thickness of 1 km where ρ and seismic velocities increase linearly with depth and finally connect to the parameters from the PREM model (1981). The PREM parameters are assumed from 2 km

below the sea bottom. PREM has the upper crustal parameters of ρ: 2600 (kg/m^3), Vp: 2.6 (km/s), Vs: 3.2 (km/s), and the parameters after transition to lower crust are ρ: 2900 (kg/m^3), Vp: 6.8 (km/s), Vs: 3.9 (km/s).

In Figure 4.A1, we show an example of the modal analysis performed with a model that has an ocean depth of 100 m. We use a code for spherical modes that incorporates gravity effects. Therefore, for each wavenumber (horizontal wavelength), we first obtain a tsunami mode with a phase velocity of $\sqrt{gH}$. Figure 4.A1 shows overtone modes up to the 4th one. The fundamental mode is termed as the Scholte mode for the reasons listed below.

Figure 4.A2 shows the same set of modes. Tsunami modes are confined to the low-frequency range (e.g., below 0.2 Hz) and do not appear in the 0.5-2.0 Hz frequency range, which is the focus of this work. The phase velocity of Scholte waves for frequencies above 0.5 Hz (e.g., 0.8-1.0 km/s) shows good agreement with Figure 4.3b. It supports that we mainly observe the effects of Scholte waves. Eigenfunctions of four modes at 1 Hz, indicated by solid circles in Figure 4.A2, are shown in Figure 4.A3.

We name the fundamental mode as the Scholte mode in this paper because eigenfunctions have their maximum amplitudes at the seabed (Figure 4.A3). The amplitudes tend to decay up and down from the seafloor, although strictly speaking, they deviate from what were originally known as Scholte waves, which were trapped at the fluid-solid interface on the seafloor.
The excitation coefficients of these modes are shown in Figure 4.A4. This figure shows clearly that the wave-wave interactions at the ocean surface preferentially excite Scholte modes. The effect of the ocean depth on the excitation coefficients is shown in Figure 4.A5. This figure shows that the results in Figure 4.A4 remain very similar from 25 m to 100 m in depth, which are relevant to this study. It also shows that ocean depths deeper than 200 m show much less

excitation of Scholte modes. This suggests that the excitation efficiency may greatly differ if the ocean depth steeply increases near the coast.

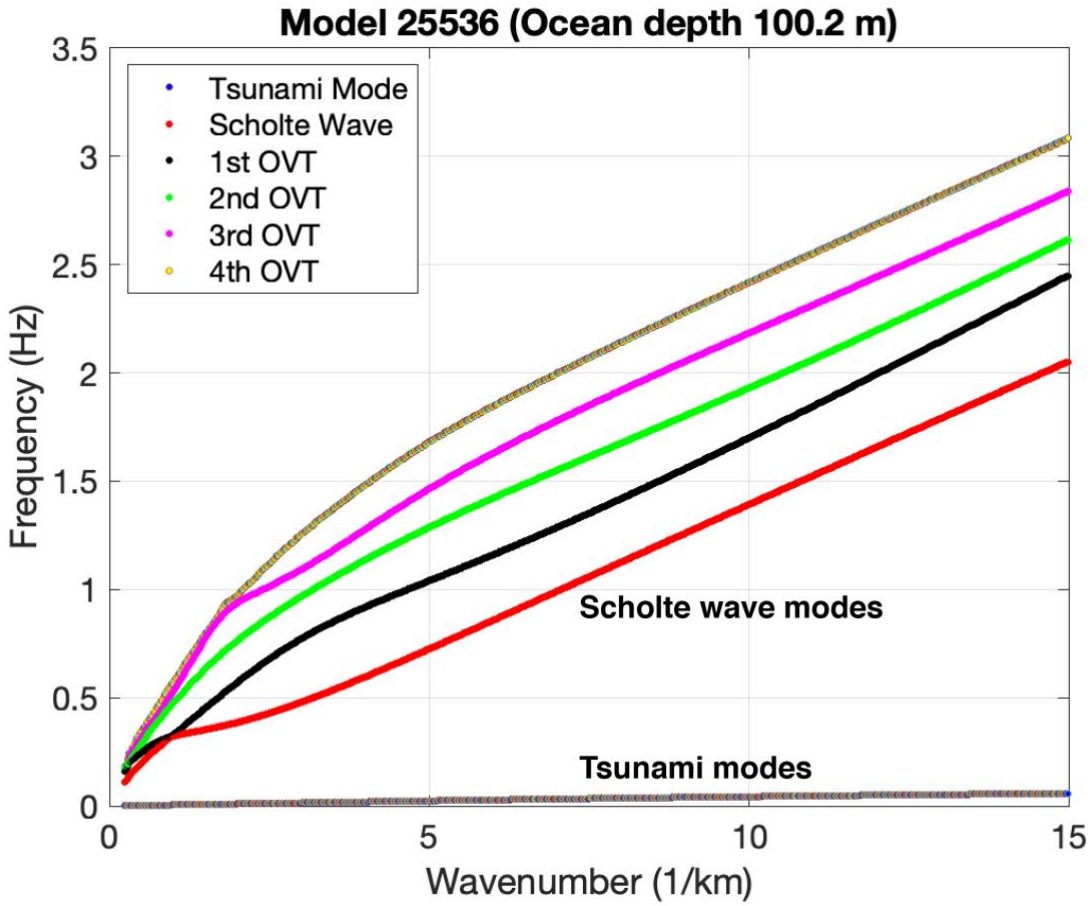

Figure 4.A1. Eigenfrequencies plotted against wavenumber. For each horizontal wavenumber, the lowest mode is the tsunami mode (equivalent mode). The fundamental mode is named as Scholte wave or Scholte mode because of a large horizontal motion peak at the sea bottom. The first four modes (overtones: OVT) are shown in this plot.

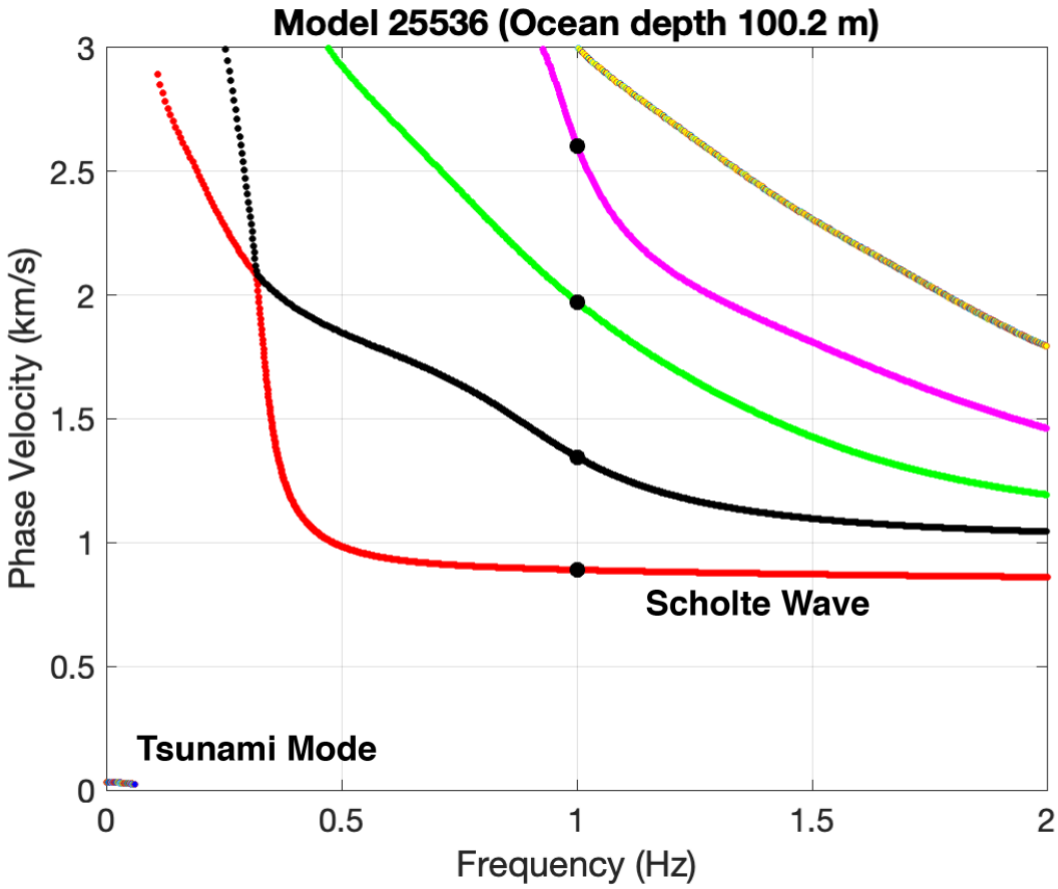

Figure 4.A2. Phase velocity of the normal modes plotted against frequency. Color code is the same as in Figure 4.A1.

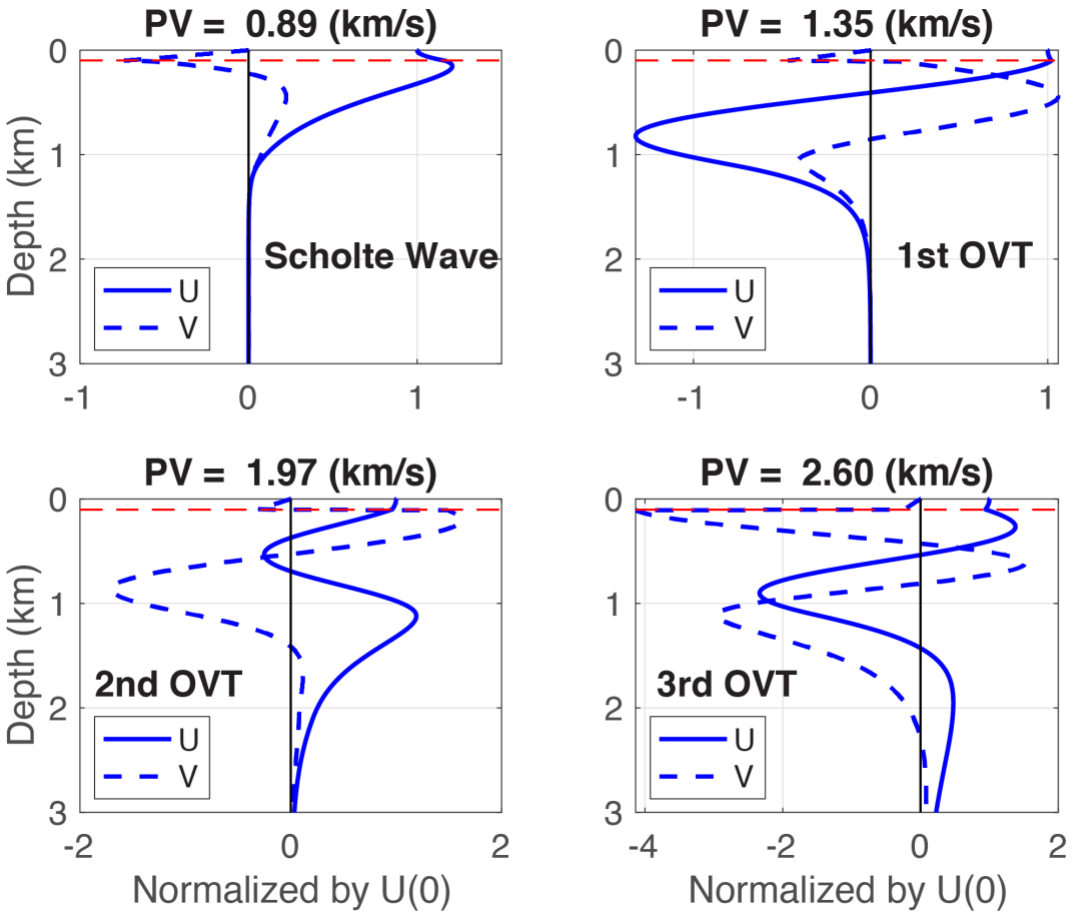

Figure 4.A3. Eigenfunctions of four modes at 1 Hz, indicated by solid circles in Figure 4.A2. The eigenfunctions of the Scholte waves (upper left) are very similar to that of Rayleigh waves on land, except for the behaviors in the ocean. The red dashed line is sea bottom.

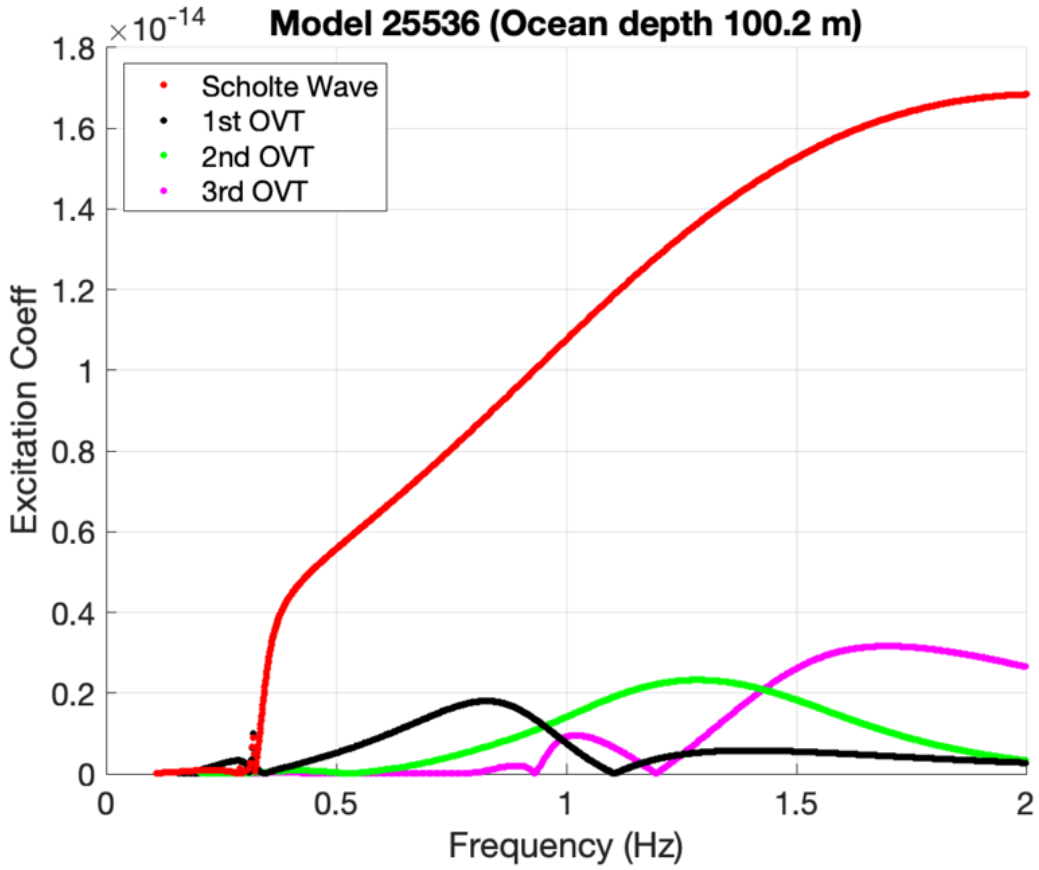

Figure 4.A4. Excitation coefficients $|a_s|$ of Scholte modes. The fundamental mode (the red dots), 1st (the black dots), 2nd (the green dots), and 3rd (the purple dots) overtones (OVT) of Scholte waves are shown. For horizontal strain at the ocean bottom, the contributions from Scholte waves are dominant.

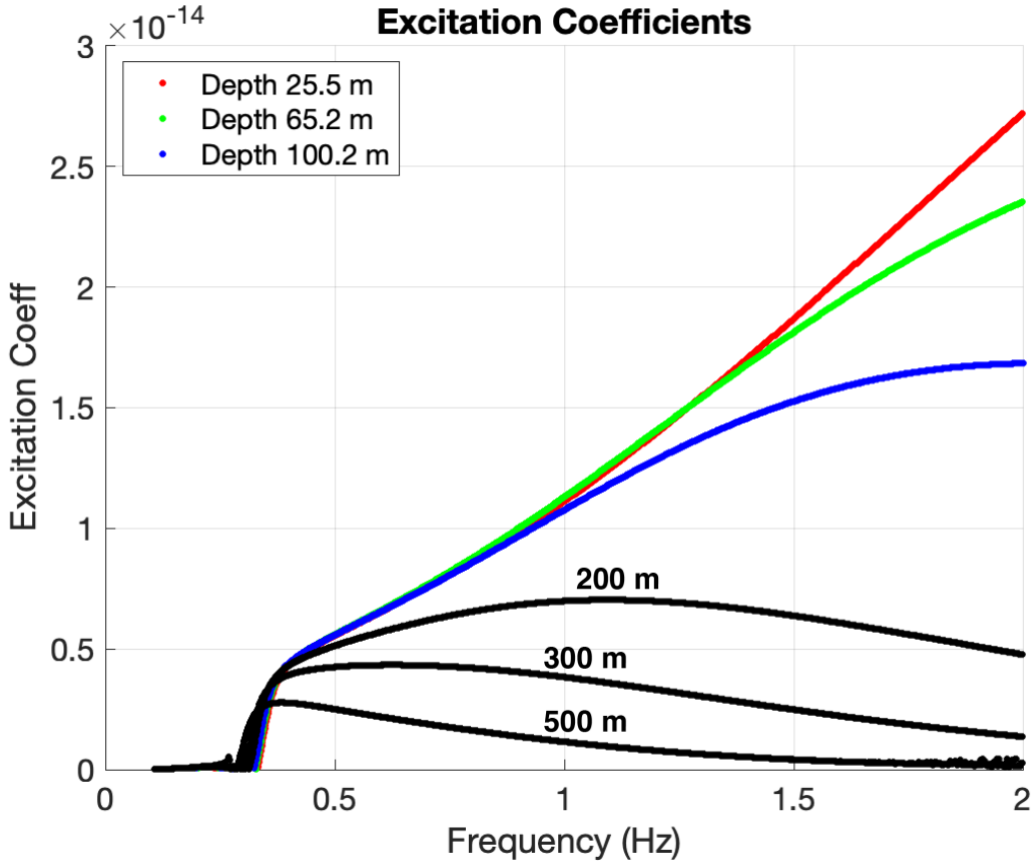

Figure 4.A5. Excitation coefficients at different depths. We observe the excitation sources changing in the area where ocean depth varies from 25 m to 100 m. Three cases within this depth range are shown in color and agree between 0.5 Hz and 1.0 Hz. Three cases for the deeper ocean, 200 m, 300 m, and 500 m, show that the excitation efficiency by the wave-wave interaction of ocean surface waves decreases quickly with depth.

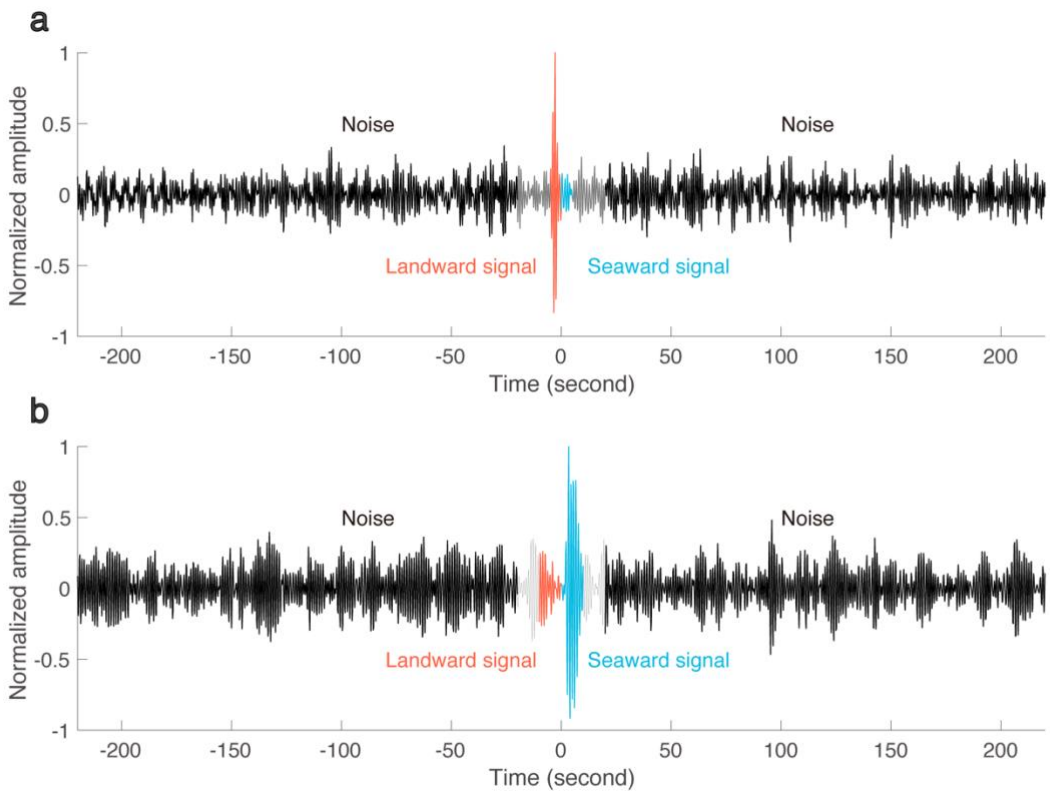

Figure 4.A6. Examples of Cross-Correlation Functions. (a) CCF between channels 300-305 (channel 300 is at 5.0 km from the coast) and channels 390-395 (channel 390 is at 6.5 km from the coast) in the frequency band 0.5-1 Hz. The red and blue lines show the Scholte wave selected in this study. The causal (blue) and acausal (red) parts relates to the seaward and landward propagations of Scholte waves. The black line shows the trailing coda for a duration of 200 sec. We calculated the signal-to-noise ratio (SNR) by using the maximum amplitude of the signals (red and blue) divided by the mean value of 200 seconds of trailing coda (black). (b) Same as a for channels 2000-2005 (channel 2000 is at 33.6 km from the coast) and channels 2090-2095 (channel 2090 is at 35.1 km from the coast).

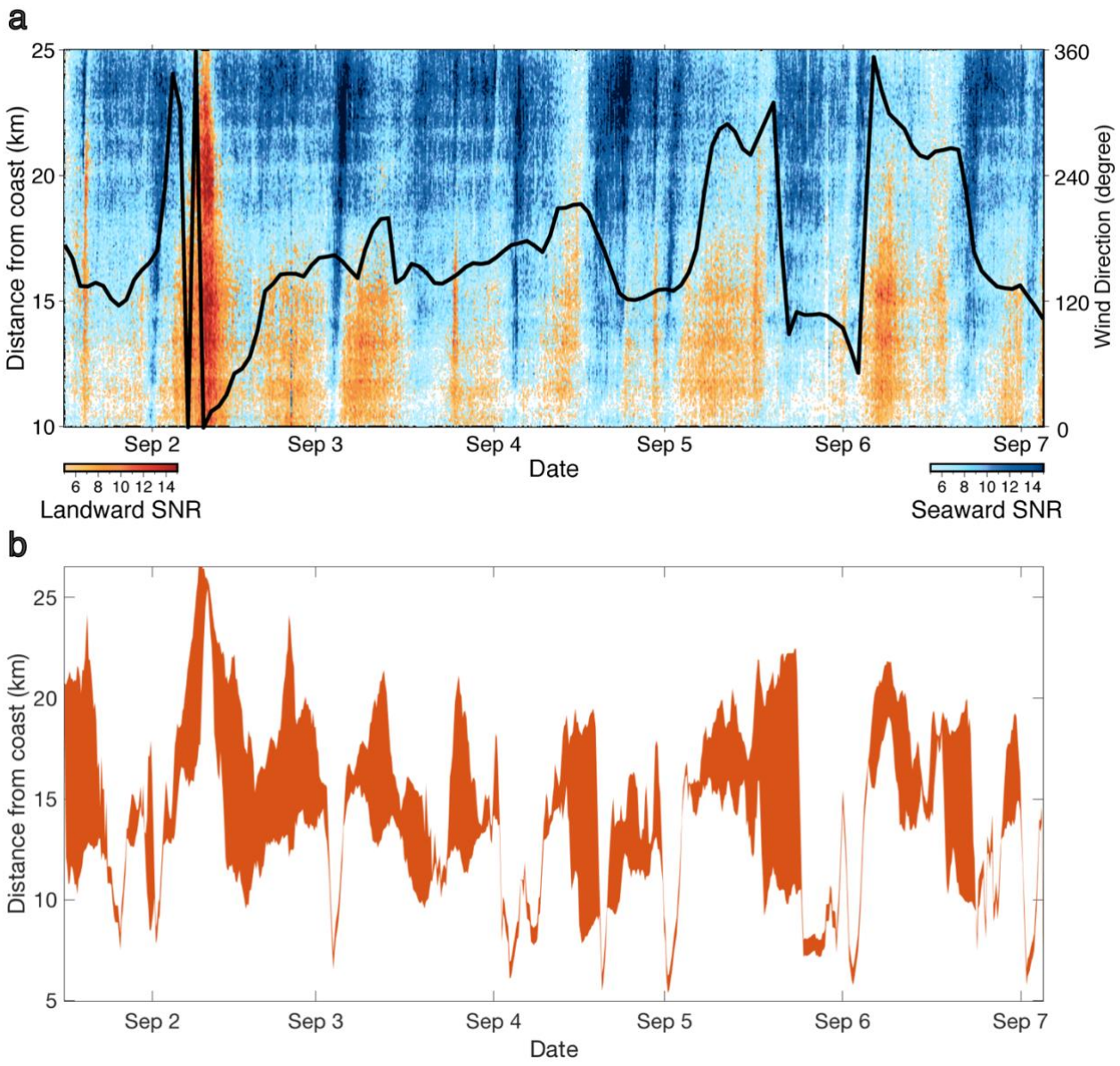

Figure 4.A7. HF microseisms source locations in the frequency band 1-2 Hz. (a) The SNR of the Scholte waves in the frequency band 1-2 Hz as a function of time for the seaward (blue) and landward direction (red) propagation. The position between the two-color series represents the source location of the HF microseism. The black line represents the local wind direction change recorded at the location marked in Figure 4.1. (b) The source regions of HF microseisms in the frequency band 1-2 Hz. We define the source locations of the HF

microseisms as the SNR of both seaward and landward propagating Scholte waves larger than 5.

4.5 References

Ardhuin, F., & Herbers, T. H. C. (2013). Noise generation in the solid Earth, oceans and atmosphere, from nonlinear interacting surface gravity waves in finite depth. *Journal of Fluid Mechanics, 716*, 316-348. https://doi.org/10.1017/jfm.2012.548

Ardhuin, F., Stutzmann, E., Schimmel, M., & Mangeney, A. (2011). Ocean wave sources of seismic noise. *Journal of Geophysical Research, 116*(C09004). https://doi.org/10.1029/2011JC006952

Brenguier, F., Campillo, M., Hadziioannou, C., Shapiro, N. M., Nadeau, R. M., & Larose, E. (2008). Postseismic Relaxation Along the San Andreas Fault at Parkfield from Continuous Seismological Observations. *Science, 321*(5895), 1478-1481. https://www.science.org/doi/abs/10.1126/science.1160943

Brenguier, F., Shapiro, N. M., Campillo, M., Ferrazzini, V., Duputel, Z., Coutant, O., & Nercessian, A. (2008). Towards forecasting volcanic eruptions using seismic noise. *Nature Geoscience, 1*(2), 126-130. https://doi.org/10.1038/ngeo104

Capon, J. (1969). High-resolution frequency-wavenumber spectrum analysis. *Proceedings of the IEEE, 57*(8), 1408-1418.

Dahlen, F. A., & Tromp, J. (2021). Princeton University Press. https://doi.org/10.1515/9780691216157

Denolle, M. A., Dunham, E. M., Prieto, G. A., & Beroza, G. C. (2014). Strong Ground Motion Prediction Using Virtual Earthquakes. *Science, 343*(6169), 399-403. https://www.science.org/doi/abs/10.1126/science.1245678

Group, T. W. (1988). The WAM Model—A Third Generation Ocean Wave Prediction Model. *Journal of Physical Oceanography, 18*(12), 1775-1810.

https://journals.ametsoc.org/view/journals/phoc/18/12/1520-0485_1988_018_1775_twmtgo_2_0_co_2.xml

Hartog, A. H. (2017). *An introduction to distributed optical fibre sensors*, CRC press.

Hasselmann, K. (1963). A statistical analysis of the generation of microseisms. *Reviews of Geophysics*, *1*(2), 177-210. https://doi.org/10.1029/RG001i002p00177

Kedar, S., Longuet-Higgins, M., Webb, F., Graham, N., Clayton, R., & Jones, C. (2008). The origin of deep ocean microseisms in the North Atlantic Ocean. *Proceedings of the Royal Society A: Mathematical, Physical and Engineering Sciences*, *464*(2091), 777-793. https://doi.org/10.1098/rspa.2007.0277

Koper, K. D., & Burlacu, R. (2015). The fine structure of double‐frequency microseisms recorded by seismometers in North America. *Journal of Geophysical Research: Solid Earth*, *120*(3), 1677-1691. https://doi.org/10.1002/2014JB011820

Koper, K. D., Seats, K., & Benz, H. (2010). On the composition of Earth's short-period seismic noise field. *Bulletin of the Seismological Society of America*, *100*(2), 606-617. https://doi.org/10.1785/0120090120

Le Pape, F., Craig, D., & Bean, C. J. (2021). How deep ocean-land coupling controls the generation of secondary microseism Love waves. *Nature Communications*, *12*(1), 2332. https://doi.org/10.1038/s41467-021-22591-5

Lindsey, N. J., Dawe, T. C., & Ajo-Franklin, J. B. (2019). Illuminating seafloor faults and ocean dynamics with dark fiber distributed acoustic sensing. *Science*, *366*(6469), 1103-1107. https://doi.org/10.1126/science.aay5881

Longuet-Higgins, M. S. (1950). A Theory of the Origin of Microseisms. *Philosophical Transactions of the Royal Society of London A-Mathematical and Physical Sciences, 243*(857), 1-35. https://doi.org/10.1098/rsta.1950.0012

Muanenda, Y. (2018). Recent Advances in Distributed Acoustic Sensing Based on Phase-Sensitive Optical Time Domain Reflectometry. *Journal of Sensors, 2018*, 3897873. https://doi.org/10.1155/2018/3897873

Nishida, K. (2017). Ambient seismic wave field. *Proceedings of the Japan Academy, Series B, 93*(7), 423-448.

Nishida, K., & Takagi, R. (2016). Teleseismic S wave microseisms. *Science, 353*(6302), 919-921. https://doi.org/10.1126/science.aaf7573

Nolet, G., & Dorman, L. M. (1996). Waveform analysis of Scholte modes in ocean sediment layers. *Geophysical Journal International, 125*(2), 385-396. https://doi.org/10.1111/j.1365-246X.1996.tb00006.x

Poli, P., Campillo, M., & Pedersen, H. (2012). Body-Wave Imaging of Earth's Mantle Discontinuities from Ambient Seismic Noise. *Science, 338*(6110), 1063. http://science.sciencemag.org/content/338/6110/1063.abstract

Posey, R., Johnson, G. A., & Vohra, S. T. (2000). Strain sensing based on coherent Rayleigh scattering in an optical fibre. *Electronics Letters, 36*(20), 1688-1689. Retrieved from https://doi.org/10.1049/el:20001200

Retailleau, L., & Gualtieri, L. (2021). Multi-phase seismic source imprint of tropical cyclones. *Nature Communications, 12*(1), 2064. https://doi.org/10.1038/s41467-021-22231-y

Scholte, J. G. J. (1958). *Rayleigh Waves in Isotropic and Anisotropic Elastic Media*, Staatsdr.- en Uitgeverijledrijf. https://books.google.com/books?id=ETNHGQAACAAJ

Schweitzer, J., Fyen, J., Mykkeltveit, S., Kværna, T., & Bormann, P. (2002). Seismic arrays. *IASPEI new manual of seismological observatory practice*, 1-51.

Shapiro, N. M., Campillo, M., Stehly, L., & Ritzwoller, M. H. (2005). High-resolution surface-wave tomography from ambient seismic noise. *Science, 307*(5715), 1615-1618. http://doi.org/10.1126/science.1108339

Sladen, A., Rivet, D., Ampuero, J. P., De Barros, L., Hello, Y., Calbris, G., & Lamare, P. (2019). Distributed sensing of earthquakes and ocean-solid Earth interactions on seafloor telecom cables. *Nature Communications, 10*(1), 5777. https://doi.org/10.1038/s41467-019-13793-z

Spica, Z. J., Nishida, K., Akuhara, T., Pétrélis, F., Shinohara, M., & Yamada, T. (2020). Marine Sediment Characterized by Ocean-Bottom Fiber-Optic Seismology. *Geophysical research letters, 47*(16), e2020GL088360. https://doi.org/10.1029/2020GL088360

Stutzmann, E., Roult, G., & Astiz, L. (2000). GEOSCOPE station noise levels. *Bulletin of the Seismological Society of America, 90*(3), 690-701. https://doi.org/10.1785/0119990025

Tanimoto, T. (2007). Excitation of microseisms. *Geophysical Research Letters*, *34*(5). https://doi.org/10.1029/2006GL029046

Toksöz, M. N., & Lacoss, R. T. (1968). Microseisms: Mode Structure and Sources. *Science, 159*(3817), 872-873. https://science.sciencemag.org/content/sci/159/3817/872.full.pdf

Tolman, H. L. (2009). User manual and system documentation of WAVEWATCH III TM version 3.14. *J Technical note, MMAB Contribution, 276*, 220.

Wessel, P., Luis, J. F., Uieda, L., Scharroo, R., Wobbe, F., Smith, W. H. F., & Tian, D. (2019). The Generic Mapping Tools Version 6. *Geochemistry, Geophysics, Geosystems, 20*(11), 5556-5564. https://agupubs.onlinelibrary.wiley.com/doi/abs/10.1029/2019GC008515

Wiechert, E. (1904). Discussion, Verhandlung der zweiten internationalen seismologischen Konferenz. *Beitrage zur Geophysik, 2*, 41-43.

Williams, E. F., Fernández-Ruiz, M. R., Magalhaes, R., Vanthillo, R., Zhan, Z., González-Herráez, M., & Martins, H. F. (2019). Distributed sensing of microseisms and teleseisms with submarine dark fibers. *Nature Communications, 10*(1), 5778. https://doi.org/10.1038/s41467-019-13262-7

Xiao, H., Tanimoto, T., & Xue, M. (2021). Study of S-Wave Microseisms Generated by Storms in the Southeast Australia and North Atlantic. *Geophysical Research Letters, 48*(15), e2021GL093728. https://agupubs.onlinelibrary.wiley.com/doi/abs/10.1029/2021GL093728

5. Future Directions

In Chapters 2 through 4, we studied the effects of the COVID-19 lockdowns on seismic noise, the existence of SH body waves in seismic noise and its potential relation to thick seafloor sedimentary layers and the near-coastal excitation sources of seismic noise. There are still many remaining questions with those projects and in the future, we envision on working on the following projects that will extend those projects.

5.1 Quantifying the relationship between human activity and seismic noise

At present, almost all research about anthropogenic noise is qualitative rather than quantitative. In Chapter 2, we verified that different noise sources have different frequencies and the seismic noise level above 1 Hz is correlated with the economic development. We also demonstrated seismic noise can provide real-time, anonymous estimates of human activity. But those analyses were qualitative and the questions remain whether we can quantitatively describe relations between the seismic noise level and the changes in local population activities. If we have truly dense seismic sensors, can we ever get to a stage to monitoring each person's activity or the movement of people within an urban area by just examining seismic noise? This may be hard to achieve but through the machine learning techniques, we envision a future in which we can establish this relationship with massive seismic data quantitatively and understand people's behaviors. Also we can make full use of DAS data for this kind of monitoring, because in cities there are already a lot of fiber optic cables buried in the ground. But this may turn out to be a scary development as it can be used to monitor each person's activity. The question may then be how to ensure anonymity of an individual.

5.2 Simulating the generation of SH-wave microseisms

In Chapter 3, we showed that the SH-wave microseisms were mainly generated near the thick sedimentary layers. However, it is still unclear how SH waves were converted from P-SV type waves that were excited by the wave-wave interactions. The best course of action seems to be to simulate the propagation process of microseisms in Earth structure that contains thick sedimentary layers. This is similar to Gualtieri et al. (2021)'s work but the direct demonstration of SH wave generation require simulation of seismic wavefields by numerical approaches. It also may be feasible to simulate how much SV waves can be converted into SH waves in the sedimentary layer. We believe we can quantitatively understand the importance of thick sedimentary layers near the source.

5.3 Mapping the global distribution of microseisms

In Chapter 4, we showed that our approach for DAS data could precisely locate the noise sources of high-frequency microseisms. This was based on the DAS study at the Spanish coast (Valencia) only. In the future we can extend this approach to map the global distributions of near-coastal noise sources.

Furthermore, we observe that these sources move quickly along narrow areas with wind directions. However, the reason why the noise sources vary with wind directions is still not fully understood. In the future, with more wind and ocean data and simulation work, we expect that this problem can be solved.

Finally, we wondered whether the continental slope of the seafloor is important for the excitation of low-frequency signals. Is it the coupling of the ocean waves or the water depth

that controls the dominant frequency of the microseisms? Answering this question is feasible because the location and amplitude of the noise source are now known but it may require more research on DAS data from different coastal regions.

5.4 References

Gualtieri, L., Bachmann, E., Simons, F. J., & Tromp, J. (2021). Generation of secondary microseism Love waves: effects of bathymetry, 3-D structure and source seasonality. *Geophysical Journal International, 226*(1), 192-219. https://doi.org/10.1093/gji/ggab095